Ludwig-Maximilians-Universität München

Sektion Physik

Influence of 5-Jet Events
on the Measurement of the
Mass of the W Boson
in e^+e^- Collisions

Diplomarbeit

von

Tim Christiansen

September 2000

*For my mom and Martin
to whom I would have loved
to explain what this
is all about . . .*

Abstract

A measurement of the mass of the W boson in hadronic $e^+e^- \rightarrow W^+W^-$ decays was performed with $183\ \text{pb}^{-1}$ of data recorded with the OPAL detector at a centre-of-mass energy of $\sqrt{s} = 189$ GeV. Using a one-dimensional reweighting technique where the W width is fixed to its Standard Model prediction, the mass was determined to

$$M_W^{4q} = 80.360 \pm 0.105^{\text{stat.}} \pm 0.093^{\text{syst.}}\ \text{GeV}.$$

Furthermore, the influence of a reconstruction of $W^+W^- \rightarrow q\bar{q}q\bar{q}(g)$ events as five jets on both the statistical and the systematic uncertainty was studied and optimised. It was also shown the feasibility of a two-dimensional analysis, a simultaneous fit to the two W masses of each event.

Contents

List of Figures

List of Tables

Chapter 1

Introduction

Understanding of the fundamental constituents of the universe has always been of great interest throughout mankind. The idea, that the microcosm, the world at infinitely small distances, is greatly related to the origin of the universe and that it contains already all the laws that govern the behaviour of nature up to the regime of our everyday life and beyond, has motivated the study of this extraordinary domain.

Since the 20th century, physicists have developed the tools to take a closer look at the behaviour of nature at the scale of elementary particles. In the study of high energetic collisions of particles, aided by the use of accelerators, one can then learn about the fundamental components of matter and their interactions under conditions that are similar to the energy density of the universe in its infancy.

The *Standard Model* of particle physics describes the elementary particles and their interactions. However, there are several free parameters that remain unpredicted and have to be determined by experiment. Also, not all ingredients of this model have been directly observed yet, so that measuring the properties of the elementary particles and their interactions not only completes the missing parts of this theory but also serves as a test of its validity and gives constraints to those parameters that have not been measured yet.

In 1934, Enrico Fermi introduced the weak force as a point-like interaction in order to explain β decays of unstable nuclei. It was already known that it could only be valid at low energies, and in the late sixties it was shown to be an effective approximation of the weak sector of the electroweak theory at low momentum transfer. This first model of the weak force described low-momentum processes very well because of the high masses of the exchange particles, the $W^{\pm}$ and Z^0 bosons, for which the interaction appears to be point-like, since at low energy these particles can only be virtually produced.

In the early eighties, the two experiments UA1 and UA2 at CERN observed the first $W^{\pm}$ and Z^0 bosons, the mediators of the weak force as predicted by the Standard Model. These particles, together with the photon, complete the framework of the electroweak theory.

Because of the hight masses of the weak bosons, very high energy is needed in particle collisions in order to create them as real particles. High precision measurements of Z^0 decays at the LEP experiments in the early nineties also serve as an indirect measurement of the W mass assuming the links between the different parameters as given by the Standard model. Therefore, a direct measurement can be seen as a test of the validity of the model itself. Furthermore, since the mass of the W boson depends to a certain degree on the mass of the Higgs boson, a precise knowledge of the W mass together with other Standard Model parameters restricts the allowed range of the mass of the Higgs boson, the so far unobserved ingredient of the model. This knowledge is important for experimentalists who attempt to discover the Higgs boson.

At energies available in electron-positron collisions at the Large Electron-Positron Collider at CERN, real pairs of $W^{\pm}$ bosons can be produced. Measuring their decay products allows the reconstruction of the mass of the $W^{\pm}$ boson. Since the W boson can decay into both, a pair of quarks and leptons, the measurement is performed separately in the three channels: the hadronic, the semi-leptonic and the leptonic channel. The analysis performed and described in this thesis covers the measurement of the mass of the W boson in the hadronic channel, where both W bosons decay into quark-antiquark pairs. Reconstructing the momenta of these quarks and pairing them correctly allows the extraction of the two W masses for each event. Unfortunately, the quarks themselves cannot be observed, since they cannot exist as isolated particles as described by Quantum Chromodynamics. The quarks fragment in showers—the so-called jets—of hadronic particles which can be measured by the detector surrounding the collision point. This effect leads to a signature of four high energetic jets, each pointing more or less into the direction of the initial quark momentum. In some hadronic W decays it happens that an initial parton radiates a high energetic gluon, which itself leads to a hadronic shower. If the jet, originating from such a gluon, is significantly separated from the initial quark, the event might not be properly reconstructed when treated as four jets. The analysis performed in this thesis focuses on the improvement of the W mass measurement by reconstructing such events as five jets. The influence on both the statistical and the systematic uncertainty of the W mass measurement from an inclusion of 5-jet events is studied and the current OPAL analysis, performed with 183 pb^{-1} of data from $e^{+}e^{-}$ collisions at a centre-of-mass energy of 189 GeV, is optimised.

Chapter 2

The Standard Model

The Standard Model describes the interactions of matter apart from the gravitation as a gauge theory based on $SU(3)_c \otimes SU(2)_L \otimes U(1)_Y$ symmetry groups.

The known fundamental[1] particles can be divided into two main groups: fermions, spin 1/2 particles and bosons, particles with spin 1. While fermions are referred to as the particles that matter is built of, the gauge bosons are responsible for the interactions, i.e. the forces between fermions arise from the exchange of gauge bosons.

In addition to these gauge bosons, the mediators of the interactions, there is another boson, the so-called Higgs boson, which is also part of the Standard Model. The existence of this spin 0 particle is a consequence of the Higgs mechanism of spontaneous symmetry breaking which is needed to provide the heavy electroweak gauge bosons, the $W^{\pm}$ and the Z^0 boson, with masses.

The following paragraphs describe the properties of the fermions and their interactions as known to date.

2.1 Fundamental Fermions

There are two groups of fundamental fermions: six leptons, six quarks in three *colours* and their associated anti-particles. All fundamental fermions that experience the strong force (see section 2.2.2) are the quarks, all the other belong to the group of leptons. Both, quarks and leptons occur in three families of the same structure. The first family, of which most stable matter is made, contains the up (u) and the down (d) quark, the electron (e^-), its neutral partner the electron neutrino (ν_e) and in addition of course the four anti-particles $\bar{u}$, $\bar{d}$, e^+ and $\bar{\nu}_e$. The second family is made of the charmed quark (c), the strange quark (s), the muon (μ), the muon neutrino (ν_μ) and the associated antifermions ($\bar{c}$, $\bar{s}$, μ^+ and $\bar{\nu}_\mu$), while the last family consists of the top quark (t), the bottom quark (b), the tau lepton (τ) and the tau neutrino (ν_τ) with the corresponding antiparticles $\bar{t}$, $\bar{b}$, τ^+ and $\bar{\nu}_\tau$. The main differences between the three different families are their masses, increasing from family 1 to 3.

2.2 The Forces

Among the four known forces of nature, gravitation is not part of the Standard Model (SM). However, there have been serious theoretical attempts to include the gravitational force into the framework of particle physics. At energy scales accessible to today's colliders, the gravitation can be neglected in

---

[1]Fundamental particles are believed to be elementary, i.e. they do not show any inner structure.

the framework of particle physics because of its weakness in comparison to the electro-magnetic, the strong and the weak force.

2.2.1   The Electro-Magnetic Force

Quantum Electro Dynamics (QED), the theory of the electro-magnetic interaction, is one of the most precisely tested theories in physics. As a motivation for the following sections, the gauge principle will be briefly introduced at the example of the electro-magnetic force.

Starting from the gauge invariance of the Maxwell equations one can see the existence of the photon as a consequence of an underlying postulate. This postulate is the invariance of the equation of motion for a spin $1/2$ particle (like the electron) under local phase transformations of the wave function $\psi(x)$ with the phase $q\chi(x)$:

$$\psi'(x) = e^{iq\chi(x)}\psi(x). \tag{2.1}$$

The equation of motion for an electron in vacuum, the Dirac equation, has to be completed by an additional term which includes a vector field $A_\mu(x)$ in order to absorb the distortion from the phase transformation. Both, the phase transformation of the wave function (2.1) and a simultaneous transformation of the vector field

$$A'_\mu(x) = A_\mu(x) - \partial_\mu \chi(x), \tag{2.2}$$

leave the equation

$$\left(i\gamma^\mu \partial_\mu - m\right)\psi(x) = q\gamma^\mu A_\mu(x)\psi(x) \tag{2.3}$$

unchanged. Herein γ^μ denotes the Dirac matrices, and m is the mass of the electron. The transformations (2.1) and (2.2) are called gauge transformations. The invariance of equation (2.3) is called local gauge invariance under the $U(1)$ symmetry group. Furthermore, it is possible to bring equation (2.3) back into the shape of the Dirac equation

$$\left(i\gamma^\mu D_\mu - m\right)\psi(x) = 0 \tag{2.4}$$

using the definition of the *covariant derivative*

$$D_\mu = \partial_\mu + iqA_\mu(x). \tag{2.5}$$

The equation for a vector field, the *Proca* equation

$$\partial_\mu F^{\mu\nu} + m_A^2 A^\nu = 0 \tag{2.6}$$

with $F^{\mu\nu} = \partial^\mu A^\nu - \partial^\nu A^\mu$, is not invariant under the transformation (2.2) unless the mass m_A of the boson is zero. Therefore, the gauge boson arising from the local gauge invariance has to be massless. A massive gauge boson would imply a finite range of the interaction. This interaction would not be able to compensate the local phase transformation of the wave function indiscriminately anywhere in space, even at large distances.

2.2.2 The Strong Force

The theory of the strong interaction, Quantum Chromodynamics (QCD), can also be formulated as a gauge theory. Analogically to QED, QCD describes the strong force between the quarks in form of a $SU(3)$ symmetry group, involving eight massless gluons as the exchange particles. The strong force is about 100 times stronger than the electro-magnetic force but has a range of less than 10^{-15} m. Contrary to the neutral photons, gluons carry the strong charge - the so-called colour charge - themselves, which allows them to interact with each other.

A feature of QCD, asymptotic freedom, explains the non-existence of free quarks. The coupling constant α_s of the strong interaction increases with separation of the quarks. Consequently, it is energetically more favourable for quark-antiquark pairs to be created from the vacuum, in order to bind the separating quarks, than for quarks to exist completely isolated. On the other hand, at small distances, e.g. in deep inelastic scattering, they can be considered as quasi free. This feature also allows the application of perturbation calculus at high energies, because α_s is sufficiently small, while the hadronization cannot be calculated perturbatively.

2.2.3 The Weak Force

A theory of a new interaction, the weak force, was needed to explain the β decays of nuclei. Enrico Fermi formulated the first theory of a weak decay in 1934. The interaction was assumed to be point like, which is a good approximation given the short range of the weak force for comparably low energies[2].

At higher energies however, the theory was condemned to break down, as the scheme of a contact interaction would violate unitarity constraints. Thus a QED like approach with charged exchange particles was needed. The W boson was then postulated and with it a neutral partner, the Z^0 boson, to provide unitarity of this theory.

If one for instance considers a doublet of an electron and a neutrino, the electron's and neutrino's wave function becomes a product of the lepton wave function $\psi_l(x)$ and the iso-spinor

$$\chi_e = \begin{pmatrix} 1 \\ 0 \end{pmatrix}, \chi_\nu = \begin{pmatrix} 0 \\ 1 \end{pmatrix}. \tag{2.7}$$

Under the assumption that the charged weak current couples to both the electron and the neutrino with equal strength, one can follow the path of phase transformation as described for QED:

$$\psi' = e^{\frac{i}{2}\vec{\tau}\cdot\vec{\alpha}(x)}\psi. \tag{2.8}$$

This is a rotation in the two dimensional space of the weak iso-spin, where $\vec{\tau} = (\tau_1, \tau_2, \tau_3)$ are the Pauli matrices and $\vec{\alpha}(x)$ denote the three rotation angles. Transformations of this kind belong to the $SU(2)$ group.

Similarly to the QED case (see section 2.2.1), the three external vector fields W_1^μ, W_2^μ and W_3^μ are needed to compensate the local phase transformation (2.8) in order to get an invariant description of the lepton in a weak field. These three quantum fields could easily be misinterpreted as the three exchange bosons needed for the weak theory.

---

[2]Since the range of the weak force is negligible when the momentum transfer is much smaller than the mass of the W or Z^0 boson, a point like interaction is a good approximation at low energies.

2.2.4   The Electroweak Unification

The simple composition $U(1)_{em} \otimes SU(2)_{weak}$ of the QED and the weak sector does not describe the particles' behaviour appropriately. The fact, that charged weak currents only couple to left handed fermions plus the fact that there is no experimental indication for the existence of right handed neutrinos, demands a joint treatment of both the electro-magnetic and the weak force. Furthermore, the neutral boson of a weak theory, as described above, does not match the Z^0 boson observed in nature.

In the weak theory one can see particles that can change their identity through an emission of a weak field quantum as multiplets of the weak iso-spin I. The left handed (right handed) fermions (anti-fermions) build doublets with $I = 1/2$:

$$\begin{pmatrix} e \\ \nu_e \end{pmatrix}_L \begin{pmatrix} \mu \\ \nu_\mu \end{pmatrix}_L \begin{pmatrix} \tau \\ \nu_\tau \end{pmatrix}_L \begin{pmatrix} u \\ d' \end{pmatrix}_L \begin{pmatrix} c \\ s' \end{pmatrix}_L \begin{pmatrix} t \\ b' \end{pmatrix}_L \begin{matrix} I_3 = 1/2 \\ I_3 = -1/2 \end{matrix}. \tag{2.9}$$

The right handed (left handed) charged leptons and quarks (anti-leptons and anti-quarks) do not couple to the W boson and therefore belong to the singlets

$$e_R^-, \mu_R^-, \tau_R^-, u_R, d_R, c_R, s_R, t_R, b_R \quad (I = 0). \tag{2.10}$$

I_3 is the third component of the weak iso-spin I. The weak eigenstates of down-type quarks, $d_i' = \sum_j V_{ij} d_j$ which are superpositions of the quarks, couple to the $W^\pm$ bosons. The unitary mixing matrix V_{ij} is referred to as the Cabbibo-Kobayashi-Maskawa (CKM) matrix. The consequence of the fact, that V_{ij} differs from the unit matrix, manifests itself in the instability of hadrons made of quarks from the second and third family[3].

A simultaneous treatment of both the electro-magnetic and the weak sector with $SU(2)_L \otimes U(1)_Y$ transformations, Y being the *hyper-charge* $Y = 2Q_{em} - 2I_3$, serves as a better description.

$SU(2)_L \otimes U(1)_Y$ transformations lead to the two fields W_1^μ, W_2^μ responsible for the charged bosons and two additional neutral fields W_3^μ and B^μ. The physical fields are linear combinations of these four fields:

$$W^{(\pm)\mu} = \frac{1}{\sqrt{2}} \left(W_1^\mu \pm i W_2^\mu \right), \tag{2.11}$$

$$Z^\mu = -B^\mu \sin\theta_W + W_3^\mu \cos\theta_W, \tag{2.12}$$

$$A^\mu = B^\mu \cos\theta_W + W_3^\mu \sin\theta_W. \tag{2.13}$$

θ_W denotes the electroweak mixing angle which is a free parameter of the electroweak theory. It is in principal determined by matching the fields A^μ and Z^μ with the photon and the neutral weak field, respectively.

Despite the fact that Van t'Hooft showed in 1971 that the electroweak theory (and generally any gauge invariant theory incorporating massless gauge bosons) is renormalizable, which is one of this theory's most important features, there was still the problem that gauge bosons themselves have to be massless in order to provide gauge invariance for their own equations of motion as well. Obviously this contradicts the high masses observed for the W and the Z^0 boson.

---

[3]Recent measurements of atmospheric and solar neutrinos strongly suggest that the neutrinos have non-zero masses. In this case a matrix similar to the CKM matrix, the Maki-Nakagawa-Sakata lepton mixing matrix, can be introduced to describe the mixing between the different neutrino generations.

2.3 The Higgs Mechanism

One of the most beautiful aspects of gauge theories, such as QED and QCD, is the renormalizability of gauge invariant models. Furthermore, the postulation of gauge invariance to the equations of motion of an electron naturally leads to a vector field — the photon, which prior to this had to be applied to the theory without any real grounds in motivation.

The arising vector fields, e.g. the electro magnetic field, has its own Lagrangian

$$\mathscr{L} = -\frac{1}{16\pi}F^{\mu\nu}F_{\mu\nu} + \frac{1}{8\pi}m^2 A^\nu A_\nu, \tag{2.14}$$

which is the Proca Lagrangian[4] for a spin 1 particle with $F^{\mu\nu} = \partial^\mu A^\nu - \partial^\nu A^\mu$. The Proca Lagrangian itself is not invariant under gauge transformations (2.2), unless m equals zero. The zero-mass constraint fits perfectly to the photon and the gluons, which are assumed to be massless, but it certainly does not apply to the heavy bosons of the electroweak force, the Z^0 and the W bosons. This section describes the Standard Model approach of the Higgs mechanism, involving spontaneous symmetry breaking, in order to provide the weak bosons with masses without giving up gauge invariance.

For simplicity, the Higgs mechanism for a weak iso-spin singlet will be described in detail in the following paragraphs. Introducing a complex scalar field, the Higgs field $\phi = \phi_R + i\phi_I$, one can formulate a spin 0 Lagrangian consisting of a kinematic term T and a potential U:

$$\mathscr{L} = \underbrace{\frac{1}{2}(\partial_\mu \phi)^*(\partial^\mu \phi)}_{T} + \underbrace{\frac{1}{2}\mu^2(\phi^*\phi) - \frac{1}{4}\lambda^2(\phi^*\phi)^2}_{-U}. \tag{2.15}$$

The system can now be made invariant under local phase transformations

$$\phi \to e^{i\theta(x)}\phi \tag{2.16}$$

by applying the usual method of introducing a massless gauge field A^μ and replacing the derivatives in equation (2.15) with covariant derivatives (2.5):

$$\begin{aligned} \mathscr{L} =& \frac{1}{2}\left[(\partial_\mu - iqA_\mu)\phi^*\right]\left[(\partial_\mu + iqA_\mu)\phi\right] \\ &+ \frac{1}{2}\mu^2(\phi^*\phi) - \frac{1}{4}\lambda^2(\phi^*\phi)^2 - \frac{1}{16\pi}F^{\mu\nu}F_{\mu\nu}. \end{aligned} \tag{2.17}$$

Since The Feynman calculus is a perturbation procedure that starts from the ground state, the vacuum, it is suggested to introduce the new fields η and ξ, which are fluctuations about one of the possible ground states $\phi_{I\,min}^2 + \phi_{R\,min}^2 = \frac{\mu^2}{\lambda^2}$ of U, for instance:

$$\eta = \phi_R - \frac{\mu}{\lambda} \quad \xi = \phi_I. \tag{2.18}$$

Note that, since the potential U is symmetric with respect to rotations in the ϕ_R-ϕ_I plane, by choosing one of the possible ground states, the symmetry of the potential itself is *hidden*. The symmetry is said to be spontaneously *broken*. The Lagrangian is symmetric, i.e. it is invariant under rotations of ϕ in the complex plane. However, when written with the new variables, it is then found not to be invariant

---

[4]The Lagrangian density function $\mathscr{L}$ of a field is an equivalent description of the field's properties than the equation of motion of the particle itself. The two descriptions are linked through the application of the Euler-Lagrange equation to the Lagrangian.

even under the interchange of η and ξ, despite the fact that both formulations display exactly the same physics. This behaviour is the consequence of the Higgs potential itself being symmetric, but any certain ground state, like $\eta = \xi = 0 \iff \phi_R = \mu/\lambda; \; \phi_I = 0$, no longer shares this symmetry.

In the new variables η and ξ, the Lagrangian (2.17) becomes

$$
\begin{aligned}
\mathscr{L} = & \left[\frac{1}{2}(\partial_\mu \eta)(\partial^\mu \eta) - \mu^2 \eta^2 \right] + \left[\frac{1}{2}(\partial_\mu \xi)(\partial^\mu \xi) \right] \\
& + \left[-\frac{1}{16\pi} F^{\mu\nu} F_{\mu\nu} + \frac{1}{2}\left(q\frac{\mu}{\lambda} \right)^2 A_\mu A^\mu \right] - 2i\left(q\frac{\mu}{\lambda} \right)(\partial_\mu)A^\mu \\
& + \left\{ q[\eta(\partial_\mu \xi) - \xi(\partial_\mu \eta)]A^\mu + q^2\frac{\mu}{\lambda}\eta(A_\mu A^\mu) + \frac{1}{2}q^2(\xi^2 + \eta^2)(A_\mu A^\mu) \right. \\
& \left. - \frac{1}{4}\lambda^2(\eta^4 + 2\eta^2\xi^2 + \xi^4) \right\} + \left(\frac{\mu^2}{2\lambda} \right)^2 .
\end{aligned}
\tag{2.19}
$$

The terms in the first line can be identified with a single massive (η) and one additional massless (ξ) scalar particle. The second line describes a vector field A^μ which has now acquired the mass $m_A = 2\sqrt{\pi}\frac{q\mu}{\lambda}$ (compare to equation 2.14), while the term in curled brackets describes the various couplings of ξ, η and A^μ. The constant term $(\mu^2/2\lambda)^2$ is irrelevant, it has no effect on the field equations. Not quite understandable is only the term for the massless vector field ξ since it is not observed in nature, although it should be easy to identify. Also there is one disturbing term in the second line

$$
-2i\left(q\frac{\mu}{\lambda} \right)(\partial_\mu)A^\mu,
\tag{2.20}
$$

which can hardly be explained. Fortunately it turns out that both terms, the so-called Goldstone boson ξ and the term (2.20) disappear if one only finds a local gauge transformation which gives a real ground state: Rotating ϕ in the complex plane

$$
\phi' = \begin{pmatrix} \cos\theta & -\sin\theta \\ \sin\theta & \cos\theta \end{pmatrix} \begin{pmatrix} \phi_R \\ \phi_I \end{pmatrix} \qquad \text{with } \theta = -\arctan\frac{\phi_R}{\phi_I}
\tag{2.21}
$$

reduces e.q. (2.19) to

$$
\begin{aligned}
\mathscr{L} = & \left[\frac{1}{2}(\partial_\mu \eta)(\partial^\mu \eta) - \mu^2 \eta^2 \right] + \left[-\frac{1}{16\pi} F^{\mu\nu} F_{\mu\nu} + \frac{1}{2}\left(q\frac{\mu}{\lambda} \right)^2 A_\mu A^\mu \right] \\
& + \left\{ q^2\frac{\mu}{\lambda}\eta(A_\mu A^\mu) + \frac{1}{2}q^2\eta^2(A_\mu A^\mu) - \lambda\mu\eta^3 - \frac{1}{4}\lambda^2\eta^4 \right\} + \left(\frac{\mu^2}{2\lambda} \right)^2 ,
\end{aligned}
\tag{2.22}
$$

which describes a massive scalar (the Higgs boson), a massive gauge field A^μ and their couplings.

The same procedure—with a slightly more complicated Higgs potential—can be applied to the whole electroweak sector in order to provide the W and the Z^0 boson with mass terms while leaving the photon massless. Note that there is a whole variety of Higgs potentials which could all serve the same purpose, but all of them have in common that they imply at least one massive scalar. Since the Higgs boson has not been observed yet[5], one cannot tell the actual shape of its potential. For a more complete description of the electroweak theory and the Higgs mechanism see [1, 2, 3].

---

[5]It is believe that the Higgs mass could be beyond the reach of today's colliders.

2.4 The Mass of the W Boson

Taking into account only lowest order perturbation calculus, the mass of the W boson is determined by

$$M_W = M_Z \cos \theta_W = \sqrt{\frac{\pi \alpha}{\sin^2 \theta_W \sqrt{2} G_F}} = \frac{v g_W}{2}, \tag{2.23}$$

where M_Z is the mass of the Z^0 boson and g_W denotes the coupling to the W boson defined by $g_W = g_e / \sin \theta_W$. The Fermi constant G_F is determined by the decay rate of muons to electrons and v is the vacuum expectation value $v = \frac{\mu}{\lambda}$ of the Higgs sector (see section 2.3).

Indirect measurements of M_W were made at LEP by precision measurements at the Z^0 resonance. They lead to a value of the W mass of $M_W^{\text{indirect}} = 80.376 \pm 0.034$ GeV [4]. A direct observation of decays of real W bosons therefore serves as a check of the Standard Model. A direct measurement from the UA1 experiment [5], where—together UA2 [6]—the W boson was discovered, leads to a mass of $M_W^{\text{direct}} = 82.7 \pm 1.0^{stat.} \pm 2.7$ GeV from $W \to e\nu$ events. Taking higher order corrections into account, M_W is sensitive to the mass of the Higgs boson, and therefore provides an indirect measurement of the mass of the latter that has never been observed as a real particle so far. The following equation shows the next order dependencies of M_W on the mass of the Higgs boson and the top quark:

$$M_W^2 = \frac{\pi \alpha}{\sin^2 \theta_W \sqrt{2} G_\mu} \left\{ 1 + \frac{3 G_\mu}{8 \pi^2 \sqrt{2}} M_t^2 + \frac{2 G_\mu}{16 \pi^2} M_W^2 \left[\frac{11}{3} \ln \frac{M_H^2}{M_W^2} + ... \right] \right\}. \tag{2.24}$$

The origin of these corrections arise from the one-loop corrections to the W propagator as illustrated in figure 2.1. The sensitivity of the mass of the W boson to both the mass of the top quark and the Higgs boson is shown in figure 2.2.
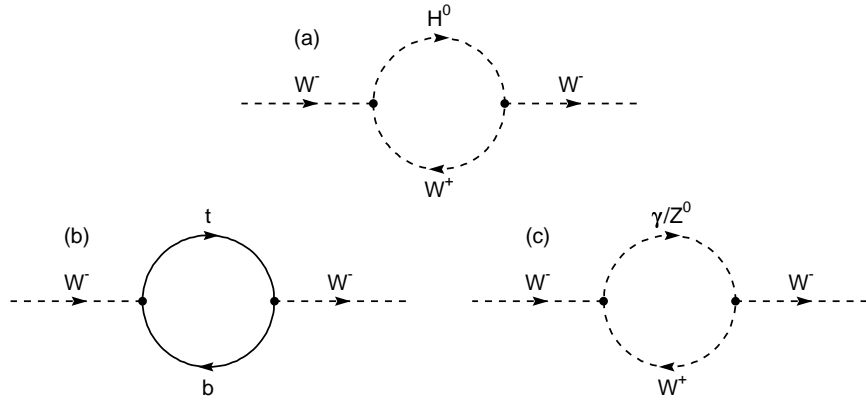
Figure 2.1: One-loop corrections to the W propagator involving virtual top quarks (a), Higgs (b) and γ/Z^0 bosons (c).
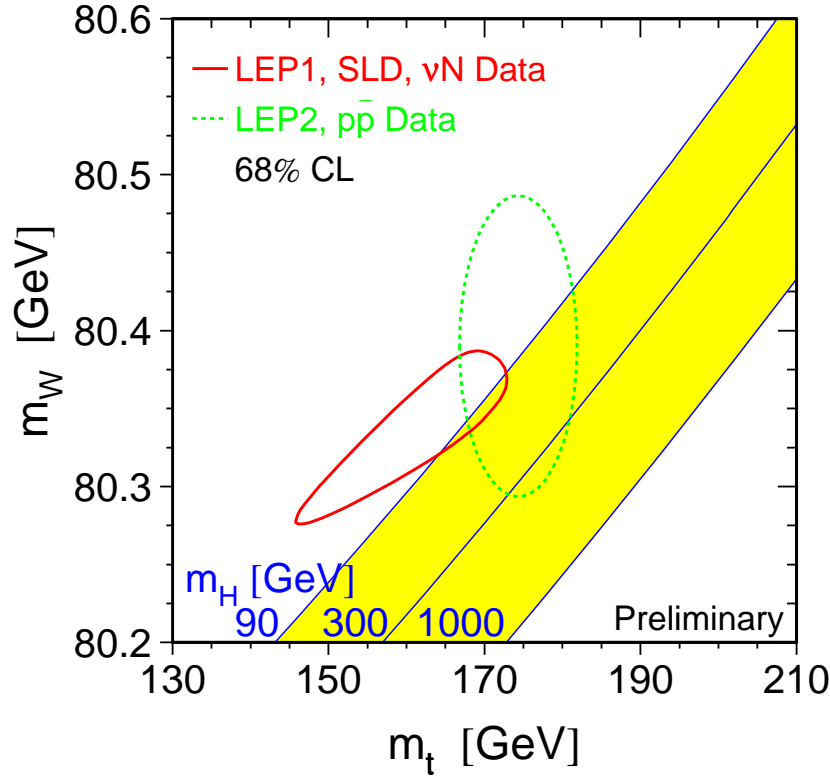
Figure 2.2: Measurement of M_W and M_t in 1997. The indirect prediction (solid line) comes from precision electroweak data and is compared to direct measurements from LEP2 and Tevatron (dashed line).

2.5   Production and Decay of W Bosons

Above the threshold of $\sqrt{s} \gtrsim 161$ GeV $\approx 2M_W$ there is enough energy available for a pair of real W bosons to be created in e^+e^- collisions. This section summarises the calculation of the W^+W^- cross-section and branching ratios. A more detailed description can be found in [7].

The knowledge of the WW production cross section σ_{WW}, calculated within the theoretical framework of the SM, allows the determination of expected WW events if both, the integrated luminosity

$$L = \int_t \mathscr{L}(t)dt, \tag{2.25}$$

where $\mathscr{L}(t)$ is the luminosity as defined in equation 3.1, and the efficiency of the applied event selections and reconstructions, are known.

2.5.1   On-shell production

In e^+e^- collisions, pairs of W bosons can in principle be produced via two processes, the e^+e^- annihilation and the neutrino exchange, as illustrated by the lowest order Feynman graphs in figure 2.3.

Considering the W bosons as stable particles with infinite lifetimes allows the analytical calcu-
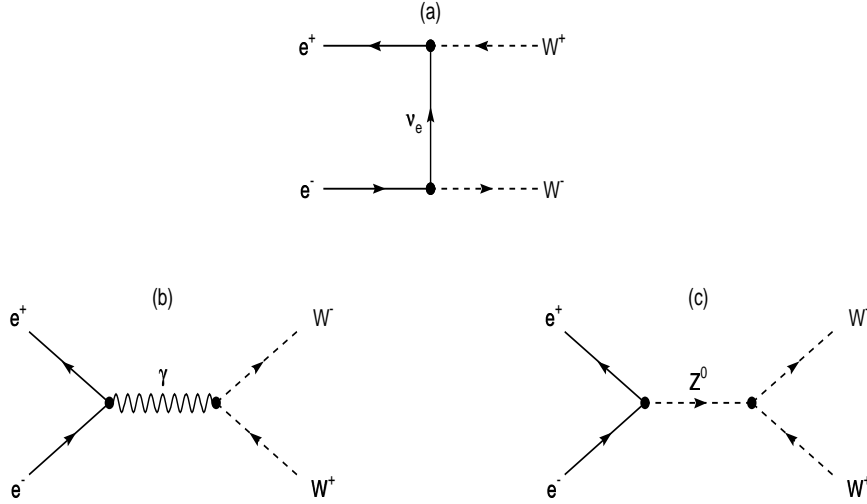
Figure 2.3: Lowest order Feynman diagrams of the W^+W^- production processes: the neutrino exchange (a) and the electron-positron annihilation to a photon (b) and a Z^0 boson (c).

lation of the on-shell WW cross-section in the Born approximation[6] using Feynman rules [3] and assuming unpolarised e^+e^- beams. This leads near the production threshold where the W bosons are produced virtually at rest to the W^+W^- cross section

$$\sigma_{WW}^0 = \frac{\pi\alpha^2}{s}\frac{1}{4\sin^2\theta_W}4\beta + \mathscr{O}(\beta^3), \tag{2.26}$$

where α is the electro magnetic coupling constant at zero momentum transfer, s denotes the centre-of-mass energy squared and $\beta = \sqrt{1 - M_W^2/E_{beam}^2}$ expresses the velocity of the W bosons in the rest frame. This cross-section is dominated by the t-channel neutrino exchange diagram ($\sim \beta$) whereas the s-channel annihilation diagrams and s-t interference terms go like β^3.

2.5.2 Off-shell Production of W^+W^- Pairs

Although equation 2.26 is already a good approximation, the cross section for the production of W boson pairs must be calculated together with all other possible 4-fermion final states to correctly account for interference effects, since the W bosons are unstable particles. Still, for matters of convenience, the W^+W^- production cross section σ_{WW} is often considered separately from other 4-fermion processes since the interference effects are predicted to be small:

$$\sigma_{4f} = \sigma_{WW} + \sigma_{other}. \tag{2.27}$$

Non-WW 4-fermion processes, such as the Z^0-pair and the single-W production and the $e^+e^- \rightarrow Z^0e^+e^-$ process, are illustrated by the lowest order Feynman diagrams in figure 2.4. These processes are treated as background in the measurement of the mass of the W boson. The curly lines in the

---

[6]Herein the Born approximation is the lowest order calculation of the processes in figure 2.3, the so-called "CC03" Feynman diagrams.
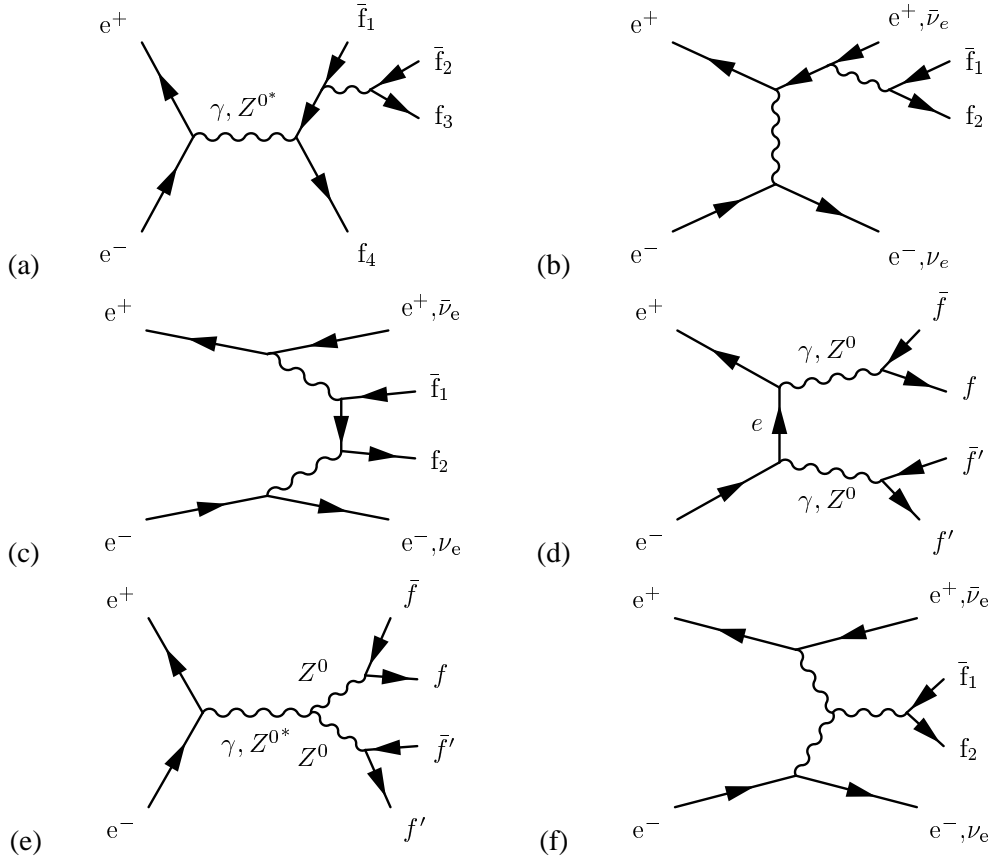
Figure 2.4: Non-*WW* 4-fermion processes and their lowest order Feynman diagrams: (a) Abelian annihilation, (b) bremsstrahlung, (c) multi-peripheral conversion, (d) conversion, (e) non-Abelian annihilation and (f) fusion process.

Feynman graphs of figure 2.4 correspond to photon, Z^0 or $W^\pm$ boson exchange unless otherwise indicated. The Z^0-pair production belongs to the processes in figure 2.4 (d) and (e), single-W production is represented by figure 2.4 (a), (b) and (f) as well as the process $e^+e^- \rightarrow Z^0e^+e^-$.

The contribution of the WW production to the 4-fermion cross-section can be written as

$$\sigma_{WW} = \sigma_{WW}^0(1 + \delta_{EW} + \delta_{QCD}) + ... \tag{2.28}$$

δ_{EW} and δ_{QCD} stand for one-loop electroweak and QCD corrections while the ellipses denote higher orders. Semi-analytical calculations of the W^+W^- production cross-section for a hypothetical W mass of $M_W = 80.33$ are shown in figure 2.5, as well as measurements performed with LEP data [8]. The dashed curve also shows the expected cross-section in the absence of ZWW couplings as well as only with ν_e exchange. Figure 2.6 shows the SM cross sections of processes in the energy region available at LEP2. One can clearly see the strong increase of the cross section for the W^+W^- production σ_{WW} just at the threshold. Note that the shown function for these processes are—mainly at the production threshold—depending on the mass of the W boson itself. The cross sections for different production channels and the dominant background processes relevant for the 4-quark channel are shown in table 2.1 for the centre-of-mass energy of $\sqrt{s} = 189$ GeV, at which the data used in this analysis, was taken.
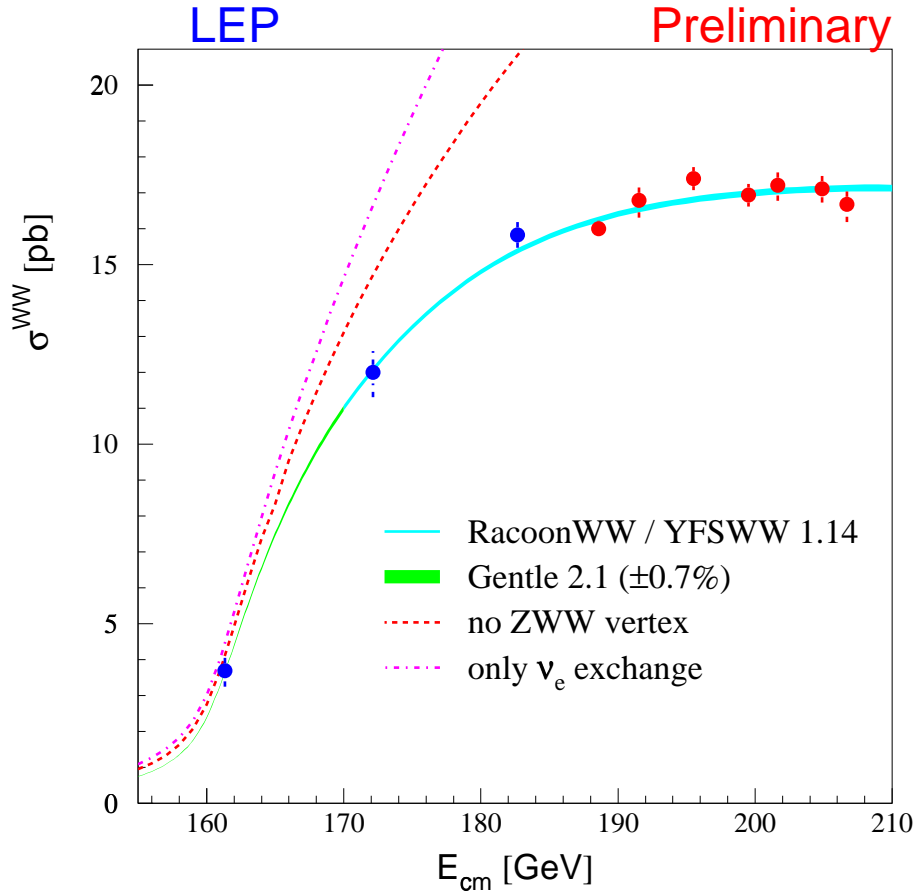
Figure 2.5: LEP measurement of the W^+W^- cross-section as a function of the centre-of-mass energy $\sqrt{s}$ compared to SM predictions [9].

Process	$\sigma[pb]$
$e^+e^- \rightarrow W^+W^- \rightarrow l^+\nu_l l^-\bar{\nu}_l$	1.76
$e^+e^- \rightarrow W^+W^- \rightarrow l\bar{\nu}_l q\bar{q}$	7.32
$e^+e^- \rightarrow W^+W^- \rightarrow q\bar{q}q\bar{q}$	7.61
$e^+e^- \rightarrow q\bar{q}(\gamma)$	98.9
$e^+e^- \rightarrow Z^0Z^0$	0.98

Table 2.1: Cross sections for Standard Model processes for both the W pair production and the most important background for the 4-quark channel at the centre-of-mass energy of $\sqrt{s} = 189$ GeV.

2.5.3 W Decay

Related to the W boson there is another important parameter: the width Γ_W. Although it can also be measured [10]—even simultaneously with the W mass—, the Standard Model allows the width to be expressed as a function of the mass. In other words: the SM contains only one free parameter for the W boson. The precision of the mass measurement can be increased by fixing Γ_W to its Standard

Model prediction

$$\Gamma_W \approx \frac{G_F M_W^3}{2\sqrt{2}\pi},\tag{2.29}$$

since only one free parameter is left.

W bosons decay into pairs of fermions, i.e. either into leptons $W \to l\bar{\nu}_l$ (31.5%) or quarks $W \to q\bar{q}'$ (68.5%) [11]. This leads to 47% hadronic, 10% leptonic and 43% semi-leptonic W^+W^- events.
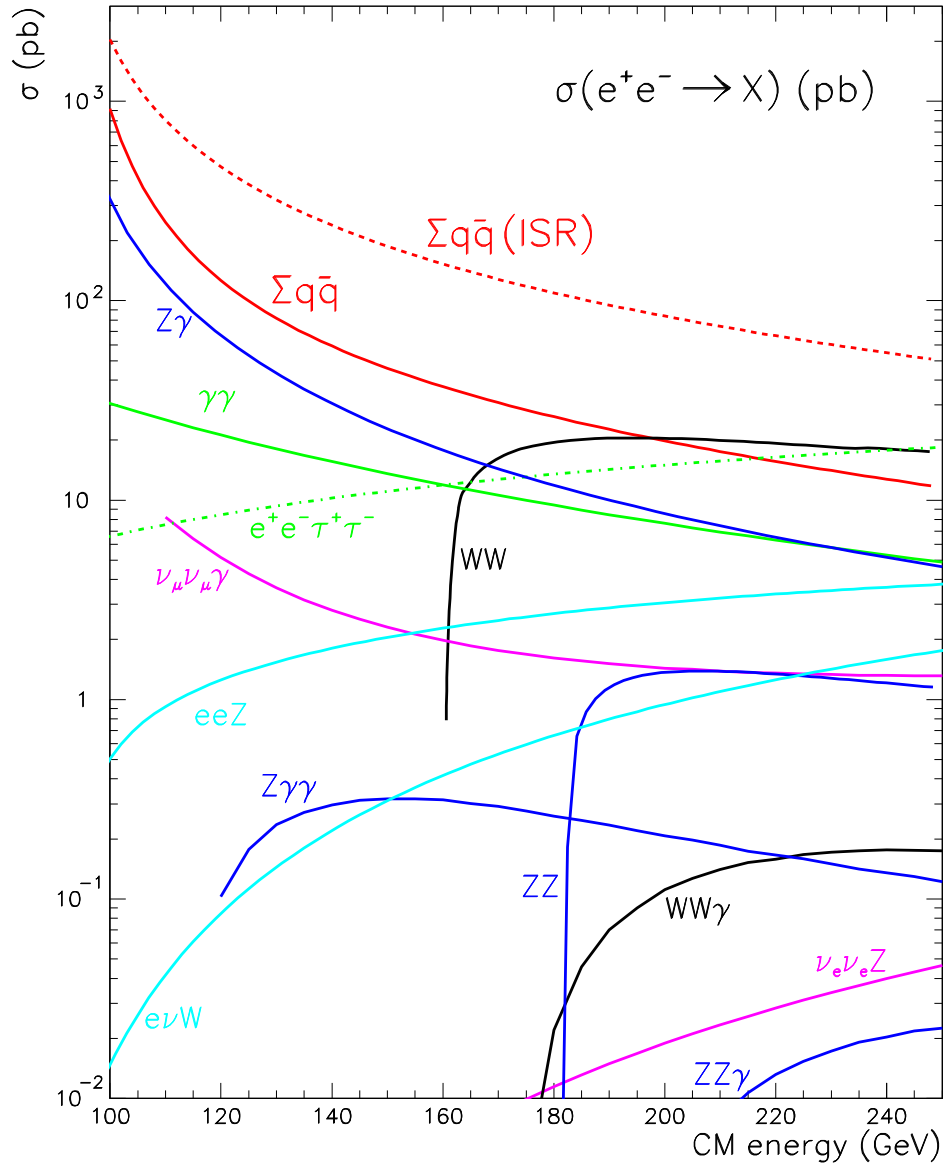
Figure 2.6: Cross sections for Standard Model processes in e^+e^- collisions at LEP2 energies.

Chapter 3

The Experiment

3.1 The Large Electron Positron Collider LEP

LEP[12], the **L**arge **E**lectron-**P**ositron Collider, is a circular accelerator for electrons and positrons, built and situated at the *European Laboratory for Particle Physics* (CERN), not far from Geneva, Switzerland.

Its main purposes are to allow precision measurements of the properties of the mediating bosons of the weak interaction, tests of the Standard Model and the search for the Higgs boson, as well as searches for other particles, predicted by extensions of the Standard Model.

During its first five years of operation (1989-1994, known as the LEP1 era) the LEP accelerator provided the four Experiments ALEPH, DELPHI, L3 and OPAL with electron-positron collisions at centre-of-mass energies in the vicinity of the mass of the Z^0 boson. From 1995 on, after a major technical upgrade of LEP, the centre-of-mass energy was increased to values above the production threshold of pairs of W bosons (LEP2).

3.1.1 The LEP Machine

Generally, collision experiments take place in three different steps: the initial production and injection of the particles, the following chain of successive acceleration and finally the collision itself. The LEP accelerator is only the last part of a cascade of pre-accelerators at CERN as schematically illustrated in figure 3.1. The process of acceleration starts in the **L**EP **I**njector **L**inacs (LIL), followed by the **E**lectron-**P**ositron **A**ccumulator ring (EPA). The two "proton" synchrotrons PS and SPS (**S**uper **P**roton **S**ynchrotron) successively accelerate the leptons to even higher energies, before they enter the LEP machine. When the LEP ring is filled with a sufficient number of electrons and positrons, they are accelerated to the desired energy by radio frequency cavities (RF). The principal characteristics of LEP are listed in table 3.1.

In the first part of LIL, the extracted electrons are accelerated to an energy of 200 MeV and part of them are directed onto a tungsten target in order to produce the positrons. Then the electrons and positrons are further accelerated to 600 MeV before they enter the EPA ring, where they are grouped to bunches, destined to the PS. Having reached an energy of 3.5 GeV in the PS, the bunches of electrons and positrons are filled into the SPS accelerator where they are further accelerated up to 22 GeV before they are filled into the LEP ring.

LEP itself consists of eight straight sections of about 300 m length and curved parts in between where the orbit of the particles is deflected by $45°$. The four electron and the four positron bunches, travelling around the ring in opposite directions, cross in the straight sections. Only in four of them
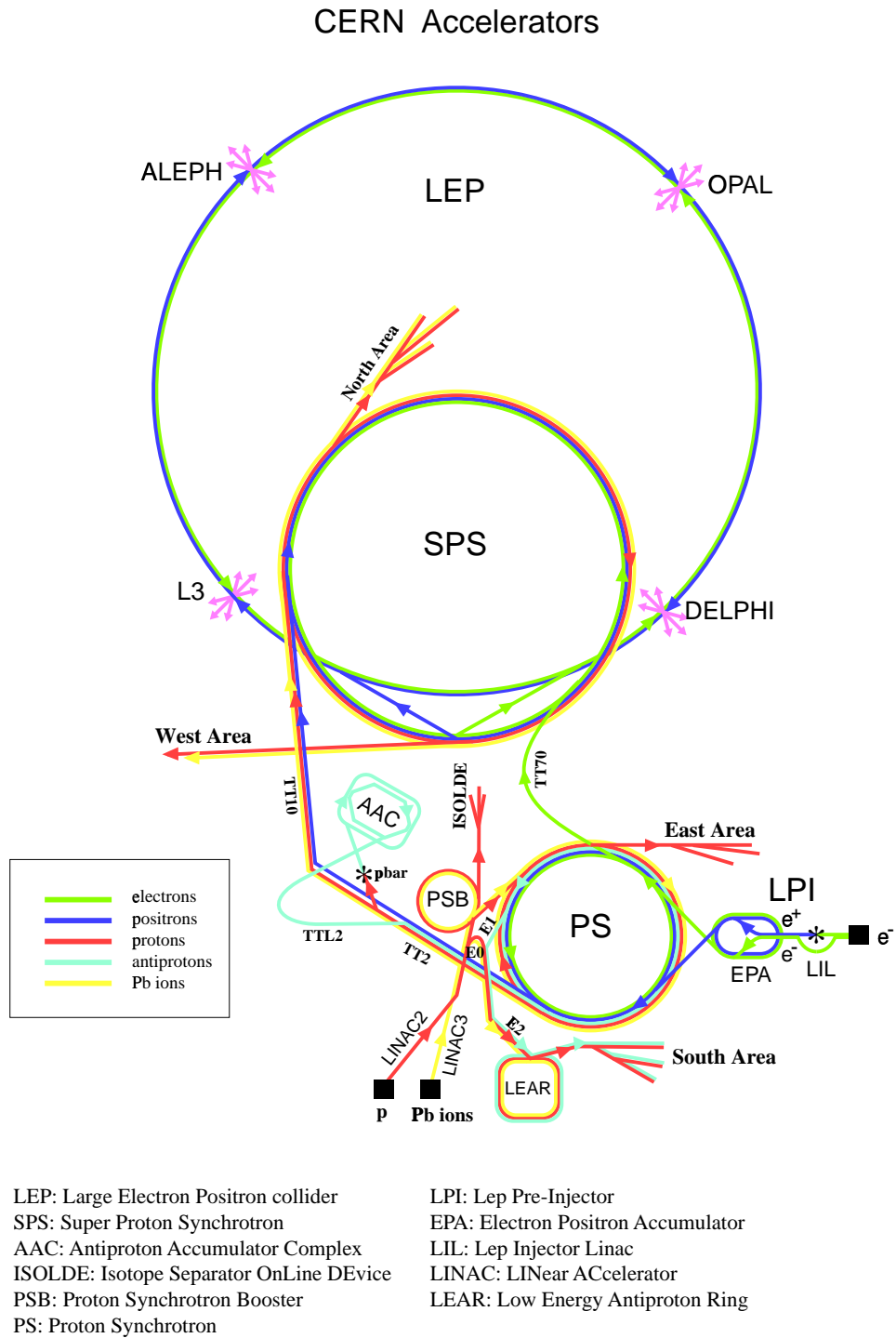
Figure 3.1: Schematic view of the accelerator system at CERN.

circumference	26659 m
mean radius of curvature	3096 m
depth of the tunnel below surface	$50 - 175$ m
diameter of the tunnel	3.8 m
number of particle bunches	$4 + 4$
spread of the bunches σ_x	200 μm
spread of the bunches σ_y	3 μm
length of the bunches σ_z	10 mm
maximum circulating current	6.3 mA
circulation frequency	11.2 kHz
maximum luminosity	10^{32} cm^{-2}s^{-1} (@ 189 GeV)
magnetic field of bending magnets	1.02 kG (@ 189 GeV)
number of dipole magnets	3368
number of quadrupole magnets	816
number of sextupole magnets	504
number of correction magnets	700
synchrotron radiation	2.28 GeV per turn (@ 189 GeV)
maximum available RF voltage	3525 MV
maximum c.m.s. energy	208.8 GeV

Table 3.1: Main characteristics of LEP in the LEP2 mode [12, 13].

the bunches are focused to provide e^+e^- collisions within the four LEP experiments. At the other four crossings, electrostatic fields separate the orbits of the electron and positron bunches in order to avoid collisions.

In the curved parts of LEP, 3368 dipole magnets deflect the particles. Another 816 quadrupole and 504 sextupole magnets correct the transversal abberation of the bunches. Close to the interaction points, super-conducting quadrupole magnets minimise the transverse dimensions of the bunches at the interaction points in order to gain as much luminosity as possible. Another 400 correcting magnets around the ring help controlling the particles' orbits. The luminosity is a machine dependent quantity that determines—together with the cross section σ—the rate dN/dt of a process:

$$\frac{dN}{dt} = \mathscr{L} \cdot \sigma. \tag{3.1}$$

At e^+e^- colliders, the luminosity, neglecting beam-beam interactions, is given by

$$\mathscr{L} = \frac{N_{e^+} N_{e^-} f}{4\pi k \sigma_x \sigma_y}, \tag{3.2}$$

where $N_{e^\pm}$ is the number of particles per beam, f is the revolution frequency, k is the number of bunches and σ_x and σ_y are the r.m.s beam radii in the plane perpendicular to the beam direction. During 1998, the maximal luminosity reached at LEP was about 10^{32}cm^{-2}s^{-1}.

Whenever a charged particle is deflected by a magnetic field, it suffers from energy loss due to synchrotron radiation. Within one turn around LEP, an electron (positron) with initial energy E emits synchrotron radiation with a total energy of

$$\Delta E_{synch} = \frac{E^4}{R_{LEP}} \cdot 8.85 \times 10^{-5} \text{GeV}^{-3}\text{m}, \tag{3.3}$$

where $R = 3096$ m denotes the mean radius of the curvature of LEP. For a centre-of-mass energy of $\sqrt{s} = 189$ GeV the energy loss through synchrotron radiation, which constantly has to be resupplied by the RF cavities, is 2.3 GeV per turn.

3.1.2   LEP Energy Measurement

The knowledge of the initial state of the collision is crucial and affects the outcome of the measurement, particularly since the measurement of the mass of the W boson applies kinematic fits imposing energy and momentum conservation (see section 4.4.1). Therefore the uncertainty of the measurement of the beam energy leads to a systematic error on the mass measurement as will be described in section 5.3.

The beam energy is evaluated by measuring the spin tune v_s, the number of electron spin precessions per turn in LEP. This measurement is performed in special runs with polarised beams. The average beam energy can be extracted via the relation

$$v_s = \frac{(g_e - 2)}{2} \frac{E_{beam}}{m_e} = \frac{E_{beam}}{0.44065 \text{ GeV}}. \tag{3.4}$$

Herein $(g_e - 2)/2$ is the anomalous magnetic moment of the electron.

During physics runs, such a polarisation measurement cannot be performed, because the beams can only be sufficiently polarised up to $E_{beam} \sim 60$ GeV. Furthermore, even at lower energies, stable collision conditions with transverse polarised beams are not achieved at LEP.

Therefore the dependency of the energy on the magnetic field

$$E_{beam} = \frac{e}{2\pi c} \oint \vec{B} \cdot \vec{dl}, \tag{3.5}$$

integrated over the orbit of the beam, is used to extrapolate the beam energy to $E_{beam} > 60$ GeV. The measurement of the bending field $\vec{B}$ is performed with 16 NMR probes installed in the dipole magnets around the LEP ring that are calibrated with measurements of the spin tune v_s in the range $41 - 61$ GeV. The linearity of the NMR probes up to LEP2 energies was tested in flux loop studies over the full range. In the calculation of the LEP energy, also time-dependent effects have to be considered, such as stray fields from the passing TGV, the French high speed train, and movements of the LEP quadrupoles with respect to the the beam due to the earth's tides as described in [14, 15].

The LEP Energy Working Group has assigned a total error of 20 MeV on the beam energy for the data taken at $\sqrt{s} = 189$ GeV in 1998 [14].

The beam energy at the OPAL interaction point does not necessarily have to be equal to the average LEP energy around the ring. Losses due to synchrotron radiation in the arcs and further acceleration in the sections to both sides of the experiment have to be taken into account.

3.2   The OPAL Detector

OPAL, the **O**mni **P**urpose **A**pparatus at **L**EP, was realized in order to study all the possible interactions produced in e^+e^- collisions at LEP with a geometric acceptance of 99% of the solid angle of 4π. A schematic view of the OPAL detector, which is extensively described in [16, 17, 18] is shown in figure 3.2. The apparatus consists of a barrel region, with subsystems arranged in concentric cylinders around the interaction point, two endcaps of subdetectors stacked in rectangular layers, covering the ends of the barrel part, and devices surrounding the beam pipe in the forward and backward regions
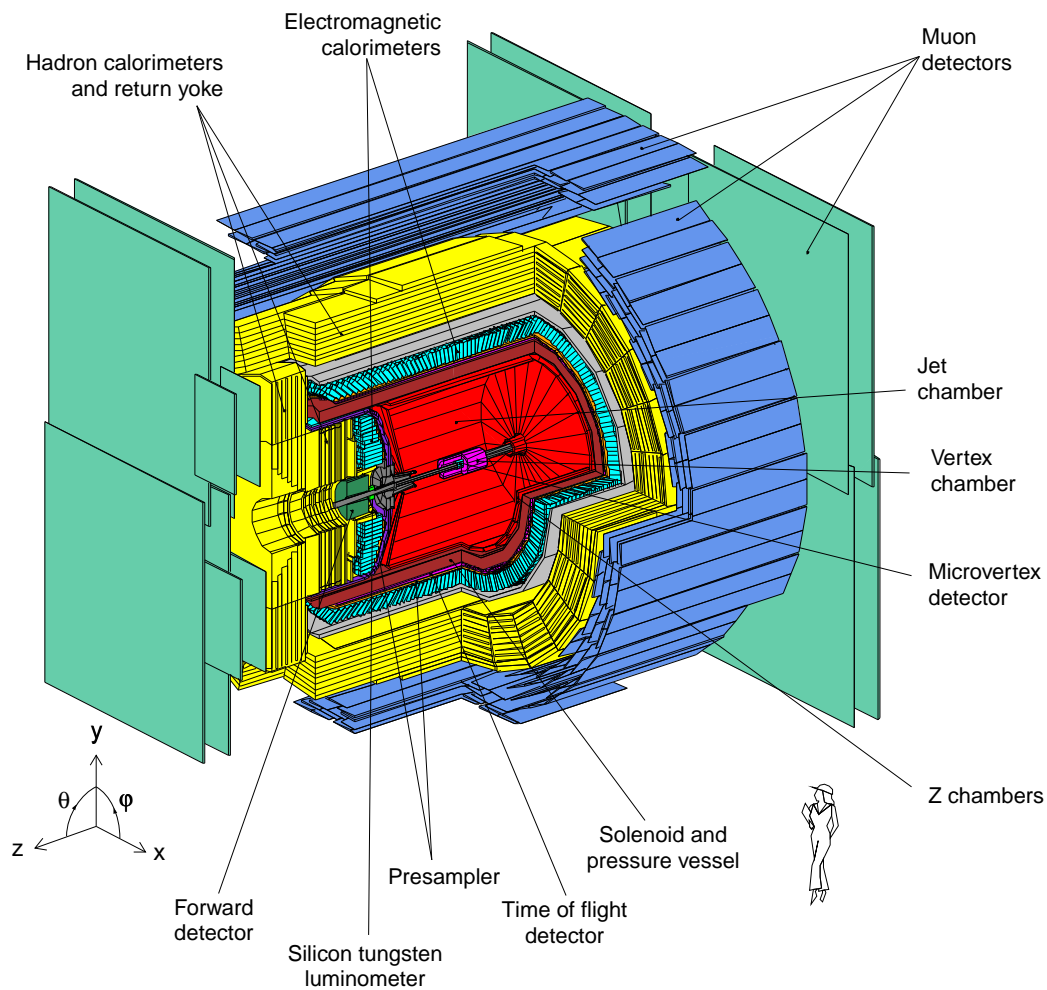
Figure 3.2: Schematic 3D view of the OPAL detector.

in order to measure small angle scattering phenomena. The Cartesian coordinate frame of OPAL is defined with its origin in the nominal interaction point such that the z axis coincides with the electron beam. The x axis points to the centre of the LEP ring and the y axis points upward. The polar and azimuthal angles of the frame are θ and ϕ, respectively. Being quasi-symmetric with respect to rotations around the beam pipe and mirroring at the $x - y$ plane, the detector's purpose is to measure momenta and energies of particles emerging from the interaction point and to determine their identity, as well as to identify secondary vertices.

3.2.1   The Tracking System

Starting with the innermost, the silicon microvertex detector, the vertex detector and the jet chamber reconstruct the trajectories of charged particles from the e^+e^- collision. While the silicon microvertex detector is a set of semiconducting microstrip layers, the rest of the tracking system consists drift chambers within a 4 bar pressured vessel filled with a gas mixture of 88.2% argon, 9.8% methane and 2.0% ISO-butane. The volume in the pressure vessel is exposed to a constant solenoidal magnetic field of 0.435 T parallel to the beam axis.

The Jet Chamber

The primary and for the W mass analysis most important tracking device in the OPAL detector is the jet chamber (CJ). It has a length of about four meters, an inner radius of 25 cm and an outer radius of 185 cm. The 24 sectors contain 159 sense wires each, interleaved with potential wires, all strung parallel to the beam axis in the $\phi - z$ plane. Cathode wire planes form the boundaries between sectors. The sense wires, staggered by ± 0.1 mm to the left and right of the $\phi - z$ plane, are 10 mm apart from each other. The maximal drift distance for electrons emerging from the ionisation of the gas is approximately 3 cm for the innermost wires and about 25 cm in the outer part of CJ. Averaged over the entire jet chamber, the typical spatial resolutions of the jet chamber are 135 μm in the $r - \phi$ plane using drift time information and 6 cm in z direction, evaluated with charge division techniques when comparing the signal from both sides of the wires.

   Since CJ provides proportional multiplication of the primary electrons close to the sense wires, the measured charge is used to determine the specific energy loss dE/dx of the high energetic particle causing the primary ionisation. Together with the knowledge of its momentum, this can be used for particle identification.

   Only tracks with $|\cos\theta| < 0.73$ can yield signals in all 159 signal wires while tracks with $|\cos\theta| \approx$ 0.98 still transverse about eight sense wires.

   The jet chamber is exposed to a magnetic field, thus measuring the curvature of tracks yield to a measurement of the transverse momentum p_{xy}, assuming the charge of the particle is ± 1, with a resolution of

$$\frac{\sigma_{p_{xy}}}{p_{xy}} \approx 2.2 \times 10^{-3} \cdot p_{xy}/\text{GeV} \quad [16] \tag{3.6}$$

for tracks from $Z^0 \to \mu^+\mu^-$ events with a maximum number of measured points.

The Z-Chambers

In order to measure the z coordinate of the particles' tracks as they exit the jet chamber, 24 Z-chambers (CZ) with sense wires perpendicular to the beam axis surround CJ, sensitive to tracks with $|\cos\theta| <$ 0.72. Their resolution is $100 - 350$ μm in z and 1.5 cm in the $r - \phi$ plane [16].

Silicon Microvertex System

Surrounding the beam pipe, a beryllium tube at a radius of 5.35 cm and 1.1 mm thick in the vicinity of the collision point, the silicon microvertex detector (SI) is installed up to a radius of 7.8 cm. It is itself surrounded by another beam pipe made of carbon fibre and thin aluminium.

The silicon microvertex detector consists of two cylindrical barrels of each two single-sided silicon detectors at 6.0 and 7.5 cm distance from the interaction point. Each cylinder is made of two microstrip detectors, glued together back-to-back: The one is sensitive to the z, the other to the ϕ direction. The purpose of the silicon microvertex system is to extrapolate the charged tracks into the insensitive region of the beam pipe in order to detect secondary vertices with high precision. Typical resolutions for the points of closest approach of the highest energy track in an event to the interaction point are 15 μm in the $r - \phi$ plane and $20 - 50$ μm in the z direction [18].

The Vertex Detector

A high resolution drift chamber, the vertex detector (CV), surrounds the outer beam pipe in two cylindrical layers of 36 sectors. It is 1 m long and extends from a radius of 8.8 cm to 23.5 cm. The inner layer contains sense wires strung parallel to the beam axis with a spacing of 0.58 cm. The outer sectors have each six "stereo" wires, 0.5 cm apart from each other and strung with an angle of 4$^{\text{o}}$ with respect to the beam axis. Measuring the drift time of the electrons from the ionisation in the gas, the resolution in the $r - \phi$ plane can be measured with an accuracy of 55 μm. A very fast z measurement, used for triggering, is performed by evaluating the time difference of the signal read out on both sides of the signal wires ($\sigma_z^{(\Delta T)} \sim 4$ cm), a more accurate determination of the z position of a track is achieved by taking both the stereo and the axial wires into account ($\sigma_z^{(stereo)} \sim 700$ μm) [16].

3.2.2   Time-of-Flight Detectors

The time-of-flight system (TOF) generates fast trigger inputs and rejects cosmic rays. The barrel part that covers a region of $|\cos\theta| < 0.82$ surrounds the magnetic coil in form of an array of 160 scintillating tiles of 684 cm length. The scintillating light, emerging from excitations in the plastic scintillator due to transversing charged particles, is read out on both sides of the scintillator bars with a total of 320 photo multipliers. An additional endcap part of the TOF, a 1 cm thick layer of scintillating tiles, is positioned just before the electro-magnetic calorimeter.

Triggered by the beam crossing signal, the TOF measures the time it takes for charged particles to reach this part of the detector at a distance of about 2.4 m from the interaction zone. A time resolution of about 220 ps can be achieved for high energetic particles [16]. With the additional information of the amplitude of the signal, the time-of-flight detector is used for charged particle identification in the $0.6 - 2.5$ GeV range.

3.2.3   Calorimeters

To measure the energy of photons, electrons and of charged and neutral hadrons, OPAL has a system of calorimeters outside the magnet coil. The particles are stopped within these detectors, leaving a signal depending on the amount of absorbed energy.

The Electro-magnetic Calorimeter

An array of about 10000 lead glass blocks, installed between the TOF and the return yoke of the magnet, forms the electro-magnetic calorimeter (ECAL). It measures the energy and the position of electro-magnetic showers by reading out the Čerenkov light in the transparent material, emitted by the highly relativistic electron-positron pairs from the electro-magnetic shower: When an energetic electron is decelerated in the field of a high-Z nucleus by emitting a photon (bremsstrahlung), this photon can—in the field of another nucleus—convert into an electron-positron pair. This e^+e^- pair itself creates further bremsstrahlung and so on, until the particles in this avalanche do not have sufficient energy to create further pairs of electrons and positrons.

Before the electro-magnetic particles reach the ECAL, they already pass approximately two radiation lengths of material, which mainly consists of the pressure vessel and the magnetic coil, even for angles $|\cos\theta| \sim 0$. Therefore the electro-magnetic shower already starts within insensitive material, before the remaining part of it can be detected in the lead glass blocks. Therefore, the intrinsic resolution of the ECAL is degraded by a factor of about $200\%/\sin\theta$. Especially measurements like that of the W mass in hadronic events, which relies on events with a wide angular spread of the particles, suffer from a degraded sensitivity of the calorimeters at angles between the barrel and the endcap part, where the entering particles pass a lot of insensitive material basically due to mechanical reasons. Barrel and endcap presampler detectors, located along the inside boundary of the electro-magnetic calorimeter, improve the position and energy resolution. The intrinsic resolution of the electro-magnetic calorimeter with its 22 radiation lengths is

$$\frac{\sigma_E}{E} \approx 0.2\% + \frac{6.3\%}{E/\text{GeV}} \quad [16]. \tag{3.7}$$

The Hadron Calorimeter

The return yoke for the magnetic flux from the magnet is used as the iron absorber of the hadron calorimeter (HCAL). The sensitive parts of this detector are streamer layers, interleaved with the iron absorber. They detect the hadronic and electro-magnetic showers produced in the iron absorbers.

With its depth of 4.8 nuclear interaction lengths it is capable to stop neutral and charged hadronic particles and measure their deposited energy. In addition it also supports the identification of muons.

Before particles reach the hadronic calorimeter which surrounds the ECAL, they pass already about two interaction lengths of material, mainly within the electro-magnetic calorimeter, thus the energy of hadrons is calculated combining ECAL and HCAL information. The energy resolution of the hadron calorimeter is about

$$\frac{\sigma_E}{E} \approx \frac{120\%}{\sqrt{E/\text{GeV}}} \quad [16]. \tag{3.8}$$

3.2.4 Muon Detectors

The only known particles that the calorimeters are not able to stop are muons and neutrinos. The latter escape the detection completely and can only be reconstructed imposing energy and momentum conservation. The muons on the other hand generally lead to signals in both the tracking system and the calorimeters, but due to their higher mass the energy loss via bremsstrahlung is negligible and they are not interacting via the strong force. Therefore, they escape the hadron calorimeter and enter the muon detectors, the outermost detector part of OPAL, which are supporting the identification of muons. With its drift chambers, covering in multiple layers both the barrel and the endcap part of

the detector, typical spatial resolutions of 1.5 mm in the $r - \phi$ plane and 2 mm in the z direction are achieved [16].

3.2.5 The Forward Detectors and Luminometers

The main purpose of the OPAL forward detectors and the silicon-tungsten luminometer is the observation of small angle Bhabha scattering processes in order to determine the LEP luminosity (see equation 3.1). At small angles to the beam, the t-channel, which has a $1/\theta^4$ dependency, dominates the differential $e^+e^- \to e^+e^-$ cross section.

The forward detector measures particles within angular the range from 47 to 120 mrad. It is divided into three parts, from inside to outside: The tube chambers, three layers of proportional counters located outside of the electro-magnetic presampler, measure the centre of gravity position of showers to within 3 mm. The following forward calorimeter consists of 35 sampling layers of a lead-scintillator sandwich, which measure the energy of the showers. The far forward detector, which is installed on either side of OPAL about 8 m from the interaction point, covers the region of $5 - 10$ mrad.

The silicon-tungsten luminometer, consisting of 19 layers of silicon microstrip detectors and 18 layers of tungsten on each side of the interaction point at $z \approx \pm 240$ cm, detects electro-magnetic showers from particles with angles between 25 and 59 mrad. It measures the position of the centre of gravity of electron showers with a precision of 220 μm and the energy with a resolution of $\sigma_E/E \approx 24\%/\sqrt{E/GeV}$ [17] in regions with minimal amount of material between the collision point and the luminometer.

3.2.6 Trigger and Data Acquisition

The first event selection and background rejection begins already on-line. Events, classified as signal, are selected and the total amount of information from all the subdetectors is already reduced in order to be able to be stored for later off-line analyses.

Trigger

With four electron on four positron bunches, there are about 45000 bunch crossings per second inside the OPAL detector. This rate is far to high to be read out by the experiment, not to mention the amount of data that would have to be stored. Therefore, the first selection of events is done already on-line with the trigger system of OPAL, reducing the number of recorded events to about 10 in a second. The trigger collects the fastest signals of the detector and compares them to predefined requirements in order to only read out "interesting events" and reject cosmic ray background and beam gas interactions. The trigger takes basically two different features into account: signals of individual subdetectors, like track and cluster multiplicities and energy sums, but also correlated angular properties in a grid of θ and ϕ from multiple detectors together.

Data Acquisition

An event, chosen to be recorded, still contains a lot of useless information, if all outputs of the various channels would be stored. Thus, the data acquisition system does not only collect the output from all the 16 subdetectors and already calibrate the data in a first step, it also compresses the event size, basically by considering only those channels that contain information above certain noise thresholds. This leads to a typical event size for a $W^+W^- \to q\bar{q}q\bar{q}$ event of 500 kbyte. Then the so-called filter compares each collected event's topology with various physics processes and rejects 15 to 35% of

events accepted by the trigger. Once the first calibration is made, the events become available for the different analyses. After having collected sufficient data – this typically takes about a week – another set of calibration constants increases the quality of the data.

3.2.7   Detector Simulation

In order to be able to compare the data taken with the detector to Monte Carlo simulated physics processes, the output of the various Monte Carlo generators is passed through the OPAL detector simulation GOPAL [19] (based on the GEANT package [20]) which attempts to produce a detector response, as if the events were taken with the real detector, as realistically as possible. The detector simulation takes into account the interaction of the particles with the material of the detector, the signal formation process in the different subsystems, as well as the behaviour of the trigger, the event builder and the filter [19].

Chapter 4

The Measurement of the Mass of the W Boson

This chapter describes the analysis tools and procedures for a W mass reconstruction in the hadronic channel for 183 pb^{-1} of data recorded with the OPAL detector in 1998 at the centre-of-mass energy $\sqrt{s} = 189$ GeV. First, the OPAL standard preselection for W$^+$W$^-$ candidates will briefly be described. Then the mass reconstruction, including kinematic corrections, will be introduced, focusing on the hadronic channel and finally the reweighting technique used in the analysis performed will be described and tests with events, simulated by Monte Carlo, will be performed. Furthermore, the influence of an inclusion of 5-jet events into the analysis will be discussed and optimised and a first attempt of an alternative two-dimensional analysis will be introduced.

4.1   Event Selection

In order to provide the analysis with an already relatively pure sample of $e^+e^- \to W^+W^- \to q\bar{q}q\bar{q}$ events, a selection takes place to reject most of those events that are obvious background. In the W pair analysis this is done in three steps: Starting with the most simple event signature, candidates for W$^+$W$^- \to \ell\nu\ell\nu$ events are selected and only events that fail this selection are considered as possible semi-leptonic or hadronic events. The second step selects W$^+$W$^- \to q\bar{q}\ell\nu$ events, while only events that fail both the leptonic and the semi-leptonic event selection enter the selection of hadronic events. For the event selection schemes for the leptonic and semi-leptonic channel the reader is referred to the references [21, 22] and [23, 24] where these two channels are fully described.

In the first stage of the selection of hadronic events from pairs of W bosons, the `DURHAM` jet algorithm combines tracks and calorimeter clusters to jets. After having corrected for double-counting of energy, the selection itself takes place.

4.1.1   Finding the jets

As one of the first steps of the mass reconstruction the tracks in the central tracking system of the detector together with the absorbed energies in the calorimeters have to be clustered in order to get four (five) jets that can be associated with the four quarks (and the energetic gluon) of hadronic W$^+$W$^-$ decays. This can be done with a variety of jet finding algorithms. All of these algorithms attempt to combine 4-momenta of tracks that are close to each other in order to end up with a reconstruction of the required number of jets, e.g. four or five.

Since the actual W mass analyses at OPAL [10, 25, 26] use the DURHAM jet finder [27], the same algorithm is used within these studies in order to allow a better comparison of the results.
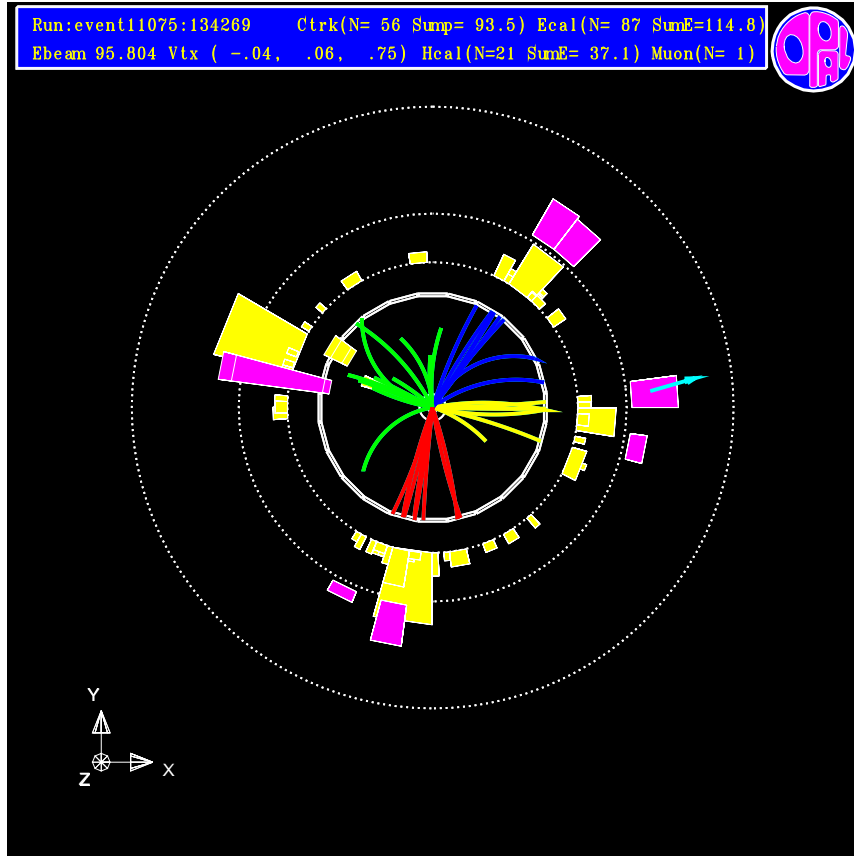
Figure 4.1: OPAL event display of a typical $W^+W^- \rightarrow q\overline{q}q\overline{q}$ candidate. The event is shown in direction of the beam axis. For a better illustration, the tracks recorded in the OPAL wire chamber have different colours which distinguish between the 4 jets found by the DURHAM jet finder (see section 4.1.1) using the detected tracks together with their associated entries in the OPAL calorimeters (yellow and magenta boxes for the electromagnetic and hadron calorimeter, respectively) and the muon system (light blue arrow).

Figure 4.1 shows a typical $W^+W^- \rightarrow q\overline{q}q\overline{q}$ candidate observed with the OPAL detector. The different colours of the tracks in the central chamber of OPAL illustrate the jet, each track belongs to with respect to the DURHAM jet finding algorithm. In the first step, this algorithm calculates for each pair i, j of detected particles (i.e. tracks and clusters) the quantity

$$\tilde{y}_{ij} = 2\frac{\min_{i,j}(E_i^2, E_j^2)}{s}(1 - \cos\theta_{ij}), \qquad (4.1)$$

where s is the centre-of-mass energy squared, $E_{i,j}$ are the energies of the i-th and the j-th particle and θ_{ij} denotes the angle between them. A small value of $\tilde{y}_{ij}$ means that the angle between the two particles is small or one of these two particles has low energy. Those two particles for which $\tilde{y}_{ij}$ is minimal are merged to a pseudo-particle by adding their 4-momenta. In the next step, $\tilde{y}_{ij}$ is calculated another time for all possible pairs of the remaining particles and the "new" pseudo-particle in order

to combine those two for which $\tilde{y}_{ij}$ is smallest. This procedure is iterated until the number of pseudo-particles[1] equals the required number of jets. These remaining pseudo-particles are then called jets, and in each step where the number of pseudo-particles is reduced from N to $N-1$,

$$y_{N-1,N} = \min_{i \neq j} \left[2 \frac{\min(E_i^2, E_j^2)}{s} (1 - \cos\theta_{ij}) \right] \tag{4.2}$$

is called the jet resolution parameter. The minimum is taken with respect to all combinations of two out of N jets. The jet resolution parameter $y_{N-1,N}$ is a measure for the smallest separation of two jets of a N-jet event. A small value of $y_{N-1,N}$ means that the event looks more like a $(N-1)$-jet rather than a N-jet event.

4.1.2 Jet Energy Correction

Information from the tracking detectors and the electro-magnetic and hadronic calorimeters contributes to the measurement of jet energies. In cases where charged tracks have associated clusters, corrections of order $10 - 15\%$ must be performed to eliminate double-counting of energy due to redundant measurements.

The algorithm used in this analysis identifies individual associations between tracks and clusters. The momentum of a particle is taken to be the momentum measured by the tracking system. The lower the momentum, the smaller is the considered matching region the track is pointing to. The contribution of each single track to the associated calorimeter cluster is subtracted from the energy measured by the electro-magnetic and the hadron calorimeter, using information from the particle identification to treat leptons and hadrons differently [28].

4.1.3 Monte Carlo Detector Recalibration

The detector response is included in the Monte Carlo simulation of events. The agreement between data and Monte Carlo simulation is very good, but due to miss-adjustment and aging effects there are small discrepancies. Therefore, the angular offsets, the angular resolutions of leptons and jets and the energy scale as a function of θ and ϕ of simulated events are corrected [29] using comparison of Monte Carlo to data for events recorded in 1998 at the centre-of-mass energy $\sqrt{s} \approx M_Z$, since the properties of the Z^0 boson are well understood from high precision measurements performed at LEP1.

4.1.4 $W^+W^- \rightarrow q\bar{q}q\bar{q}$ Event Selection

The selection of hadronic events from pairs of W bosons is fully documented in reference [30].

Preselection

First, a cut-based preselection suppresses poorly reconstructed events as well as a big fraction of the non-WW background – mainly from $Z^0 \rightarrow q\bar{q}(\gamma)$ events – by requiring the following properties of each candidate, reconstructed as a 4-jet event:

1. The effective invariant mass of the event, $\sqrt{s'}$ must exceed 75% of the available energy $\sqrt{s}$. $\sqrt{s'}$ is the energy that is left if the photon energy from initial state radiation is subtracted.

---

[1]For convenience, the term *pseudo-particles* also includes remaining particles that have not been merged to pseudo-particles yet.

2. The visible energy must be greater than $0.7 \cdot \sqrt{s}$.

3. The most energetic electro-magnetic cluster must contain less than $0.3 \cdot \sqrt{s}$.

4. The lowest (second lowest) multiplicity jet must contain at least one (two) charged particles.

5. The logarithm (base 10) of the largest weight W_{420}, calculated from the matrix element for the QCD background process $e^+e^- \rightarrow q\bar{q}q\bar{q}, \; q\bar{q}gg$ for all three jet combinations of a 4-jet event, must be less than zero. The momenta of the four jets are input in place of the parton momenta in order to calculate the probability density of a $e^+e^- \rightarrow Z^0$ event leading to this particular 4-parton arrangement. [31].

This preselection rejects 96% of the $Z^0 \rightarrow q\bar{q}$ background and has an efficiency of 93% so that a total of 2077 events in the data at $\sqrt{s} = 189$ GeV survive.

Likelihood Selection

After the preselection, a likelihood discriminant is calculated for each surviving candidate, evaluated with the following four variables:

1. $\max_{j.p.}[\log_{10}(W_{420})]$, the largest weight from the QCD matrix element of all three different jet combinations. Hadronic W^+W^- decays peak at lower value than the $q\bar{q}$ background.

2. $\max_{j.p.}[\log_{10}(W_{exe})]$, the maximal weight from the EXCALIBUR matrix element [32] for the CC03 process $W^+W^- \rightarrow q\bar{q}q\bar{q}$ of all three different jet permutations. In general, hadronic WW events have larger values of this event weight than the background processes.

3. $\log_{10}(y_{45})$, the logarithm of the jet resolution parameter from the DURHAM jet clustering algorithm (see section 4.1.1).

4. $S = 3/2 \min_{\vec{n}}(\sum p_t^2 / \sum \vec{p}^2)$, the sphericity of an event. Herein p_t is the transverse momentum with respect to the direction defined by $\vec{n}$ while the sum is performed over all particles. $q\bar{q}$ events tend to low values of S while the sphericity of $W^+W^- \rightarrow q\bar{q}q\bar{q}$ events is in general larger.

The relative likelihood discriminant for each event is taken from Monte Carlo simulated distributions of these four variables for both signal and background processes in a similar way as the likelihood selection described in section 4.4.3, by transforming these variables into uncorrelated (for the case of hadronic WW events) and Gaussian-like linear combinations of the original variables.

The selection of hadronic WW events provides an efficiency of 86.5% and a purity of 77% [10, 33].

4.2   Reconstruction of the Leptonic Events

A direct W mass reconstruction in the leptonic channel $W^+W^- \rightarrow \ell\nu\ell\nu$ is impossible because the two involved neutrinos are not detected and their momenta are not measurable.

However, it was shown that the distributions of certain variables are sensitive to the mass of the W boson. At OPAL two variables serve such a property: the lepton energies and the so-called pseudo-mass, a W mass that can be calculated under the assumption of completely planar events [21]. Figure 4.2 shows the OPAL event display of a typical $W^+W^- \rightarrow \mu^+\nu\mu^-\bar{\nu}$ candidate.
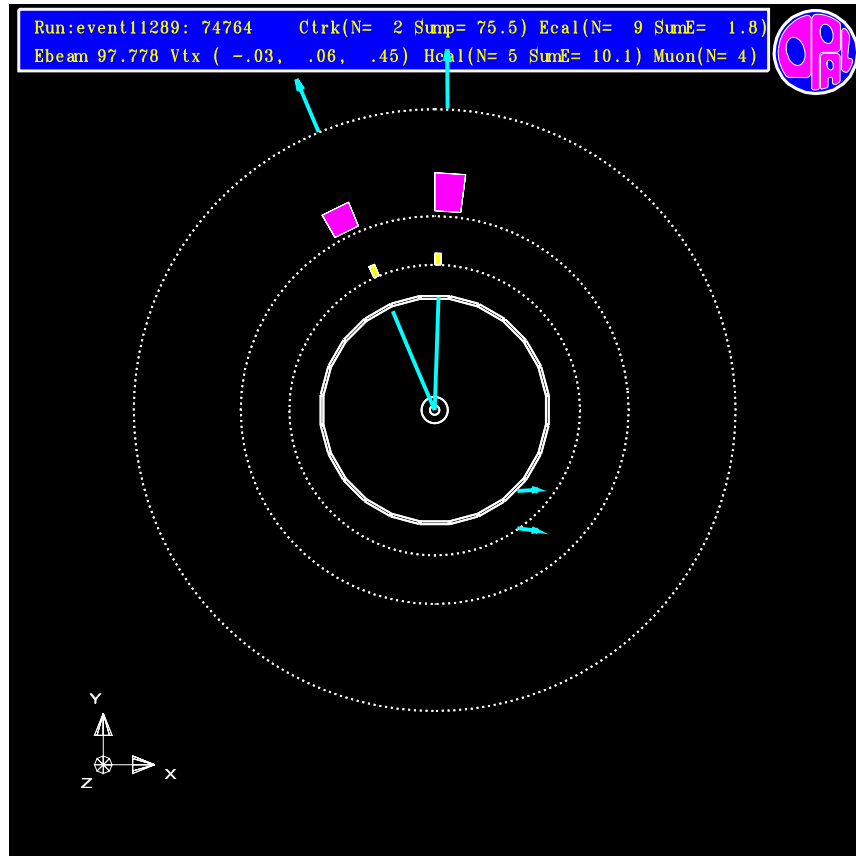
Figure 4.2: OPAL event display of a typical $W^+W^- \to \mu^+\nu\mu^-\bar{\nu}$ candidate. The event is shown in direction of the beam axis. From inside to outside, one can see the following signals: the tracks of the muons in the central tracking chamber (blue), little energy depositions in the electro-magnetic calorimeter (yellow), small entries in the hadronic calorimeter (magenta) and finally signals in the muon detectors (blue arrows).

4.3 Reconstruction of the Semi-Leptonic Events

First of all, after the primary lepton was identified, the hadronic jets have to be reconstructed. This is done by the DURHAM jet finder (see section 4.1.1), an algorithm which combines tracks and jets one after the other until the number of jets is reduced to the desired number of jets, i.e. two in the case of $W^+W^- \to q\bar{q}\ell\nu$ events.

In $W^+W^- \to q\bar{q}\ell\nu$ events, one already has the main mass information by evaluating the invariant mass of the two quark jets. The resolution can be improved by imposing constraints, i.e. momentum and energy conservation and the assumption that the two W masses are equal [23, 10]. Figure 4.3 shows a typical $W^+W^- \to q\bar{q}e\bar{\nu}$ candidate recorded with the OPAL detector.
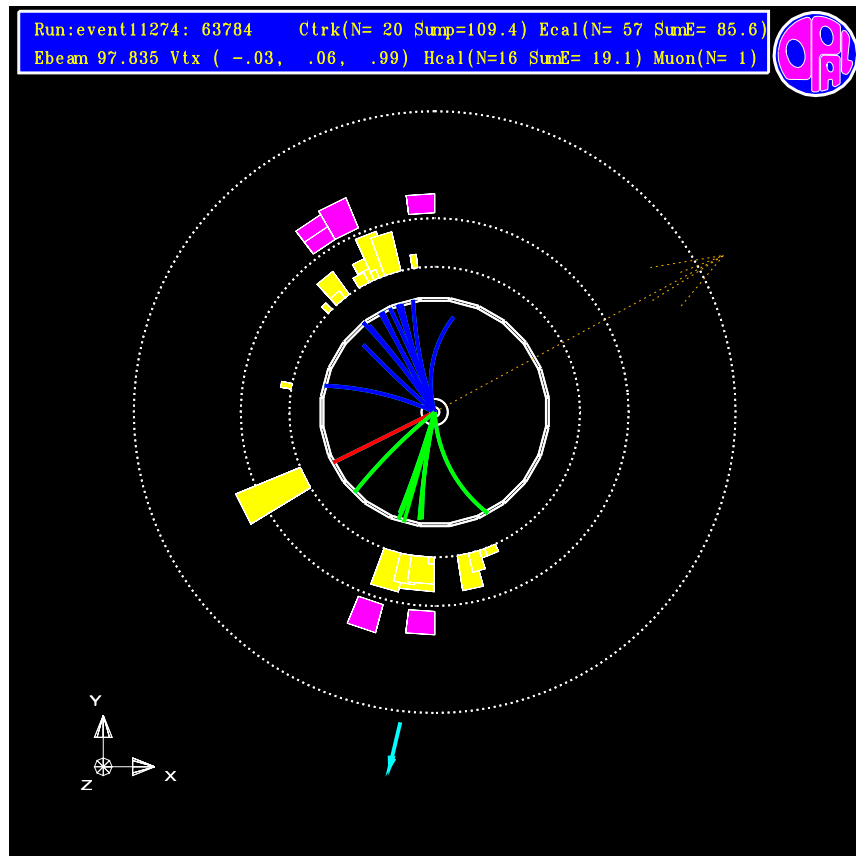
Figure 4.3: OPAL event display of a typical $W^+W^- \to q\bar{q}e\bar{\nu}$ candidate. The event is shown in direction of the beam axis. From inside to outside, one can see the following signals: the tracks of the muons in the central tracking chamber, entries in the ECAL (yellow), entries in the HCAL (magenta) and finally signals in the muon detectors (arrows). The big arrow denotes the direction of undetected momentum due to the neutrino. Clearly one can identify the isolated high energetic track from the electron (red) that was completely absorbed in the electro-magnetic calorimeter.

4.4 Reconstruction of the Hadronic Events

Figure 4.1 shows a $W^+W^- \to q\bar{q}q\bar{q}$ candidate recorded at OPAL. The four quarks of a hadronic WW event produce parton showers leading to four jets of hadrons, or—in the case of hard gluon radiation of a primary parton—to four quark jets and a gluon jet. The following paragraphs describe in more detail the different steps to reconstruct the momenta of the primary partons leading to a determination of the W mass for each hadronic event. Special emphasis is given to the different treatment of 4- and 5-jet like events.

4.4.1 Kinematic Corrections

The $W^+W^- \to q\bar{q}q\bar{q}$ channel does not have the disadvantage of undetected particles like in the other two WW channels. The mass reconstruction, however, is degraded from ambiguities due to multiple

jet combinations: There are three (ten) different ways to pair two out of four (five) jets and associate them with one of the two W bosons. The W mass reconstruction of each event therefore depends on the efficiency of finding the correct jet combination. If the correct jet pairing is found, the jet momenta can be corrected similarly to section 4.3 by imposing energy and momentum conservation as well as equal invariant mass of the two jet pairs. Because of the five constraints involved, this correction is called a 5-C fit. The following paragraphs describe the basic principles of such a correction and introduce the *fit probability* which is a function of the measure for the *goodness-of-fit* χ^2.

Given a set of measured variables $\{x_i\}$, $i = 1, 2, ..., N$ with uncorrelated uncertainties $\{\sigma_i\}$ and additional $n < N$ independent constraints

$$f_k(x_1, x_2, ..., x_N) = 0, \quad k = 1, 2, ..., n, \tag{4.3}$$

the fit tries to find the values $\{x_i'\}$ that minimise the function

$$\chi^2 = \sum_{i=1}^{N} \left(\frac{(x_i' - x_i)}{\sigma_i} \right)^2 + \sum_{k=1}^{n} \lambda_k f_k(x_1', x_2', ..., x_N'), \tag{4.4}$$

which is a fit with the Lagrangian multipliers λ_i. For a set of measured variables that are correlated, the expression changes to

$$\chi^2 = \sum_{i,j=1}^{N} (x_i' - x_i)(G^{-1})_{ij}(x_j' - x_j) + \sum_{k=1}^{n} \lambda_k f_k(x_1', x_2', ..., x_N'), \tag{4.5}$$

G being the covariance matrix of the measured variables $\{x_i\}$.

Assuming the errors and their correlations are correctly estimated, the minimal χ^2, divided by the number of degrees of freedom $N_{d.o.f.} = n$, is approximately 1. The χ^2-probability is given by

$$P(\chi^2; N_{d.o.f.}) = \frac{2^{-N_{d.o.f.}/2}}{\Gamma(N_{d.o.f.}/2)} \int_{\chi^2}^{\infty} \chi^{N_{d.o.f.}-2} \exp(-\chi^2/2) d\chi^2. \tag{4.6}$$

$P(\chi^2; N_{d.o.f.})$ describes the probability that a larger value of χ^2 than the one observed could occur. If the data obey the constraints and the errors are Gaussian and correctly estimated, this probability is a flat function between 0 and 1 (for further details see reference [34]).

For each of the three (ten) different combinations of a 4-jet (5-jet) event a 5-C fit is applied using energy and momentum conservation

$$f_k = \sum_{\text{jets } j} p_j^{(k)} - \delta_{k0}\sqrt{s} = 0, \quad k = 1, ..., 4, \tag{4.7}$$

as well as the equal mass constraint

$$f_5 = M_{W_1} - M_{W_2} = 0. \tag{4.8}$$

$p_j^{(k)}$ is the kth component of the 4-momentum $p_j^\mu = (p_j^{(0)} = E_j, \vec{p}_j)$ of the jth jet while M_{W_l} denotes the invariant mass of the lth W boson ($l = 1, 2$) for the combination chosen. If only the equations 4.7 are applied, it is referred to as a 4-C correction of the event. Such a 4-C fit is independent of a certain jet-W association.

For WW candidates, the assigned errors and correlations (the error matrix G) are estimated from Monte Carlo studies of $W^+W^- \to q\bar{q}q\bar{q}$ events and parameterised depending on the energies E_j, the

momenta $\vec{p}_j$ and the directions θ_j of the jets [35, 36]. Figures 4.4 a) and b) show the distributions of the 5-C fit probability for 4- and 5-jet events, respectively, with a cut on $p_{4,5}^{5\text{-C}} > 1\%$. These figures show good agreement between data and Monte Carlo. In principle, these distributions are supposed to be flat in case of well estimated errors. The large increase of entries for very small values of the fit probability originates from background. Also events with large deviations which get a small fit-probability, since the χ^2 is evaluated with Gaussian-like errors that do not take into account badly reconstructed events in the tails of the non-Gaussian distributions. For those events the errors on the measured quantities are underestimated.
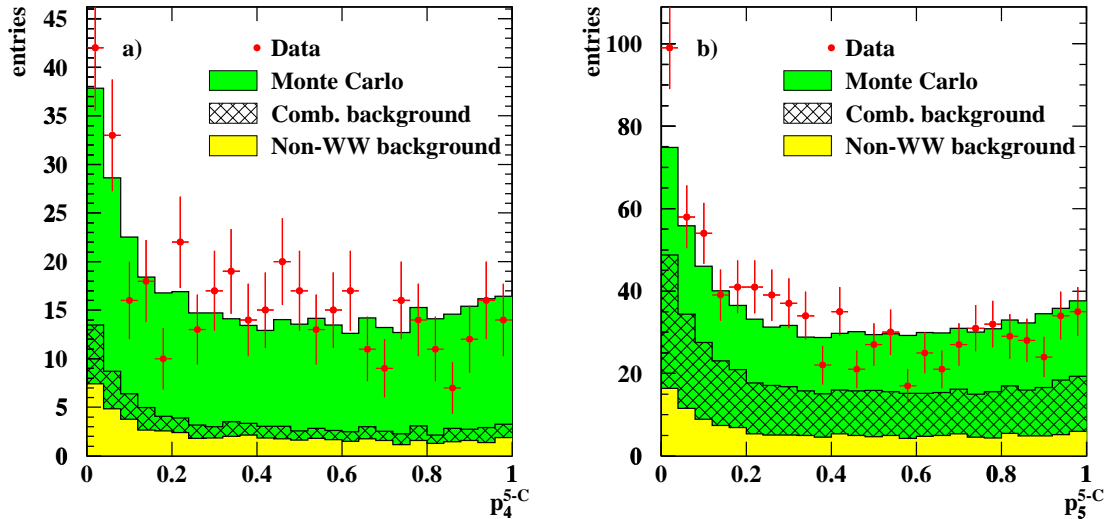
Figure 4.4: 5-C fit probability for a) 4- and b) 5-jet events with $p_{4,5}^{5\text{-C}} > 1\%$ and a 5-C fitted mass larger than 65 GeV. An event is treated as five jets if $\ln y_{45}$ exceeds -6.8. Otherwise, it is considered as a 4-jet event.

4.4.2   Five Jets versus four Jets

A kinematic fit (as described in 4.4.1) provides the probability that the four jets and their association to the two W bosons are consistent with energy and momentum conservation and the assumption of equal mass of the two W bosons. This probability is calculated for each jet pairing separately. Together with additional kinematic information it is used to determine, which combination is most likely the correct one (see section 4.4.3).

Even in the case of hard gluon radiation from one of the partons, the mass reconstruction of the event is correct if the jet finding algorithm (see section 4.1.1) associates the gluon jet to the correct parton. However, the 4-jet mass reconstruction can be biased or wrong if an initial parton radiates an energetic gluon and (part of) the momentum of the latter is not associated to the jet of the initial parton it originates from: Either the event is rejected due to a small probability to fulfil the constraints mentioned above, or it provides a non-optimal mass information and degrades the mass resolution of the analysis. Figure 4.5 shows a typical 5-jet candidate recorded with the OPAL detector. The tracks in the jet chamber are already coloured to label the jet they are associated to by the DURHAM jet algorithm.
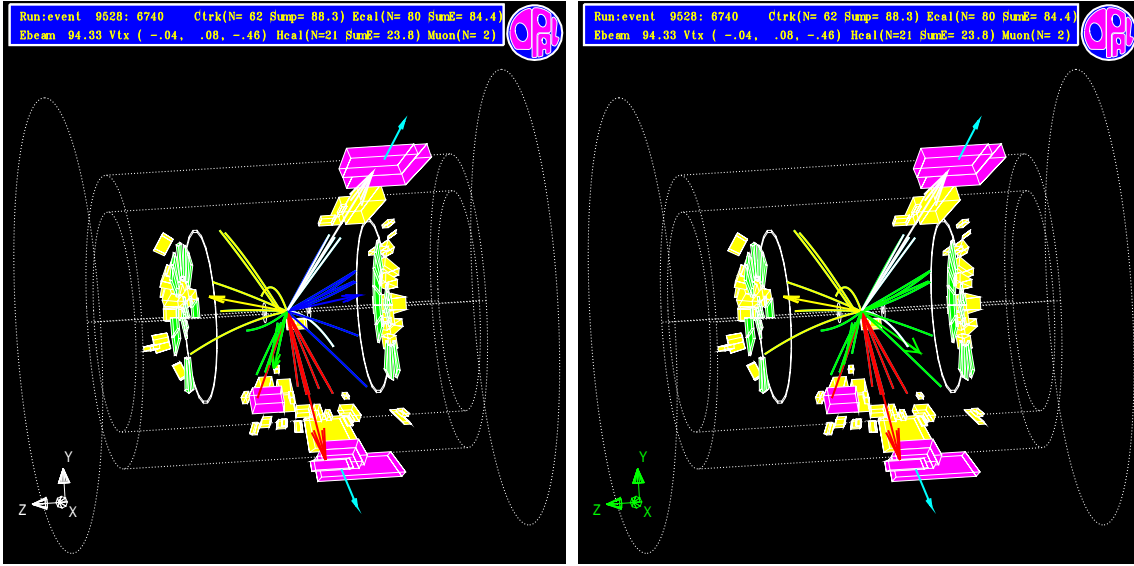
Figure 4.5: A 5-jet candidate recorded with the OPAL detector. This event, although it clearly looks like a 5-jet event ($\ln y_{45} = -4.20$) with a 5-C fitted mass of $M_W^{5j} = 79.43$ GeV, it also leads to a reasonable 4-jet reconstruction with $M_W^{4j} = 79.20$ GeV. The jet pairing likelihood is 0.78 and 0.65 for the 5- and 4-jet reconstruction (see section 4.4.3). Treated as 4 jets, the green and the red tracks, together with their associated calorimeter clusters, would be combined to a single jet.

A possible solution to the problem of wrongly associated energy is to treat the events as five jets rather than four jets in order to avoid that the jet algorithm adds gluon energy to a wrong jet. The idea is to recover otherwise rejected 4-jet events on the one side and improve the mass reconstruction of events with a hard gluon on the other side. As an example for an event that might be recovered in a 5-jet treatment, figure 4.6 shows the event display of a 5-jet candidate where a 4-jet reconstruction fails by means of a low fit probability $p_{4j}^{5\text{-}C} = 0.08$. Reconstructed as a 5-jet event, the fit probability becomes $p_{5j}^{5\text{-}C} = 0.38$ [2]. The corresponding reconstructed masses are 72.15 GeV for four and 79.61 GeV for five jets.

The disadvantage of treating WW events as five jets comes from the larger number of possibilities of jet combinations: There are ten different ways of associating two jets out of five to one W. This can in general lead to a bigger combinatorial background, i.e. $W^+W^- \to q\bar{q}q\bar{q}(g)$ events that provide no

---

[2]Note that the probabilities for a 4- and a 5-jet 5-C fit cannot easily be compared in a quantitative way, since the number of free parameters is bigger in the case of 5 jets. Therefore, the corresponding fit probability is anyhow likely to tend to higher values. Using a likelihood discriminant in order to find the correct jet combination as will be described in 4.4.3, this event, reconstructed as four jets, gets a likelihood value of 0.01 and would be rejected. As five jets, the jet pairing likelihood becomes 0.83.

Figure 4.6: Another 5-jet candidate recorded with the OPAL detector ($\ln y_{45} = -3.70$), reconstructed as five (left) and as four jets (right). This event gives significantly different results when treated as four jets: The measured W masses are $M_W^{5j} = 79.61$ GeV and $M_W^{4j} = 72.15$ GeV. The values for the jet pairing likelihood (see section 4.4.3) are 0.83 and 0.01 for the case of five and four jets, respectively. This event would probably be rejected in a pure 4-jet analysis.

useful mass information due to a wrong jet-W association. Also a loss of signal events for which the 4-jet analysis would have picked the right combination has to be considered.

The path this analysis wants to follow is to improve the existing 4-jet analysis by dividing all events into two groups with respect to the jet resolution parameter y_{45} (given by equation (4.2)) and treat them separately.

In order to quantify the effect of mixing the energy from both W bosons in one jet, one can use the incorrectly associated W energy E_{wrong} to each of the four or five jets known from Monte Carlo simulated events. The fraction of the jet energy that originates from a certain one of the two W bosons can be obtained by applying a jet finding algorithm at the parton level of the event simulation. The parton jets for which the association to the two W bosons is known can then be associated to the jets on detector level using angular matching.

The left part of figure 4.7 shows the fraction of 4-jet (5-jet) events in bins of $\ln y_{45}$ that have at least one jet for which the wrongly associated energy E_{wrong}^{max} exceeds 10 GeV. For a small value of $\ln y_{45}$, E_{wrong}^{max} is similar for 4 and 5 jet events but with increasing $\ln y_{45}$ it becomes much worse for 4 jet events. This indicates that an improvement by 5 jet reconstruction can mainly be expected for events with a large $\ln y_{45}$.

The effect is further illustrated in the right side of figure 4.7 by the distribution of the wrongly associated W energy E_{wrong}^{max} for the "worst" jet for both four and five jets just for those events with $\ln y_{45}$ exceeding -6.8. This distribution shows that it is worth trying to recover 4-jet events in the high-y_{45} region with a high amount of wrongly associated W energy by treating them as five jets.
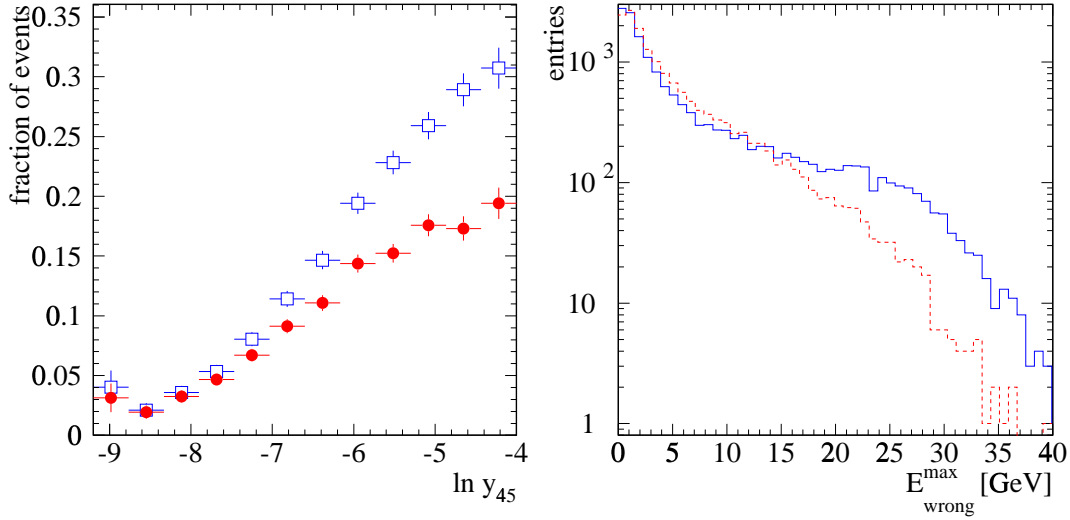
Figure 4.7: The left side shows the fraction of events with wrongly associated energy that is bigger than 10 GeV for each bin in $\ln y_{45}$ for 4-jet (empty squares and solid bars) and 5-jet events (filled circles and dashed bars). The right side shows the distribution of the wrongly associated energy E_{wrong}^{max} for the "worst" jet for 4-jet (solid line) and 5-jet events (dashed line) with $\ln y_{45} > -6.8$.

4.4.3 The Correct Jet Combination

The best jet pairing, i.e. the jet combination that is most likely the correct one, is found for both 4- and 5-jet events with a relative likelihood discriminant [25].

This selection is based on the so-called *principal component* (PC) technique. For each jet combination a relative likelihood

$$\mathcal{L} = \frac{\mathcal{L}^{(\text{correct comb.})}}{\mathcal{L}^{(\text{incorrect comb.})} + \mathcal{L}^{(\text{correct comb.})}} \tag{4.9}$$

is evaluated, where the likelihood function $\mathcal{L}^{(\cdots)}$ is defined by

$$\mathcal{L}^{(\cdots)} = \prod_i p_i^{(\cdots)}(x_i). \tag{4.10}$$

$p_i^{(\cdots)}(x_i)$ is the probability density function (pdf) of the i-th linearly independent variable at the value x_i for being either a correct or incorrect jet combination.

The pdfs are taken from Monte Carlo simulated distributions of the variables. Since they are generally correlated, a transformation is applied in order to get uncorrelated variables for the correct jet combinations—not necessarily for the combinatorial background—before they enter equation 4.10: First each single variable is transformed separately to become Gaussian-like, finally a set of linearly independent combinations of these variables is found.

This likelihood selection associates to each of the different jet combinations a likelihood value, evaluated with the distributions of a set of kinematic variables for both correct and incorrect combinations. These distributions are taken from events simulated by Monte Carlo where the correct jet-W association is known.

The variables that are used to determine the correct jet pairing in the case of a 4-jet event are the following [10, 25, 33]:

- the difference $|\Delta M_W^{4\text{-C}}| = |M_{W_1}^{4\text{-C}} - M_{W_2}^{4\text{-C}}|$ of the two W masses after a 4-C fit, applying only energy and momentum conservation, and

- the sum of the two di-jet opening angles $\theta_{ij} + \theta_{lk}$.

The distributions of these variables for both correct and incorrect jet pairings are shown in the figures 4.8 and 4.9. Those 4-jet combinations that have a 5-C fit probability $p_{4j}^{5\text{-C}}$ exceeding 1% and provide a 5-C corrected W mass $M_W^{5\text{-C}}$ larger than 65 GeV enter these distributions. For each event, there are two possible contributions of combinatorial background. However, there are more correct than incorrect jet combinations shown in these figures which reflects the fact, that already most of the wrong combinations fail the cuts described above.

Taking the jet combination that maximises the JPLH leads to a jet pairing efficiency of 91% for those events with a jet resolution parameter $\ln y_{45}$ smaller than -6.8 [3] and with at least one combination with JPLH > 0.4.
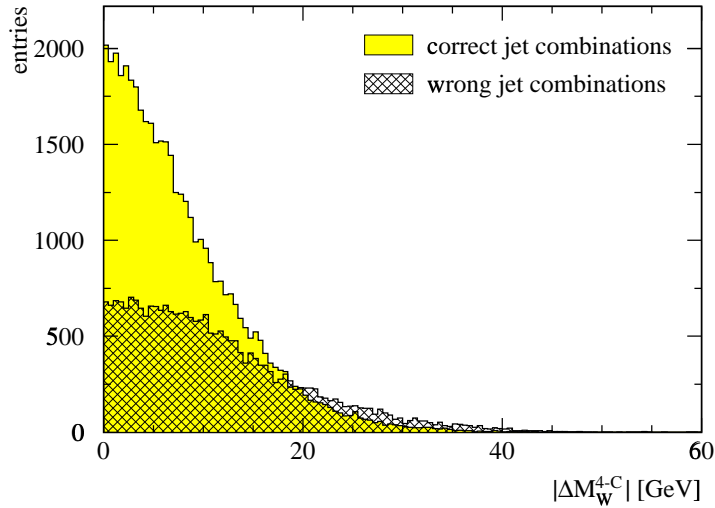
Figure 4.8: Distribution of the difference of the 4-C corrected W masses for both the correct and incorrect jet pairings. Only 4-jet combinations with a 5-C fit probability $p_{4j}^{5\text{-C}}$ exceeding 1% and a 5-C corrected W mass $M_W^{5\text{-C}}$ larger than 65 GeV are taken into account.

For 5-jet events the following three variables are chosen:

- the difference between the two fitted masses from the 4-C fit $|\Delta M_W^{4\text{-C}}| = |M_{W_1}^{4\text{-C}} - M_{W_2}^{4\text{-C}}|$,

- the minimum opening angle $\min\limits_{3\text{-jet W}} (\alpha)$ between the jets associated to the system $W \rightarrow q\bar{q}g$ and

- the cosine of the polar angle of the reconstructed 3-jet system $|\cos\theta_{3j}|$.

The figures 4.10 to 4.12 show the distributions of these three variables for both the correct jet pairing and the combinatorial background only for those combinations that have a 5-C fit probability exceeding 1% and a 5-C corrected mass above 65 GeV. For each event, there are approximately two out of

---

[3]The fact that a value of $(\ln y_{45})_{\text{cut}} = -6.8$ is chosen to distinguish between 4- and 5-jet events looks arbitrary in this section. This particular value is chosen because it minimises the expected error on the mass determination, as will be shown in section 4.6.

Figure 4.9: Distribution of the sum of the two di-jet opening angles $\theta_{ij} + \theta_{kl}$ for both the correct and incorrect jet pairing. Only 4-jet combinations with a 5-C fit probability $p_{4j}^{5\text{-C}}$ exceeding 1% and a 5-C corrected W mass $M_W^{5\text{-C}}$ larger than 65 GeV enter the distributions.

nine possible incorrect jet combinations that pass the cuts and therefore enter the distributions for the combinatoric background in these figures.
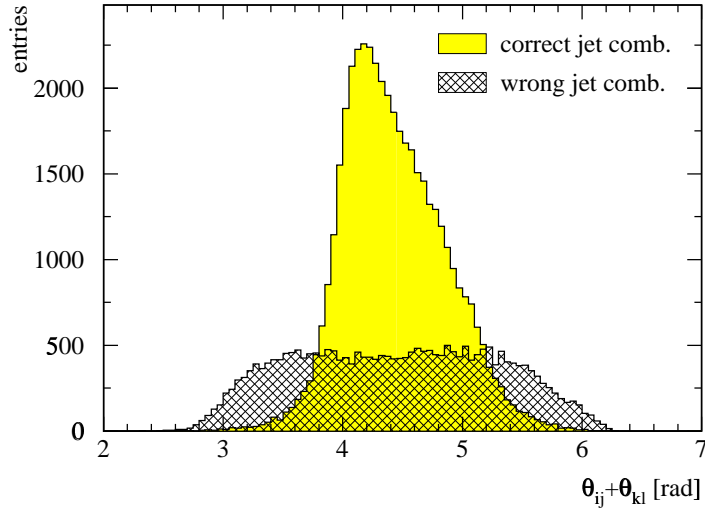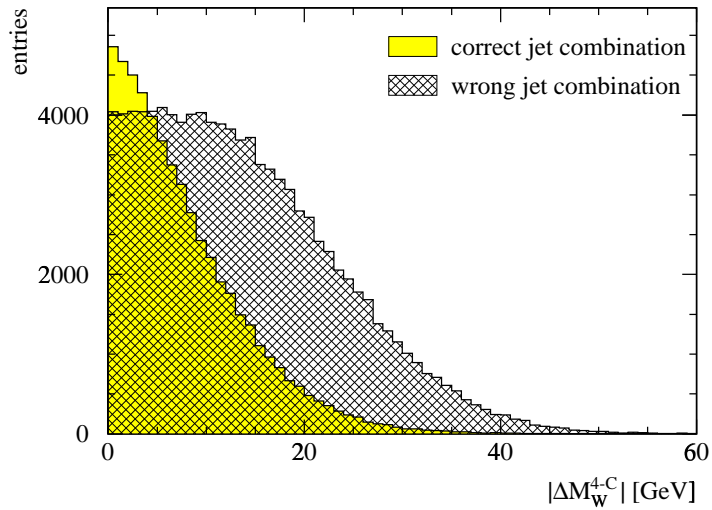

Figure 4.10: Distribution of the difference of the 4-C corrected W masses for both the correct and incorrect jet pairing. Only 5-jet combinations with a 5-C fit probability $p_{5j}^{5\text{-C}}$ exceeding 1% and a 5-C corrected W mass $M_W^{5\text{-C}}$ larger than 65 GeV and smaller than 95 GeV are taken into account.

In former OPAL analyses [10, 33] an additional variable was taken for 5 jet events: The 5-C fitted mass $M_W^{5\text{-C}}$ itself was entering the jet pairing likelihood (JPLH). This variable, being very sensitive to the correct jet pairing (see figure 4.13), enhances the efficiency of the jet pairing from 59% to 74%
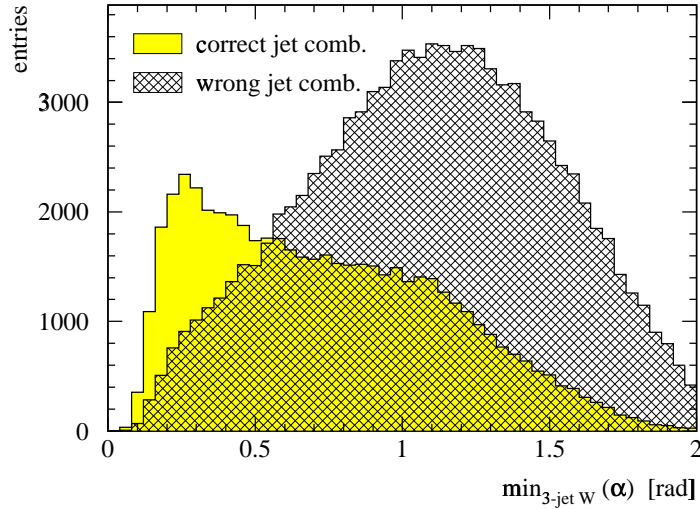
Figure 4.11: Distribution of the smallest opening angle of the 3-jet system for both the correct and incorrect jet pairing. Only 5-jet combinations with a 5-C fit probability $p_{5j}^{5\text{-}C}$ exceeding 1% and a 5-C corrected W mass $M_W^{5\text{-}C}$ larger than 65 GeV contribute to the distributions.
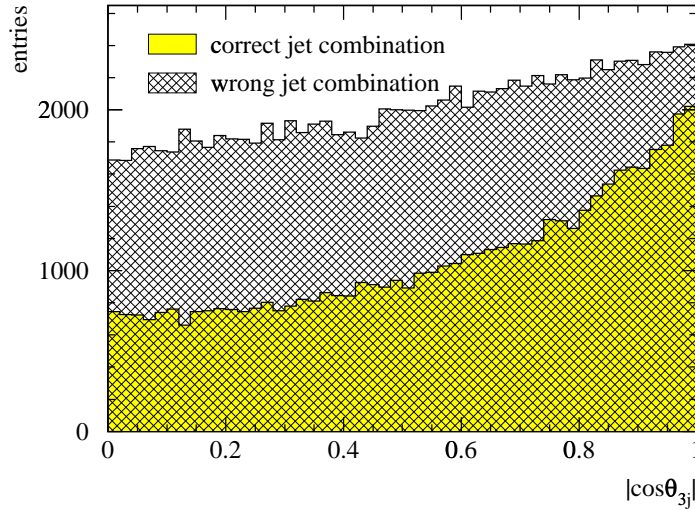
Figure 4.12: Distribution of the cosine of the angle between the 3-jet W and the beam pipe $|\cos\theta_{3j}|$ for both the correct and incorrect jet pairing. Only 5-jet combinations with a 5-C fit probability $p_{5j}^{5\text{-}C}$ exceeding 1% and a 5-C corrected W mass $M_W^{5\text{-}C}$ larger than 65 GeV are considered.

for jets with a jet resolution parameter $\ln y_{45}$ exceeding -6.8. This efficiency is the fraction of events for which the 5-jet JPLH was maximal for the correct combination with respect to all events that have at least one jet combination with a JPLH exceeding 0.42. Jet combinations with 5-C fit probabilities smaller than 1% or 5-C fitted masses smaller than 65 GeV are not taken into account.

Of course, a better jet pairing efficiency leads to a better resolution, since there is not much mass
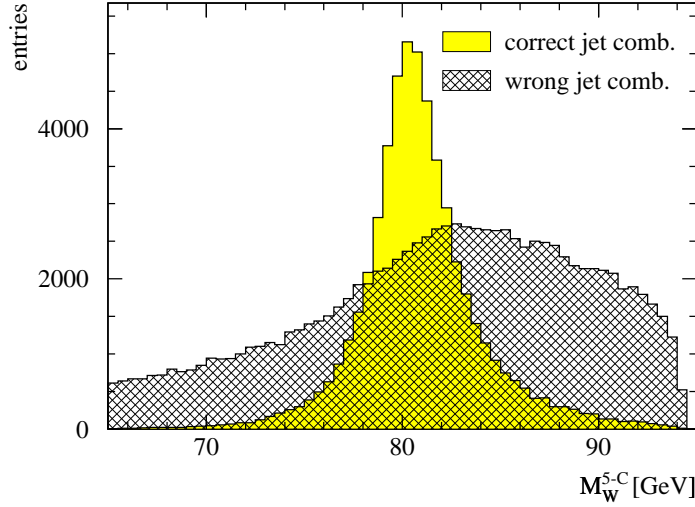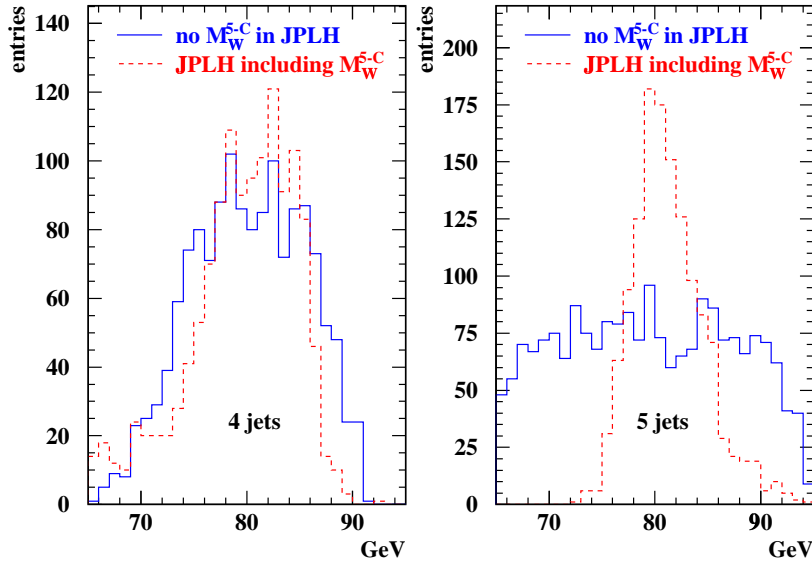
Figure 4.13: Distribution of the 5-C fitted W mass of 5-jet events for both the correct and incorrect jet pairing. Only 5-jet combinations with a 5-C fit probability $p_{5j}^{5\text{-C}}$ exceeding 1% and a 5-C corrected W mass $M_W^{5\text{-C}}$ larger than 65 GeV enter the distributions. For reasons, explained in section 4.4.3, the variable $M_W^{5\text{-C}}$ is not used for the JPLH in order to find the correct jet-W association.

information in combinatorial background, i.e. those events for which a wrong combination maximises the JPLH. On the other hand, the distributions taken to evaluate the JPLH come from Monte Carlo simulated data for a W mass of 80.33 GeV. Therefore, those jet combinations, that have a 5-C fitted mass close to 80.33 GeV are favoured. Since this analysis uses a reweighting technique (see 4.5.1), this does not lead to a bias (also the reweighted distributions, to which the data are compared, are slightly shifted towards the W mass, for which the reference distributions in the JPLH were simulated, i.e. $M_W^{MC} = 80.33$ GeV), but the sensitivity of the measurement decreases.

This effect is illustrated in figure 4.14 where the 5-C fitted mass distributions of the $q\bar{q}$ background are shown for both jet pairing methods, with and without the 5-C fitted mass as an input variable for the JPLH. One can clearly see that this distribution does not show a maximum at 80.33 GeV in the latter case for 5-jet events. The flatness of the distribution taken without the 5-C mass in the JPLH indicates the independency of the remaining variables from the W mass itself. For 4-jet events however, the distribution does not change as dramatically when taking the 5-C fitted mass into account. The jet pairing is already quite efficient, even without this additional variable in the jet pairing likelihood. Furthermore, the opening angle of the jets of each W boson is sensitive to the velocity of the W boson itself. This velocity is determined by the kinematic energy $E_{kin} = 1/2\sqrt{s} - M_W$ which depends on the W mass.

The diagrams in figure 4.15 demonstrate the effect of the jet pairing being sensitive to the W mass on the mass distributions themselves. The left diagram shows the mass distribution $M_W^{rec.} - M_W^{MC}$ of the selected 5-jet combinations ($\ln y_{45} > -6.8$) for different Monte Carlo masses M_W^{MC} without the contribution from combinatoric and non-WW background. If the jet pairing would not be correlated with the Monte Carlo mass, for which the pdfs in the JPLH are produced, these distributions—and therefore their mean values—are expected to be identical. The mean values of the distributions are indicated by the vertical lines. Distributions for MC masses smaller than the mass M_W^{JPLH}, for which the reference distributions of the jet pairing likelihood were obtained, are shifted to higher masses.

Figure 4.14: 5-C fitted mass distribution of 4-jet (left) and 5-jet (right) events of the $q\bar{q}$ background for different jet pairing likelihoods: with (dashed line) and without (solid line) the mass $M_W^{5\text{-C}}$ being additional variable in the JPLH. The left figure contains events, reconstructed as 4 jets, with a jet resolution parameter $\ln y_{45}$ smaller than -6.8, while the right side shows 5-jet events with $\ln y_{45}$ exceeding -6.8.

Distributions for higher masses tend to lower values. The right diagram of figure 4.15 shows the mean values of the mass distributions versus the Monte Carlo mass $M_W^{MC} - 80.33$ GeV. Ideally, one would expect a constant function. However, the mean of a mass distribution for selected correct jet combinations of a MC sample with $|M_W^{MC} - M_W^{JPLH}| = 500$ MeV is shifted only by 354 ± 15 MeV, as the linear fit indicates. This effect results in a decrease of the sensitivity of the mass measurement. The mean of the mass distribution is certainly not the ideal measure in order to quantify the decrease of sensitivity in a reweighting analysis. A measurement of M_W aided by reweighting techniques is sensitive to the whole shape of the mass distributions. Furthermore, combinatoric and non-WW background was not taken into account.

The initial idea was to drop the 5-C corrected W mass as a variable for the JPLH and replace it by other kinematic variables that are less correlated with the mass itself but still sensitive to the correct jet combination in order to gain a similar jet pairing efficiency as before. This attempt is described in appendix A. Unfortunately there are no additional variables found that are both, sensitive to the correct jet combination and uncorrelated with the 5-C mass. Therefore, $M_W^{5\text{-C}}$ is taken out of the JPLH for 5-jet events but the second best jet pairing is considered as well if its 5-C fit probability exceeds $1/2$ of the fit probability of the jet combination that maximises the JPLH. This basically ensures, that the correct jet pairing is taken into account, and the wrong combinations lead to a flat combinatorial background. The jet pairing efficiency for the best jet combination is only 59% for 5 jet events, but including also the second best jet pairing yields 68% in total.
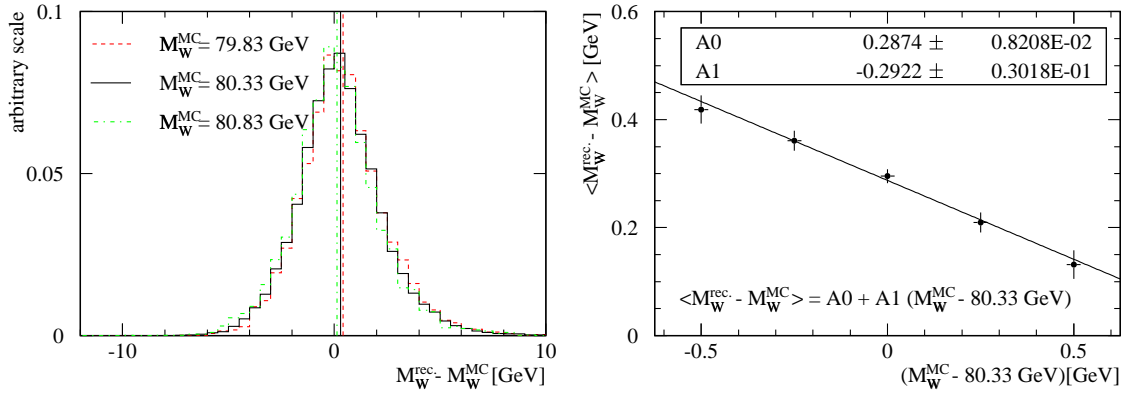
Figure 4.15: Influence of the W mass as an additional variable in the jet pairing likelihood: The left diagram shows the 5-C fitted mass distributions for selected 5-jet combinations (combinatoric and non-WW background is not included) for different Monte Carlo masses M_W^{MC}. The right diagram shows the mean values of these distributions versus the Monte Carlo mass as well as a line fit through the points.

4.5 The W Mass fit in the $W^+W^- \to q\overline{q}q\overline{q}$ Channel

Probably the simplest way to measure the mass of the W boson by evaluating the average of the 5-C fitted masses of all selected candidates and correct the result for background and biases. A more sophisticated method uses an asymmetric Breit-Wigner fit to the spectrum of all 5-C corrected masses [10, 37]. Such an analysis yields smaller statistical errors but the result needs to be bias corrected as well. It turns out, however, that using a reweighting technique [38] improves the error on the measurement [10] and is—as will be be discussed—by construction bias free.

The purpose of this section is to describe the way the W mass is evaluated from the sample of data detected at OPAL in 1998. It introduces the reweighting technique and explains the several steps taken to calculate the mass and its statistical error.

4.5.1 The Reweighting Technique

As well as a Breit-Wigner fit, the reweighting method uses the whole distribution of calculated masses rather than just an average value. The basic idea is to compare this distribution to Monte Carlo (MC) simulated distributions for different masses M_W^{MC} including background distributions. This can be done by evaluating the likelihood distribution, based on Poisson probabilities for the data sample in each bin of the mass distribution, for each mass point M_W^{MC}. The W mass together with its error are then obtained from the shape of the likelihood contour. Provided the simulated distributions come from correctly simulated Monte Carlo events, the result does not have to undergo a bias correction since the steps from the event sample to the distributions are the same for both the real data and the simulated distributions the data is compared to.

Unfortunately, it would be too much effort and it would cost too much computer and data storage capacity to produce enough statistics of Monte Carlo events for each different mass point of a sufficiently thin grid. Therefore, this analysis uses a reweighting technique [38] to create mass distributions for arbitrary masses from given samples of MC events to evaluate the likelihood function at any given mass point different from Monte-Carlo masses.

In order to create a mass distribution for a required mass $M_W = M_W^{Rew.}$ and width $\Gamma_W = \Gamma_W^{Rew.}$, the

reweighting technique fills all events of a given MC sample at $M_W = M_W^{MC}$ and $\Gamma_W = \Gamma_W^{MC}$ into a histogram, but with a weight f associated to each event. This factor f, which depends on $M_W^{Rew.}, \Gamma_W^{Rew.}, M_W^{MC}$ and Γ_W^{MC}, is the probability[4] that the generated event corresponds to $(M_W^{Rew.}, \Gamma_W^{Rew.})$, divided by the probability that the same event arose from $(M_W^{MC}, \Gamma_W^{MC})$. These probabilities $P(M_W, \Gamma_W, m_1, m_2)$ are proportional to the product of the relativistic Breit-Wigner distributions for the two W bosons:

$$P(M_W, \Gamma_W, m_1, m_2) = \mathfrak{BW}(M_W, \Gamma_W, m_1) \times \mathfrak{BW}(M_W, \Gamma_W, m_2) \times c(m_1, m_2, \sqrt{s}). \tag{4.11}$$

Herein m_1 and m_2 denote the two W masses of the event on tree-level and c is a phase space factor depending only on m_1, m_2 and the centre-of-mass energy $\sqrt{s}$. The relativistic Breit-Wigner function $\mathfrak{BW}$ is given by

$$\mathfrak{BW}(M_W, \Gamma_W, m) = \frac{1}{\pi} \frac{\frac{m^2}{M_W}\Gamma_W}{(m^2 - M_W^2)^2 + \frac{m^4}{M_W^2}\Gamma_W^2}. \tag{4.12}$$

The reweighting factor for a generated event with the tree-level masses m_1 and m_2 then becomes

$$f = \frac{\mathfrak{BW}(M_W^{Rew.}, \Gamma_W^{Rew.}, m_1) \times \mathfrak{BW}(M_W^{Rew.}, \Gamma_W^{Rew.}, m_2)}{\mathfrak{BW}(M_W^{MC}, \Gamma_W^{MC}, m_1) \times \mathfrak{BW}(M_W^{MC}, \Gamma_W^{MC}, m_2)}. \tag{4.13}$$

Figure 4.16 shows the function f of equation (4.13) for the case where MC data, that is available for $M_W^{MC} = 80.0$ GeV and $\Gamma_W^{MC} = 1.9$ GeV, has to be extrapolated for a distribution with $M_W^{Rew.} = 80.5$ GeV and $\Gamma_W^{Rew.} = 2.0$ GeV.

However, since the statistic in the Monte Carlo sample is limited, large fluctuations in the reweighted spectra arise from events with tree-level masses in the vicinity of $M_W^{Rew.}$, especially when the difference between M_W^{MC} and $M_W^{Rew.}$ is large. These events can gain enormously big weighting factors (4.13). The quality of the reweighted spectra can be improved by including Monte Carlo samples at different masses M_W^{MC} into one reweighted spectrum by taking the weighted average bin-by-bin, such that the content of the jth bin of the reweighted spectrum from MC sample k is given by

$$r_j^{(k)} = \frac{1}{N^{(k)}} \sum_{i=1}^{n_j^{(k)}} f_i^{(k)} \tag{4.14}$$

where the sum is taken over all $n_j^{(k)}$ events in bin j of the kth MC sample and $f_i^{(k)}$ is the weighting factor for each of those events. $N^{(k)}$ is a normalisation factor and determined by

$$N^{(k)} = \sum_j r_j^{(k)} \tag{4.15}$$

in order to normalise all the reweighted distributions of the different MC masses to unity before combining them.

The error on $r_j^{(k)}$ is given by

$$\Delta r_j^{(k)} = \frac{1}{N^{(k)}} \sqrt{\Delta(\bar{r}^{(k)})^2 + \sum_{i=1}^{n_j^{(k)}} f_i^{(k)2}}. \tag{4.16}$$

---

[4]Since it is *fact* that the considered event comes from a sample of MC events for given $(M_W^{MC}, \Gamma_W^{MC})$ and *not* from $(M_W^{Rew.}, \Gamma_W^{Rew.})$, the term *probability* can be rather misleading. More precisely, those probabilities are the probability densities that an event with the same tree-level masses M_{W_1} and M_{W_2} could have been produced with a MC generator for given mass and width.
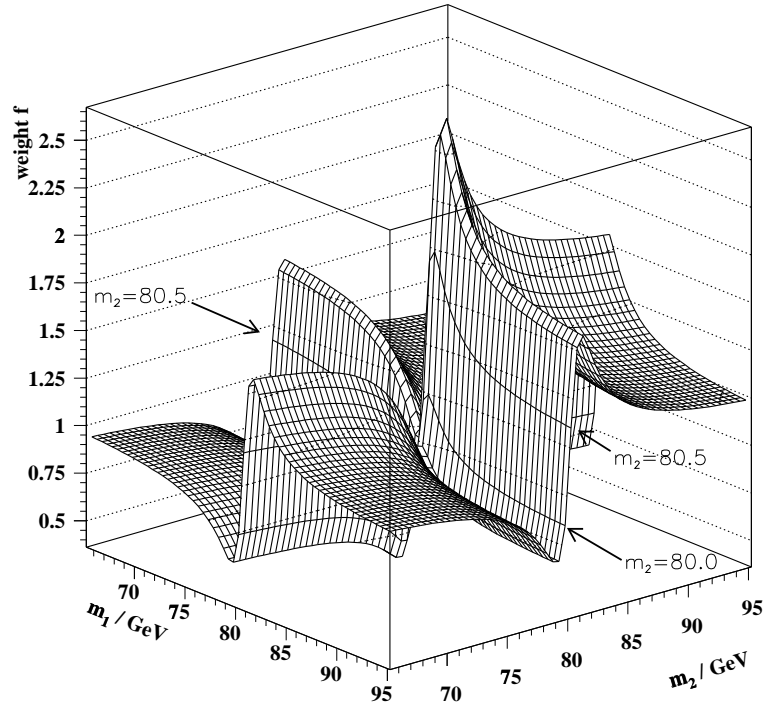
Figure 4.16: Weight f of events with the tree-level masses m_1 and m_2 for Monte Carlo events, produced for $M_W^{MC} = 80.0$ GeV and $\Gamma_W^{MC} = 1.9$ GeV, that have to be extrapolated to $M_W^{Rew.} = 80.5$ GeV and $\Gamma_W^{Rew.} = 2.0$.

The average error $\Delta(\bar{r}^{(k)})$ is added to ensure a meaningful inclusion of bins with low statistics. It is defined as

$$\Delta(\bar{r}^{(k)}) = \frac{1}{N_{bins}} \sqrt{\sum_{j=1}^{N_{bins}} \sum_{i=1}^{n_j^{(k)}} f_i^{(k)}}. \tag{4.17}$$

For bins with high statistics - e.g. around the mass peak - this term can be neglected, but without it, the error (4.16) could become very low (or even zero) for bins with just few (or no) events. Since the error determines the weights, as will be shown, the weights would become to high. A discussion of the errors can be found in [38]. The combined content of bin number j is the weighted sum over the N_{MC} available Monte Carlo samples

$$r_j = \frac{\sum_{k=1}^{N_{MC}} \frac{r_j^{(k)}}{\Delta r_j^{(k)}}}{\sum_{k=1}^{N_{MC}} \frac{1}{\Delta r_j^{(k)}}}. \tag{4.18}$$

The weight ensures that MC samples with a mass $M_{MC}^{(k)}$ closer to $M_{MC}^{Rew.}$ have greater impact than samples that are further away.

In the presented analysis, reweighted Monte Carlo spectra of the 5-C corrected mass are produced for $M_W^{Rew.}$ between 79.33 and 81.33 GeV with a step size of $\Delta M_W^{Rew.} = 50$ MeV [5]. The width in equation (4.13) is set to the Standard Model expectation value (see equation 2.29).

Then the mass spectrum for the expected non-WW background, i.e. $e^+e^- \rightarrow \gamma/Z \rightarrow q\bar{q}(\gamma)$ and $e^+e^- \rightarrow ZZ \rightarrow q\bar{q}q\bar{q}$ events, is created from Monte Carlo simulations and added, to each of the reweighted spectra, such that the ratio of WW to non-WW contributions equals the SM expectation.

For each of the mass points, the data sample's distribution is compared to the corresponding reweighted spectrum (including background) by calculating the binned likelihood function

$$\mathscr{L} = \prod_j \frac{\lambda_j^{n_j} e^{-\lambda_j}}{n_j!},$$
(4.19)

which is the product of the Poisson probabilities of each bin j for an expected content of λ_j, while n_j is the number of data events found in bin j. The central limit theorem [34] tells that for large numbers of events the shape of the likelihood function is a Gaussian[6], with the maximum being the measured quantity M_W^{fit} and the width determining its error $\Delta M_W^{fit} = \sigma_\mathscr{L}$. In practice, the evaluation of (4.19) is done by examining the function

$$\begin{aligned}
-\ln\mathscr{L} &= -\sum_j \ln \frac{\lambda_j^{n_j} e^{-\lambda_j}}{n_j!} \\
&= -\sum_j n_j \ln\lambda_j + \sum_j \lambda_j + \sum_j \sum_{i=1}^{j} \ln n_i
\end{aligned}$$
(4.20)

where the second and third term in the second line are constants and therefore can be neglected: the second term is the integral over the reweighted spectrum and the third term only depends on the data sample. Given $\mathscr{L}$ is a Gaussian, $-\ln\mathscr{L}$ can be written as a second order polynomial

$$-\ln\mathscr{L}' = -\sum_j n_j \ln\lambda_j = -a(m - M_W^{fit})^2 + b$$
(4.21)

with the minimum in M_W^{fit}. The spread $\Delta M_W^{fit} = \sigma_\mathscr{L}$ of the Gaussian $\mathscr{L}$ can be obtained by varying $-ln\mathscr{L}$ by $1/2$ and is therefore given by $\Delta M_W^{fit} = \sqrt{\frac{1}{2a}}$. The shape of the likelihood function, as well as $(-\ln\mathscr{L})$, is shown in figure 4.17, together with the result of a fit to a Gaussian and a polynomial, respectively.

4.5.2 The Different Jet Pairing Likelihood Classes

To reject poorly reconstructed events that do not contain useful mass information, all events are required to have 5-C fit probability exceeding 1% and a 4-jet (5-jet) JPLH larger than 0.4(0.42). It turns out however that amongst the remaining events, not all possess the same quality of W mass information. Dividing the events into separate classes with respect to their JPLH guarantees that better reconstructed events gain greater impact such that the statistical error decreases. In addition, the contribution of combinatorial background varies with the JPLH as can bee seen in figure 4.18 and 4.19.

---

[5]It was also tested to decrease the test size but since spectra at more mass points would be needed, the computing time increases. 50 MeV is sufficiently small to provide an appropriate fit to the likelihood contour, which will be shown by the pull distributions in section 4.5.3.

[6]The best indication for sufficient statistics is the study of the pull distribution, which will be done in 4.5.3.
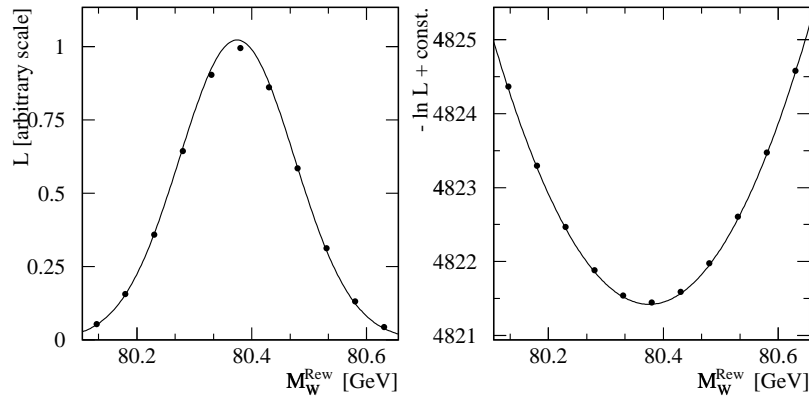
Figure 4.17: Likelihood $\mathscr{L}$ (left) and Log-Likelihood contour $-\ln\mathscr{L}'$ (right) together with fits to a Gaussian and a polynomial, respectively.

These two figures show the JPLH distributions for both, 4- and 5-jet WW events. An event is treated as a five jets if its jet resolution parameter exceeds a certain threshold $\ln y_{45} > -6.8$, otherwise it is reconstructed as a 4-jet event.
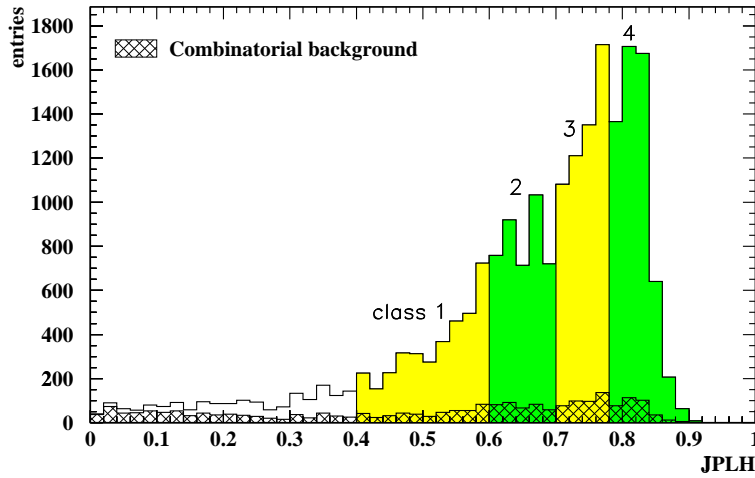
Figure 4.18: JPLH distribution for 4-jet events ($\ln y_{45} < -6.8$) and the four different likelihood classes.

best comb.	class 1	class 2	class 3	class 4
Range of JPLH	$0.4 - 0.6$	$0.6 - 0.7$	$0.7 - 0.78$	$0.78 - 1.0$
Expected events	80	84	101	100

Table 4.1: The different likelihood classes for 4-jet events ($\ln y_{45} < -6.8$).
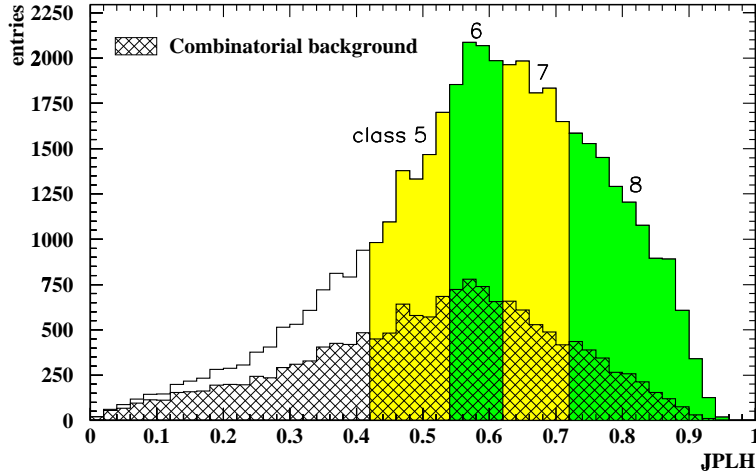
Figure 4.19: JPLH distribution for 5-jet events ($\ln y_{45} > -6.8$) and the four different likelihood classes for the best jet combination.

best comb.	class 5	class 6	class 7	class 8
Range of $JPLH_1$	$0.42 - 0.54$	$0.54 - 0.62$	$0.62 - 0.72$	$0.72 - 1.00$
Expected events	167	161	184	198

2nd best comb.	class 9	
Range of $JPLH_2$	$0.42 - 1.00$	if $p_{2nd}^{5\text{-C}} > \frac{1}{2} p_{1st}^{5\text{-C}}$
Expected events	234	

Table 4.2: The different likelihood classes for 5-jet events ($\ln y_{45} > -6.8$).

The events are filled into different M_W^{5-C} distributions and are then compared to the corresponding reweighted spectra, obtaining a likelihood value (4.20) for each single class that are finally added up before the actual likelihood fit (4.21) is performed to extract the W mass and its statistical error. A list of the classifications and their cuts are shown in table 4.1 and 4.2 and the corresponding mass distributions are illustrated in figure 4.20 and 4.21. In principle, if only enough Monte Carlo statistics would exist, one could think of even more different classes, but this approach breaks down as soon as the reweighted spectra for the different classes would not have enough entries anymore and start to be affected by fluctuations.

4.5.3 Ensemble Tests

This section discusses the results from bias tests, performed with multiple independent samples of events simulated by Monte-Carlo for different masses M_W^{MC}, each of the size corresponding to the recorded luminosity of real data. The number of samples for the different Monte Carlo masses are shown in table 4.3.

As it has been shown in reference [39], the number of different samples can be increased up to
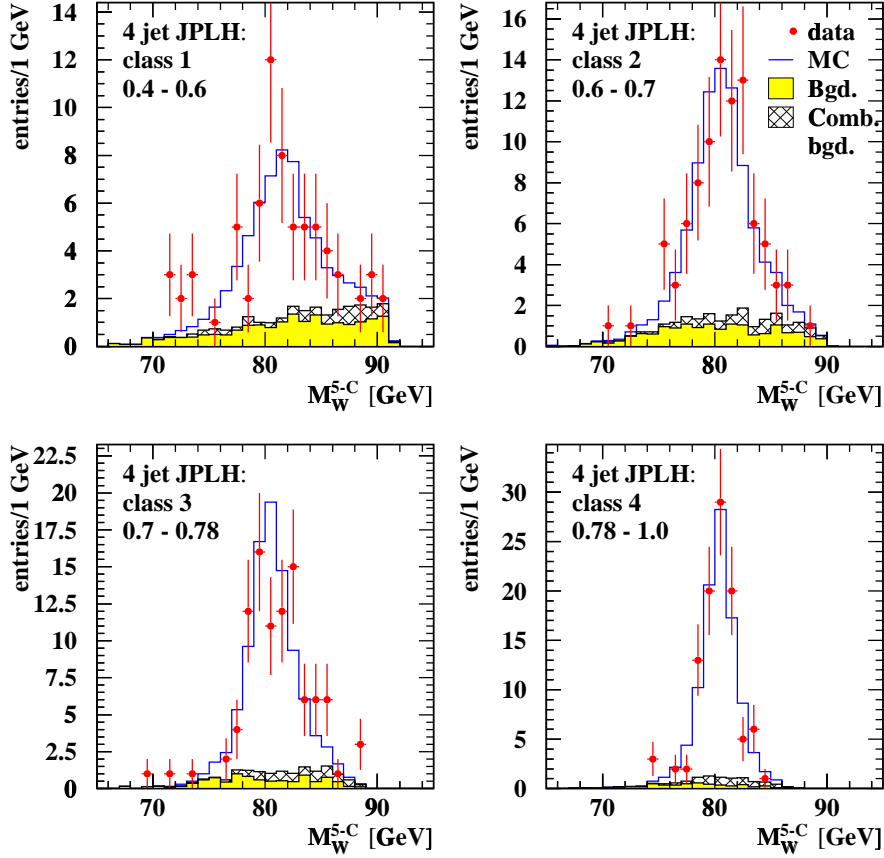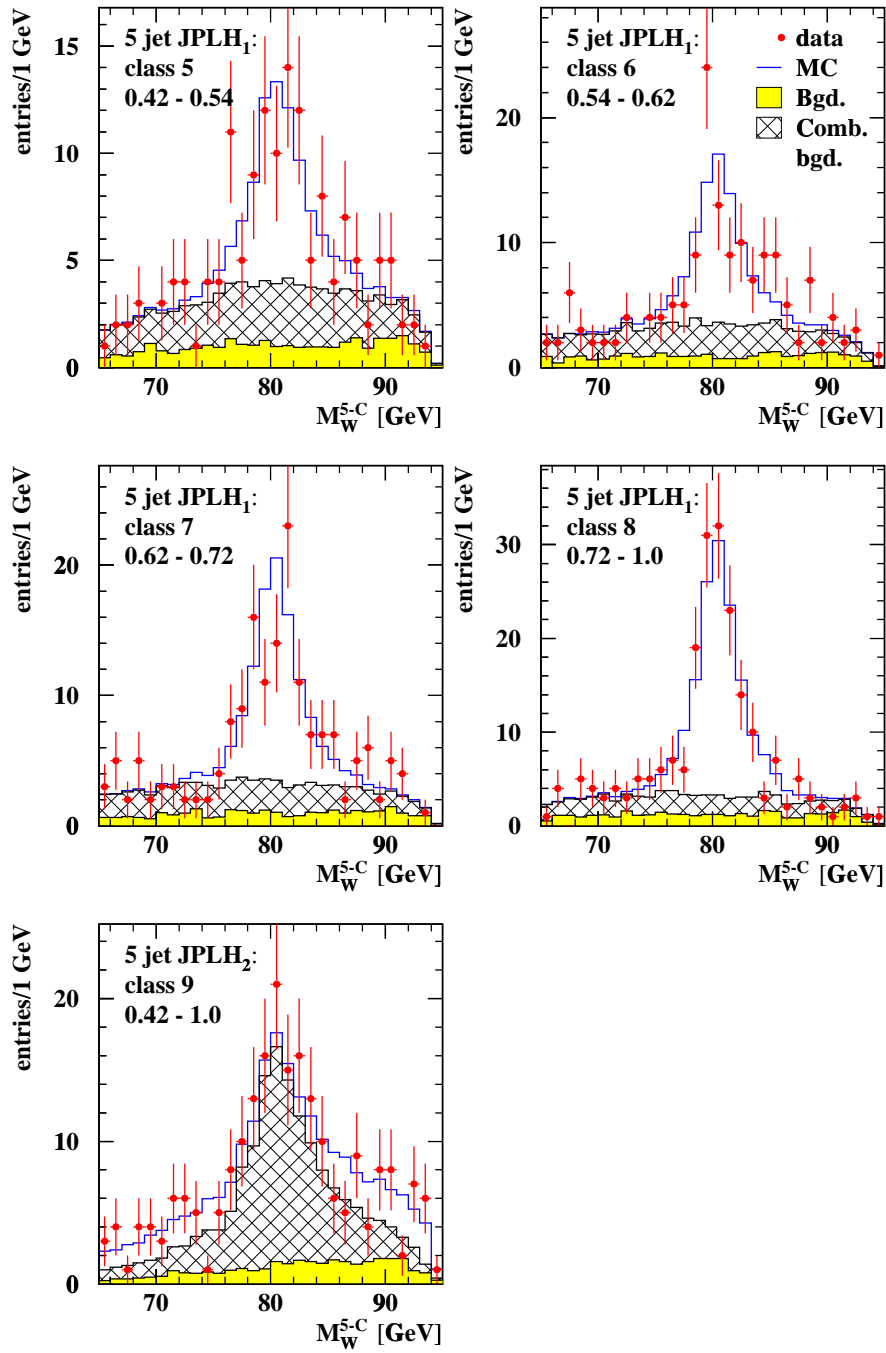
Figure 4.20: 5-C fitted mass distributions for the different JPLH classes for 4-jet events as defined in table 4.1.

$(N_{MC}/N_{data})^2$ in examinations concerning the spread of estimates—in our case the expected error—provided, the resampling is made by randomly assigning the events to the samples. However, the estimate itself, the mean of the resulting masses from each sample, might be biased in the case of correlated samples. In order to evaluate the expected error and to test whether the output of the Likelihood fit is correct, the analysis is repeated with 1000 randomly mixed MC samples for $M_W^{MC} = 80.33$ GeV, each of the size of the real data for $\sqrt{s} = 189$ GeV. The resulting distribution of the fitted masses for the 1000 samples can be seen in figure 4.22. Since the MC sample, where the subsamples originate from, is only 60 times bigger than the data size, the 1000 test samples are not 100% uncorrelated. Therefore the error on the mean value is $\Delta M_{mean} = \frac{\sigma_{exp}}{\sqrt{60}} \approx 13$ MeV, assuming no bias from correlations between the samples. The expected error, which is the spread $\sigma_{M_W^{fit}}$, is

$$\sigma_{exp} = 99.7 \pm 3.2 \text{ MeV.} \tag{4.22}$$

Figure 4.23 shows the pull distribution $(M_W^{fit} - M_W^{MC})/\sigma_{fit}$ originating from the ensemble test with independent MC samples for different masses as shown in table 4.3. In case of correctly es-

Figure 4.21: 5-C fitted mass distributions for the different JPLH classes for 5-jet events as defined in table 4.2.

M_W^{MC} [GeV]	N_{MC}/N_{data}
79.83	15
80.08	30
80.33	60
80.58	30
80.83	15

Table 4.3: Available simulated W masses and the corresponding number of independent MC samples N_{MC}/N_{data}.
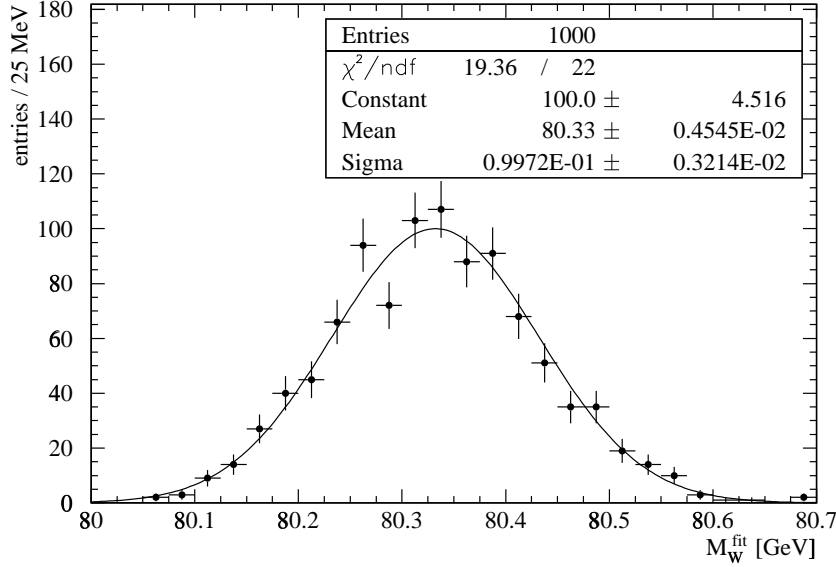
Figure 4.22: Results of the ensemble test with 1000 MC subsamples, generated at $M_W^{MC} = 80.33$ GeV.

timated errors σ_{fit} from the likelihood fit, this distribution should be a Gaussian with $\sigma_{pull} = 1$. A fit to a Gaussian shows that the centre of the distribution $mean_{pull} = -0.01 \pm 0.13$ is consistent with 0 and that the spread $\sigma_{pull} = 0.986 \pm 0.022$ is equal to 1 within the assigned errors. Also for the error on the mean of the pull distribution, the fact that only 60 samples can be 100% uncorrelated has to be taken into account. The fact, that the errors evaluated by the fit perfectly describe the errors from ensemble tests, proves that the best and the second best jet combination of 5-jet events are sufficiently independent. Similar ensemble test are also performed for different masses $M_W^{MC} = 79.83$, 80.08, 80.58 and 80.83 GeV in order to show that the measurement is free of any bias. The results are illustrated in 4.24, where $\langle M_W^{fit} \rangle - 80.33$ GeV is plotted versus $M_W^{MC} - 80.33$ GeV. This should lead to a linear function with slope 1 and without any offset. A linear fit to the points,

$$(\langle M_W^{fit} \rangle - 80.33 \text{ GeV}) = A_0 + A_1(M_W^{MC} - 80.33 \text{ GeV}), \qquad (4.23)$$

yields the offset of $A_0 = -4.2 \pm 8.3$ MeV and the slope $A_1 = 1.01 \pm 0.03$ which are consistent with

Entries	1000	
χ^2/ndf	8.382 / 13	
Constant	161.8 $\pm$	6.273
Mean	0.1322E-01 $\pm$	0.3121E-01
Sigma	0.9863 $\pm$	0.2214E-01
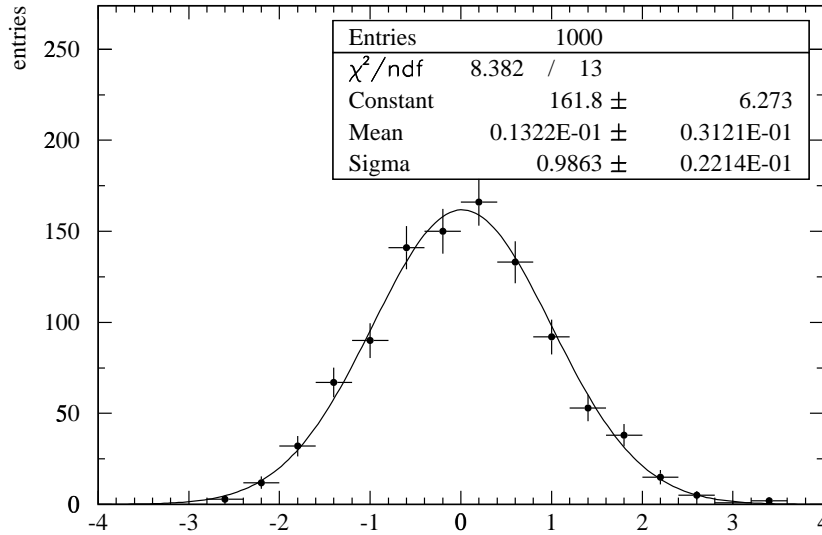
**Figure 4.23:** Pull distribution $(M_W^{fit} - 80.33\,\text{GeV})/\sigma_{fit}$ of the ensemble test with 1000 MC subsamples, generated for $M_W^{MC} = 80.33$ GeV.

0 and 1, respectively. The parameterisation $M_W - 80.33$ GeV was chosen to minimise the correlation between A_0 and A_1. The number of generated MC samples is symmetrically distributed around $M_W^{MC} = 80.33$ GeV, thus a different slope A_1 would still lead to the same over-all mean $\langle M_W^{fit} \rangle = A_0 + 80.33$ GeV.

4.6   Comparison of Methods

Forcing all events to four jets and requiring a 5-C fit probability larger than 0.01 leads to a rejection of about 19% of all preselected $W^+W^- \rightarrow q\bar{q}q\bar{q}$ events. Picking the correct jet combination out of the three possibilities to pair two out of four jets together using a jet pairing likelihood selection (JPLH) as described in section 4.4.3 leads to an overall efficiency of 57% of correct jet pairings entering the analysis with a cut on the JPLH at 0.4.

To consider all events as five jets recovers formerly rejected events and leads to about 93% of preselected 4-quark events with at least one jet combination with a 5-C fit probability exceeding 0.01. On the other hand, since the jet pairing is more difficult and the number of combinations increases to ten, a 5-jet JPLH, including the 5-C fitted mass as a likelihood variable, yields an overall efficiency of 59% correct combinations with a cut on the JPLH at 0.42, i.e. about 2% more than in the case of four jets. However, the amount of combinatorial background is much higher for the 5-jet case (compare figures 4.18 to 4.21) and taking the W mass $M_W^{5\text{-C}}$ itself as a likelihood variable in order to determine the correct combination leads to a degraded sensitivity as discussed in section 4.4.3. Thus, treating all events as five jets does not yield a better resolution. Therefore, the influence of mixing 4- and 5-jet events, depending on the cut on the jet resolution parameter $\ln y_{45}$ (see equation 4.2), and an optimal
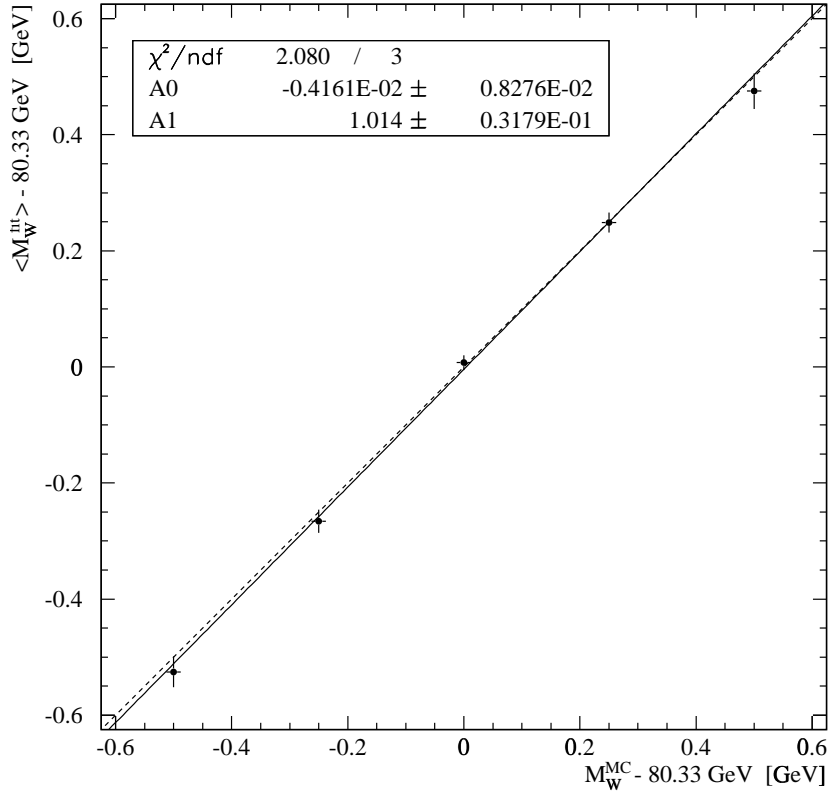
Figure 4.24: The mean of the fitted masses $\langle M_W^{fit} \rangle - 80.33$ GeV for each ensemble test versus the MC mass $M_W^{MC} - 80.33$ GeV. The solid line shows a line fit $(\langle M_W^{fit} \rangle - 80.33 \text{ GeV}) = A_0 + A_1 (M_W^{MC} - 80.33 \text{ GeV})$, while the dashed line shows the ideal dependency $\langle M_W^{fit} \rangle \equiv M_W^{MC}$.

distinction whether to treat an event as four or five jets is studied in this analysis and presented in this section.

The results are illustrated in figure 4.25. This figure illustrates both, the fraction of events treated as four jets (figure 4.25a)) and the resulting expected error for the different analyses (figure 4.25b)), depending on the cut on $\ln y_{45}$ in order to distinguish between 4- an 5-jet like events. The higher the on cut $\ln y_{45}$, the more events are reconstructed as four jets. The shown expected errors arise from statistics only (systematic effects are not included) and are calculated from the weighted average from 3200 subsamples in total for different Monte Carlo masses between 78.83 and 80.83 GeV.

Figure 4.25b) compares the following four analyses:

- with only two classes, a 4-jet and a 5-jet class, for the best jet combination from a jet pairing selection including the 5-C corrected W mass for the case of five jets (blue filled circles),

- the same but with the four jet events split up into four bins of JPLH as defined in table 4.1 (stars in magenta),

- as described in this thesis, i.e. without the W mass as an additional variable for the jet pairing
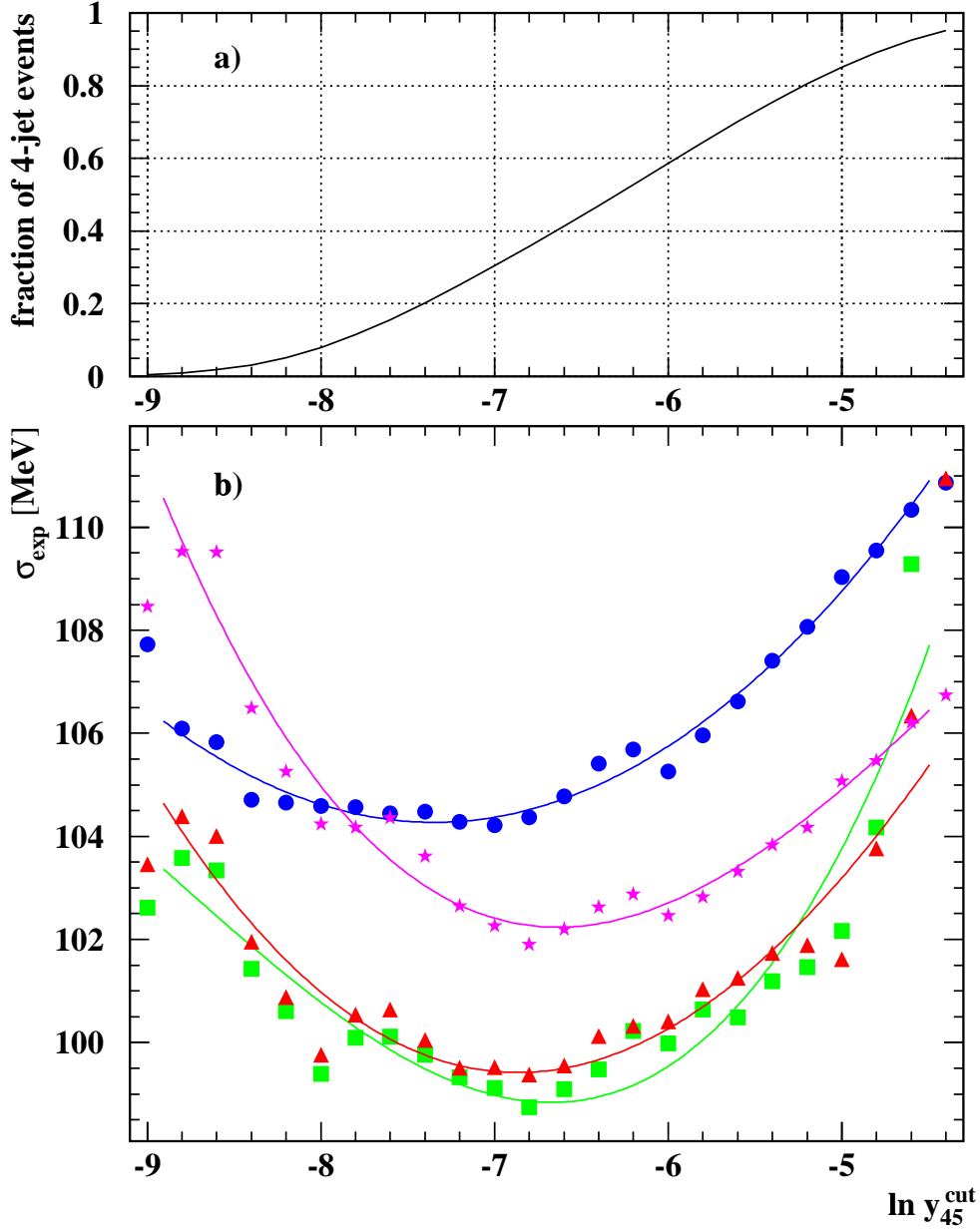
Figure 4.25: The fraction of events treated as four jets (a) and the statistical error of M_W, depending on the cut on $\ln y_{45}$ (b): The blue filled circles show results with the 5-C corrected mass as an additional variable in the 5-jet JPLH. The stars in magenta are from the same analysis, but with four 4-jet classes as defined in table 4.1. The red filled triangles show the analysis as performed in this thesis at $\ln y_{45}^{cut} = -6.8$. Herein the mass is taken out of the JPLH and also the second best jet combination is taken into account with a classification defined in table 4.2. Finally, the green squares illustrate the same analysis but with an additional class for the third best 5-jet combination, if its 5-C fit probability is larger than one third of the fit probability of the best jet pairing. The solid lines are fits to third order polynomials and are shown for illustrative purposes only.

but with the second best combination and a classification as defined in the tables 4.1 and 4.2 (red triangles) and

- the same with another class of the third best jet pairing of 5-jet events that have a sufficient fit probability $p_{3rd}^{5-C} > \frac{1}{3} p_{1st}^{5-C}$ (green squares).

The uncertainty of the presented expected errors is about 2 MeV for values of $(\ln y_{45})_{cut}$ not too far from -6.8. However, the error bars are not shown, since the statistical fluctuations *between* the shown points is smaller because of the correlation between the different analyses and values of $(\ln y_{45})_{cut}$ due to the same choice of subsamples. The results for very small and very big values of the cut $(\ln y_{45})_{cut}$ are less reliable since the errors of the reweighted histograms are not negligible anymore when the statistics in these histograms drop. This is especially the case for the magenta, red and green points— the stars, triangles and squares—on the left side (and for the red and green points–the triangles and squares —on the right side) of the diagram, since the 4-jet (5-jet) events are split up into even smaller bins of the JPLH. This is the reason for the big fluctuations at the far left and right of figure 4.25b).

From this figure one can conclude that taking also five jets into account drops the statistical error of the W mass measurement by $5-6\%$. Dividing the 4-jet events into four classes with respect to their JPLH yields another 2 MeV. It also illustrates that dropping the W mass out of the JPLH and including also the second best combination is not just comparable but even gains another $2-3$ MeV when introducing also different JPLH classes for events reconstructed as five jets.

The dependency of the statistical error on the cut on the resolution parameter $\ln y_{45}$ suggests an optimal cut at around $(\ln y_{45})_{cut} = -6.8$ where 36% of the selected events are reconstructed as four jets.

4.6.1   An Alternative Analysis: 2D Reweighting

Performing the mass analysis as described above involves a one-dimensional fit to the W mass. The single value of the reconstructed mass for each event originates from the equal-mass constraint in the 5-C fit (see section 4.4.1). The width of the W boson, however, is not zero (it was determined by the OPAL experiment to $\Gamma_W = 2.02 \pm 0.16^{\text{stat.}} \pm 0.10^{\text{syst.}}$ GeV [10]) and the distributions of the 3-jet and the 2-jet W masses in a 5-jet reconstruction are only identical for a pure sample without combinatorial and non-WW background. Therefore, there was the hope to decrease the error on the W mass by dropping the equal-mass constraint and performing a reweighting fit involving two-dimensional distributions in the two 4-C fitted W masses. In this case, the analysis is automatically sensitive to the mass difference of the two reconstructed W bosons. Since all the variables that are used to determine the correct jet combination (see section 4.4.3) are correlated to either the mass difference or the 5-C fitted mass itself, no particular jet pairing is performed in this first attempt of a two-dimensional reweighting analysis: Any jet combination of an event with both 4-C fitted W masses in the window between 60 and 100 GeV and with a 5-C fit probability exceeding 1% is accepted. Figure 4.26 illustrates the number of jet combinations per event that fulfil these requirements. An event is considered as four jets if its jet resolution parameter $\ln y_{45}$ is smaller than -6.4, otherwise it is reconstructed as five jets. The particular choice of the cut on $\ln y_{45}$ is not originating from an optimisation as discussed for the one-dimensional analysis. The cut $(\ln y_{45})_{cut} = -6.4$ was chosen, because it divides the event sample into two parts of approximately equal size.

The diagrams in figure 4.27 show the two-dimensional mass distributions for correct combinations as well as combinatorial background. One can clearly see the kinematic limit at $M_1 + M_2 = 189$ GeV. In the case of four jets, the combinatorial background is flat. For 5-jet events, the contribution from

m
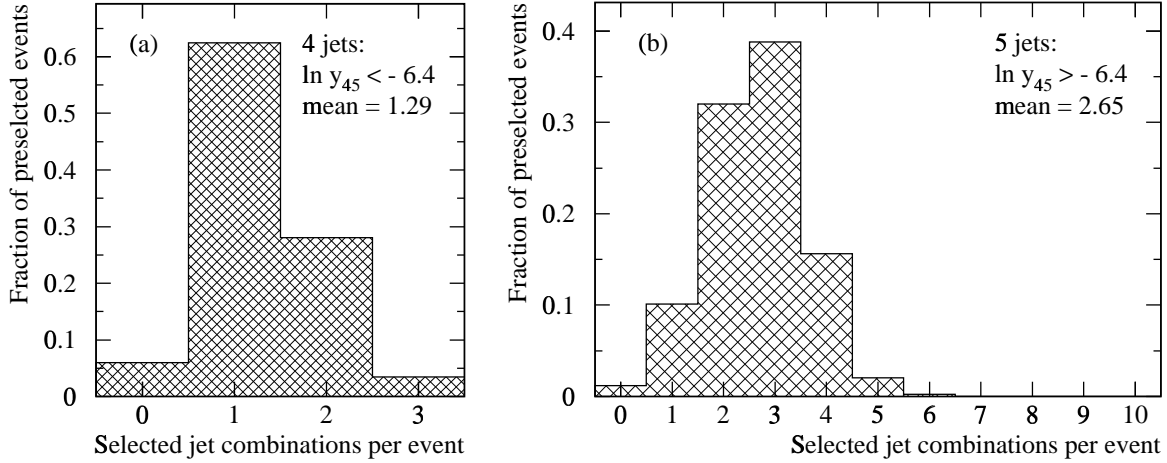
Figure 4.26: Number of jet combinations with a 5-C fit probability larger than 0.01 and both 4-C fitted W masses in the range $60 - 100 \, \text{GeV}$: Figure (a) shows the events considered as four jets ($\ln y_{45} < -6.4$), figure (b) shows those events reconstructed as five jets ($\ln y_{45} > -6.4$). The diagrams are normalised with respect to all preselected WW events that have at least one jet combination with a 5-C fit probability greater than 0.01. Non-WW background is not included.

wrong jet pairings is asymmetric: On average, the 3-jet system has a larger invariant mass than the 2-jet W. This is not the case for correct combinations only, as shown in figure 4.27 (b).

In the reweighting technique as described in section 4.5.1, the errors on the entries of the reweighted histograms are neglected. For sufficiently large numbers of events contributing to each bin of the reweighted distribution, this is a good approximation. However, large fluctuations in these distributions lead to uncontrollable biases. Of course an increase of the bin size decreases the fluctuations but it also smoothens out the shape of the distribution itself and therefore decreases the sensitivity to the W mass.

The figures 4.28 (a) and (b) illustrate the fluctuations in the distributions of the $q\bar{q}$ and ZZ background. Since this is already the whole available MC background sample, the background contribution to the reweighted histograms is smoothened in order to decrease the effect of fluctuations in the background distributions: The entry $b_{ij}^{(\text{non-}WW)}$ of each bin (i,j) in the two-dimensional diagram becomes

$$b_{ij}^{(\text{non-}WW)} \rightarrow \tilde{b}_{ij}^{(\text{non-}WW)} = \frac{\sum_{k,l} b_{ij}^{(\text{non-}WW)} \cdot \exp\left\{-\frac{(m_i - m_k)^2 + (m_j - m_l)^2}{\sigma^2}\right\}}{\sum_{k,l} \exp\left\{-\frac{(m_i - m_k)^2 + (m_j - m_l)^2}{\sigma^2}\right\}}, \qquad (4.24)$$

where m_i, m_j denote the two W masses associated to the bin (i,j) and the width σ of the Gaussian weight is set to $0.8 \, \text{GeV}$. The resulting smoothened background contributions to the reweighted spectra are shown in the figures 4.28 (c) and (d) for four and five jets, respectively. As it was discussed in section 4.5.1, a reweighting technique is bias free provided the event simulation is correct, but any smoothing of the reweighted histograms also modifies the shape of the mass distributions. Therefore, the results will be corrected for bias effects. Results from bias test, similar to those of the one-dimensional scheme as described in section 4.5.3, can be seen in figure 4.29, where the mean values $\langle M_W^{fit} \rangle - 80.33 \, \text{GeV}$ of multiple tests are plotted versus the corresponding Monte Carlo masses $M_W^{MC} -$
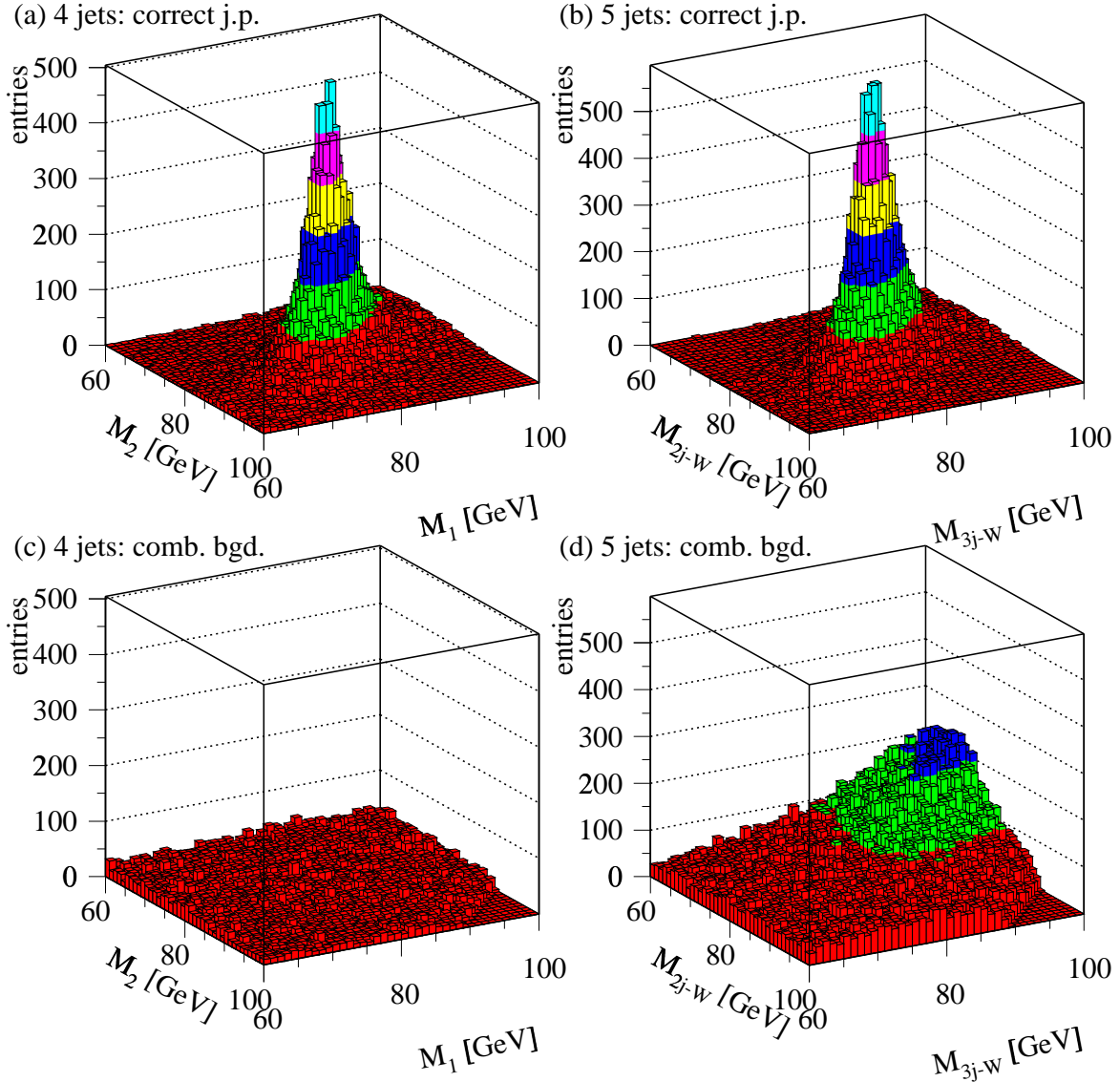
Figure 4.27: Two-dimensional mass distributions for four and five jet events: Correct combinations for 4-jet (a) and 5-jet (b) events, combinatorial background of 4-jet events (c) and incorrect 5-jet combinations (d).

80.33 GeV. A line fit to the data points yield a shift of 9 ± 8 MeV and a slope of 0.98 ± 0.03. The resulting mass shift is about one standard deviation away from zero, while the slope is consistent with 1 within the errors assigned.

The figures 4.30 show the results from ensemble tests as introduced in section 4.5.3. The uncorrected expected error is

$$\sigma_{exp}^{2D} = 95.5 \pm 3.2 \text{ MeV}. \tag{4.25}$$

The pull distribution $(M_W^{fit} - 80.33 \text{ GeV})/\sigma_{fit}$ in figure 4.31 shows that the errors estimated in the fit correctly describe the spread of the results from the ensemble test. The spread $\sigma = 0.993 \pm 0.022$
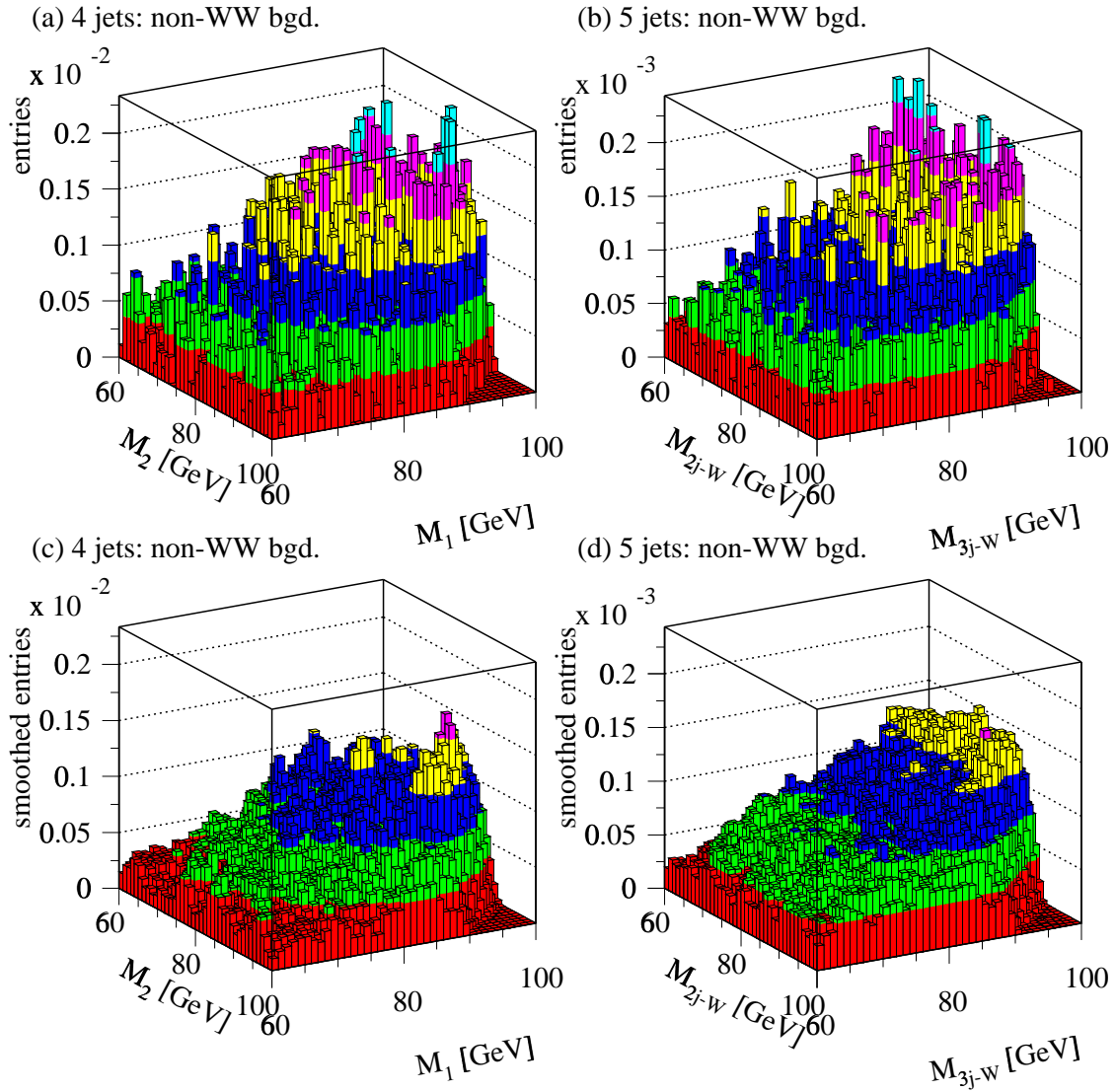
Figure 4.28: The contribution of the non-WW background to the reweighting histograms: The figures (a) and (b) show the unmodified "W mass" distributions for four and five jets respectively. These distributions are smoothened using Gaussian weights resulting in the distributions (c) for four and (d) for five jets.

of the pull distribution is consistent with 1. This result illustrates that those reconstructed masses from correct and incorrect jet combinations that are considered in the analysis are sufficiently uncorrelated. Compared to the result of the one-dimensional reweighting fit (see section 4.5.3), the expected error is reduced by about 4%.

Using this two-dimensional reweighting technique for hadronic events corresponding to 183 pb^{-1} of data recorded with the OPAL detector in 1998, the mass of the W boson is determined to
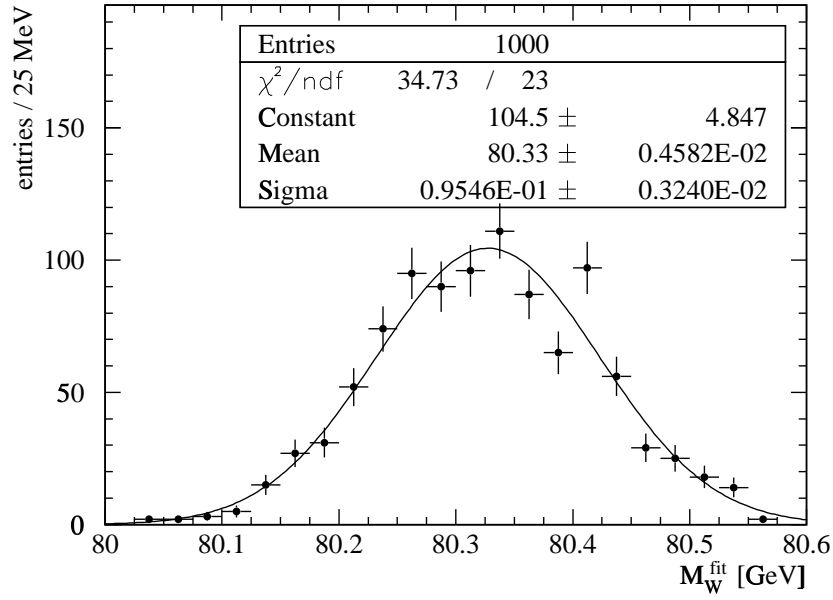
$$M_W^{2D} = 80.404 \pm 0.095^{stat.} \text{ GeV.} \tag{4.26}$$

This result is not corrected for bias effects and the error is statistical only.
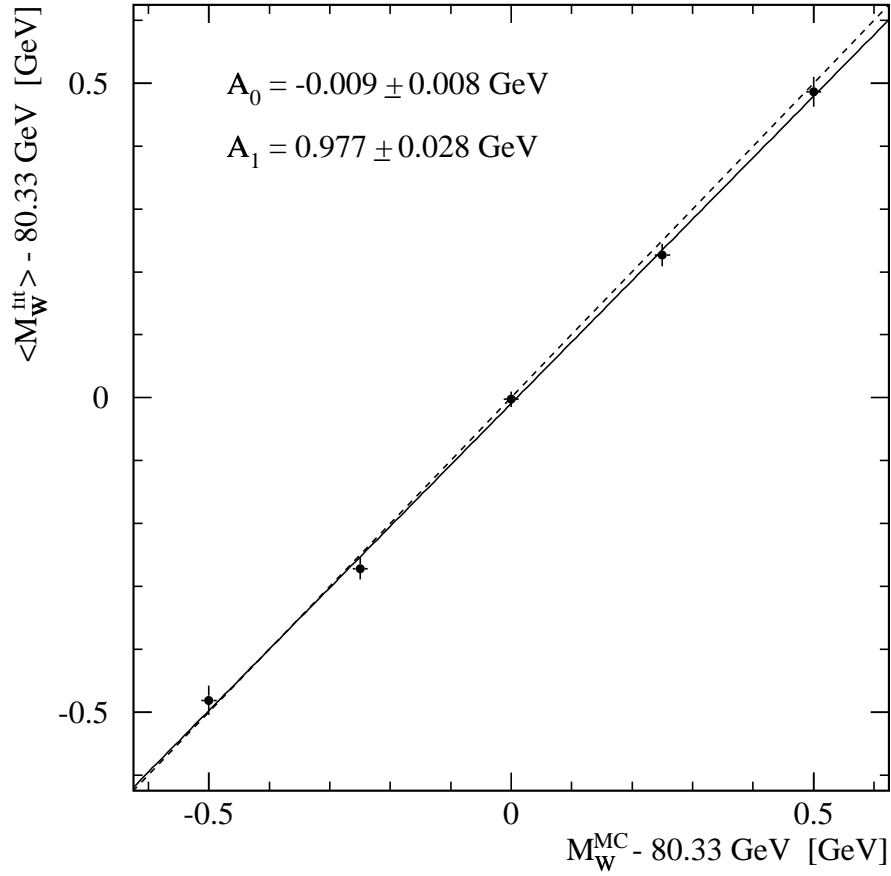
Figure 4.29: Result from a bias test of the 2-dimensional analysis: the mean of the fitted masses $\langle M_W^{fit} \rangle -$ 80.33 GeV for each ensemble test versus the MC mass $M_W^{MC} - 80.33$ GeV. The solid line shows a line fit $(\langle M_W^{fit} \rangle - 80.33\,\text{GeV}) = A_0 + A_1(M_W^{MC} - 80.33\,\text{GeV})$, while the dashed line shows the ideal dependency $\langle M_W^{fit} \rangle \equiv M_W^{MC}$.

Note, that this two-dimensional reweighting analysis is only a first attempt to show its feasibility. It is not optimised yet, neither for an appropriate mixing of 4- and 5-jet like events, nor for an optimal treatment of the non-WW background. For further studies, more statistics would certainly be needed for both the signal and the non-WW background simulated by Monte Carlo. Introducing a jet pairing likelihood, for instance based on the probability density functions of the weights of matrix elements, in order to discard incorrect jet combinations, would certainly further decrease the error and would allow the introduction of different JPLH classes as done for the one-dimensional scheme.

Entries		1000	
χ^2/ndf	34.73	/ 23	
Constant		104.5 $\pm$	4.847
Mean		80.33 $\pm$	0.4582E-02
Sigma		0.9546E-01 $\pm$	0.3240E-02

Figure 4.30: Results from the ensemble test of the two-dimensional analysis with 1000 MC subsamples, generated at $M_W^{MC} = 80.33$ GeV.

Entries		1000	
χ^2/ndf	15.84	/ 15	
Constant		160.7 $\pm$	6.231
Mean		-0.3084E-01 $\pm$	0.3143E-01
Sigma		0.9931 $\pm$	0.2230E-01
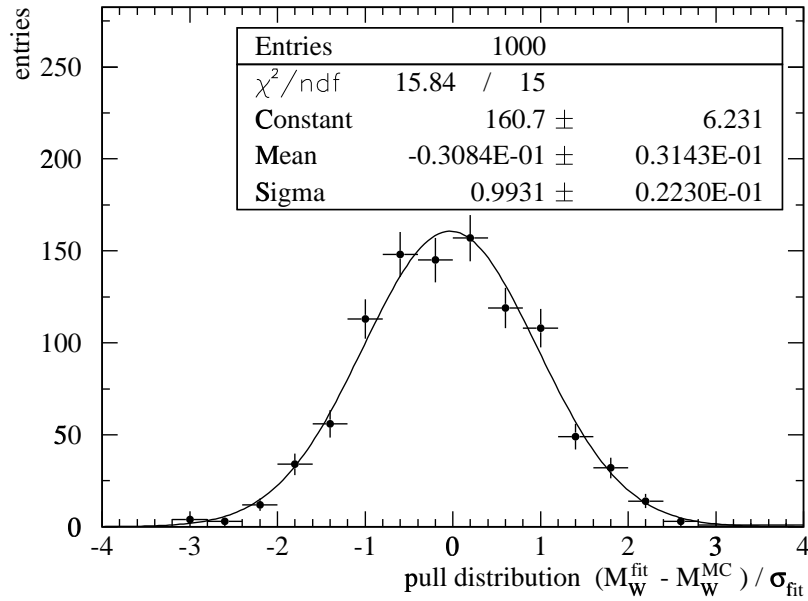
Figure 4.31: Pull distribution $(M_W^{fit} - 80.33 \text{ GeV})/\sigma_{fit}$ of the ensemble test of the two-dimensional analysis with 1000 MC subsamples, generated at $M_W^{MC} = 80.33$ GeV.

Chapter 5

Systematic Uncertainties

In the framework of this analysis there are basically two systematic tests that have been performed, mainly to study the systematic effect arising from the inclusion of 5-jet events in the analysis: The dependency of the colour reconnection effect on the fraction of 5-jet events that enter the analysis was examined, and the stability with respect to the jet structure of the $q\bar{q}$ background was investigated. Other systematic checks were not part of the thesis and will only briefly be mentioned. A summary of the different systematic effects and their assigned uncertainties is given in table 5.1. The contributions from each of the different sources are added in quadrature to yield the total systematic uncertainty.

5.1 Colour Reconnection and Bose-Einstein Correlation

Since the decay length of the W boson produced in LEP2 collisions (~ 0.1 fm) is smaller than the typical scale at which a quark fragments into hadrons (~ 1 fm), final state interaction (FSI) effects between the decay products of the two W bosons can occur which could bias the measurement of the mass of the W boson in the 4-quark channel as the decay products may have a significant space-time overlap.

The two effects considered are the *Bose-Einstein correlation* (BEC) [40, 41], which enhances the production of identical particles with integer spin that are close in phase-space, and the *colour reconnection* (CR) effect, the exchange of soft gluons that can lead to a colour flux between partons from different W bosons [42].

While the Bose-Einstein correlation is not examined within the framework of this thesis (resulting systematic errors on the W mass from OPAL studies [10] are shown in table 5.1), the effect of introducing 5-jet events on the mass bias arising from CR is studied with the model that is taken as the current conservative estimate of a plausible description of colour reconnection in OPAL analyses [10]. This CR model, the *Sjöstrand-Khoze* model I (SK I) with $\rho = 0.9$ as described in [43], gives the largest mass shift of those models that are not disfavoured by previous LEP analyses as discussed in the reference [10]. The resulting mass shift is considered as the CR contribution to the systematic uncertainty.

In order to quantify the effect of colour reconnection on the mass determination of $W^+W^- \to q\bar{q}q\bar{q}$ events, Monte Carlo samples (see table B.3), each of the size of the recorded data, with and without the CR effect implemented by the SK I model ($\rho = 0.9$), are compared such that the events in the compared samples are identical up to the end of the parton shower. Figure 5.1 shows the difference $\Delta M_{CR} = M_{CR}^{fit} - M_{no\,CR}^{fit}$ of W mass fits with and without this CR effect for the present analysis (cut on $\ln y_{45} = -6.8$). The mean value of this distribution, the mass shift, is taken as the systematic

uncertainty.

The mass shift and the *r.m.s.* of the ΔM_{CR} distribution is shown in figure 5.2 as a function of the jet resolution parameter $\ln y_{45}$ (see section 4.1.1). The shown mass shift is the mean of the difference of 63 independent samples with and without CR. This diagram shows that the effect is only slightly dependent on the choice of whether to consider an event as four or five jets. At $\ln y_{45} = -6.8$ where the measurement is performed, the mass shift is

$$\langle \Delta M_{\mathrm{CR}} \rangle = \langle M^{fit}_{\mathrm{CR}} - M^{fit}_{\mathrm{no\ CR}} \rangle = 51 \pm 7 \text{ MeV}. \tag{5.1}$$

A short remark: The spread of the ΔM_{CR} distribution for $(\ln y_{45})_{cut} = -6.8$, *r.m.s.* $= 55 \pm 5$ MeV, is smaller than the expected spread for completely independent samples: $\sigma(\Delta M^{(\mathrm{indep.})}_{\mathrm{CR}}) = \sqrt{2} \cdot \sigma_{exp}(M^{\mathrm{fit}})$ ≈ 140 MeV (compare to equation 4.22). The *r.m.s.*, and therefore the uncertainty of the mass shift, is smaller, since only 34% of the event have a different fragmentation for $\rho = 0.9$.
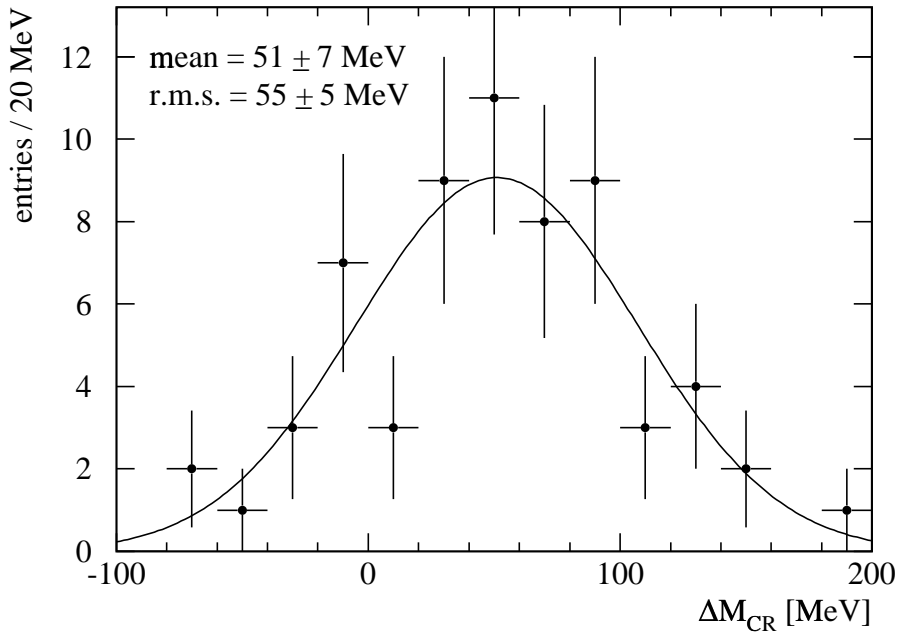

Figure 5.1: The difference of the fitted mass $\Delta M_{\mathrm{CR}} = M^{\mathrm{fit}}_{\mathrm{CR}} - M^{\mathrm{fit}}_{\mathrm{no\ CR}}$ for samples with and without the colour reconnection effect as described by the SK I model with $\rho = 0.9$.

5.2   Simulation of $q\bar{q}$ Background

The largest number of events from non-WW background comes from $\gamma/Z^0 \rightarrow q\bar{q}(\gamma)$ events (the so-called $q\bar{q}$ background) with a 4- or 5-jet like topology from hard gluon radiation from the initial partons. Since these processes are already higher orders in α_s, it is very difficult for them to be simulated.

Therefore the $q\bar{q}$ background distributions were varied in the samples in ensemble tests while they were left unchanged in the reweighted spectra in order to study the influence of incorrectly simulated $q\bar{q}$ background. The special interest lies in the comparison of the resulting deterioration with respect to analyses that only use 4-jet events, a study that has not been performed with OPAL data so far.
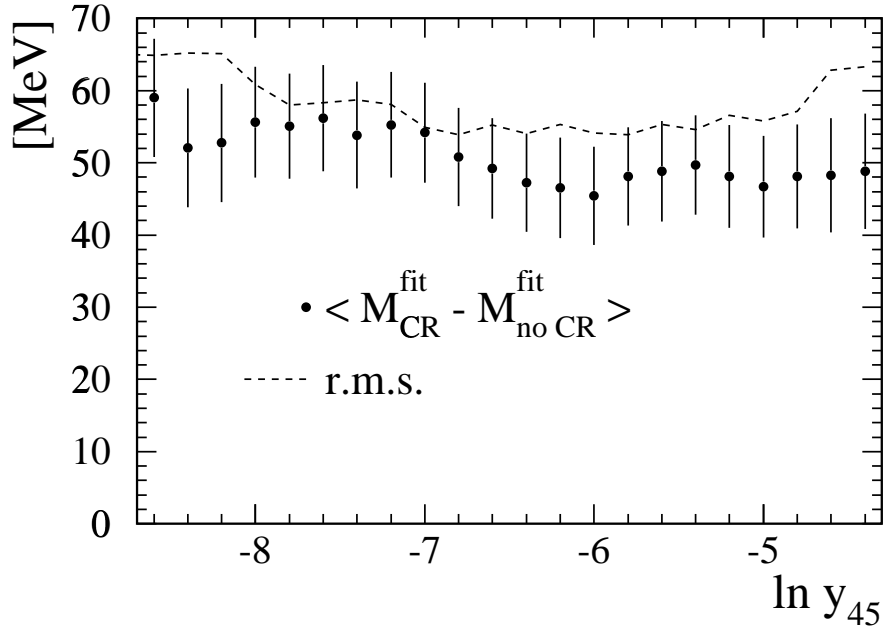
Figure 5.2: Colour reconnection studies with the SK I ($\rho = 0.9$) model as a function of the cut on $\ln y_{45}$. The points with the assigned error bars are the mean of the difference from 63 samples simulated by Monte Carlo with and without the effect of colour reconnection. The dotted line illustrates the the spread of the distribution of theses differences.

For these studies, the distribution of the jet resolution parameter of the $q\bar{q}$ events was modified, by varying the probability of an event to be chosen to contribute to a certain sample in the ensemble test in a $\ln y_{45}$ dependent way. This is done by weighting the probability with a factor that is depending on the jet resolution parameter y_{45} of the considered event. This weight, which is simply a linear function with a given slope and a value of 1 at the mean of the original $\ln y_{45}$ distribution, is shown in the lower diagram of figure 5.3 for different slope values. The resulting $\ln y_{45}$ distributions are shown in the upper diagram: With a positive slope, the distribution is varied with a preference of higher values of $\ln y_{45}$ while it is shifted towards lower values for negative slopes.

For different slopes of the weight function and various values of the cut $(\ln y_{45})_{cut}$[1], bias tests were performed. The determined biases and slopes for these tests are shown in figure 5.4. The absolute effect of these variations of the $q\bar{q}$ background is relatively small with respect to the absolute error assigned to both the slope and the bias: For a slope of the weighting factor of ± 0.2, the mass shift is less then 4 MeV. On the other hand, figure 5.4 demonstrates that the applied distortion leads to an effect that varies with different cuts on the jet resolution parameter $\ln y_{45}$. While for pure 5- or 4-jet analysis (very small or big values of $\ln y_{45}$) the effect is quite small ($\lesssim 1$ MeV), for certain compositions of 4- and 5jet events, the deviation increases up to about 4 MeV.

Note that there is no hint whether the performed variations really are sufficiently large in order to account for possible systematic effects from incorrectly simulated QCD background. The choice of this particular weighting with a slope of ± 0.2 was chosen because it leads to a modification of the $\ln y_{45}$ distribution of the $q\bar{q}$ background from Monte Carlo simulations. Which is big enough to be

---

[1]This cut determines whether to reconstruct an event as four or five jets. The corresponding fraction of 4-jet events entering the analysis for a given value of $(\ln y_{45})_{cut}$ can be seen in figure 4.25.
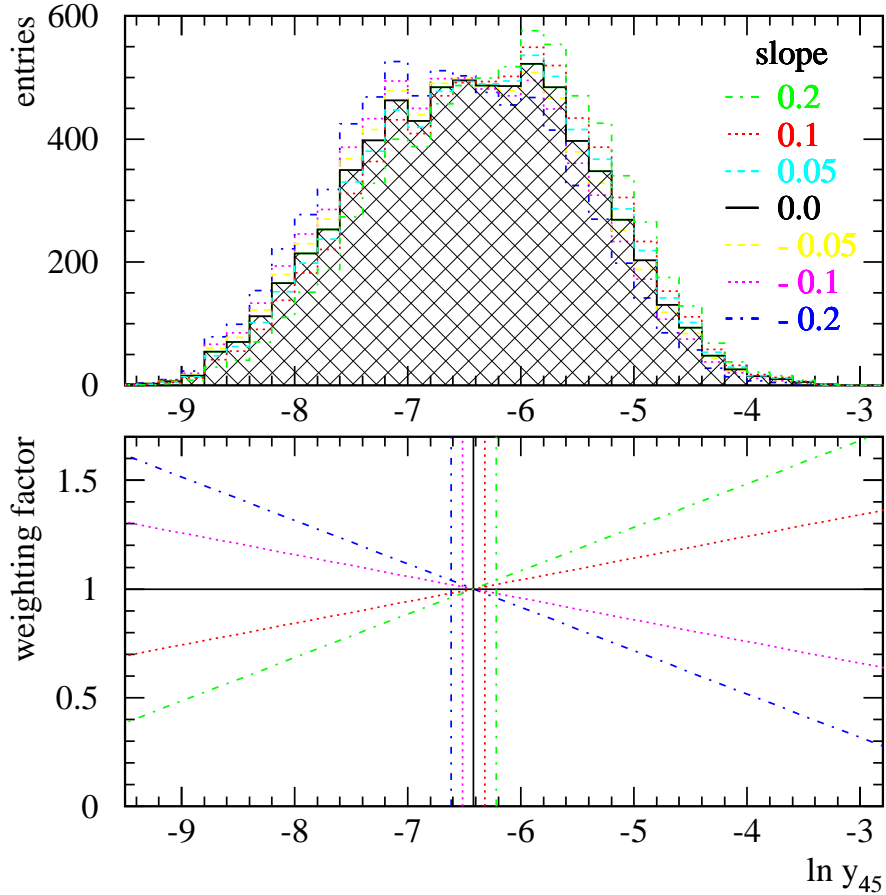
Figure 5.3: Variation of the $\ln y_{45}$ distribution of the $q\bar{q}$ background: The upper diagram shows the resulting shift in the $\ln y_{45}$ distribution of the $q\bar{q}$ background, when the probability for these events to contribute to a certain MC sample, for which the W mass will be evaluated, is not equal for all $q\bar{q}$ events but depending on the value of their jet resolution parameter $\ln y_{45}$. This probability is multiplied by a $\ln y_{45}$ depending weight, a linear function with a given slope and a value of 1 at the mean of the original $\ln y_{45}$ distribution as shown in the lower diagram. The vertical lines show the shift of the average value of $\ln y_{45}$ for the $q\bar{q}$ background for different slopes. The solid lines (slope 0) corresponds to the unmodified distribution.

examined with the $q\bar{q}$ data recorded in 1998.

The modification of the $\ln y_{45}$ distribution of the $q\bar{q}$ background, originating from this particular choice of the slope ± 0.2 of the weight, is sufficiently large in the sense that the $q\bar{q}$ data recorded in 1998 have enough statistics to be sensitive to such variations.

As for the assigned error from the background treatment, several tests including different fragmentation models and rescaling data taken at $\sqrt{s} \approx M_Z$ were performed in OPAL studies [10] which result in an uncertainty of 6 MeV on the measurement of M_W.

5.3   Other Systematic Uncertainties

Tests of other systematic uncertainties than the effect of colour reconnection were not performed within this analysis and are therefore only briefly mentioned in this section. The systematic checks and
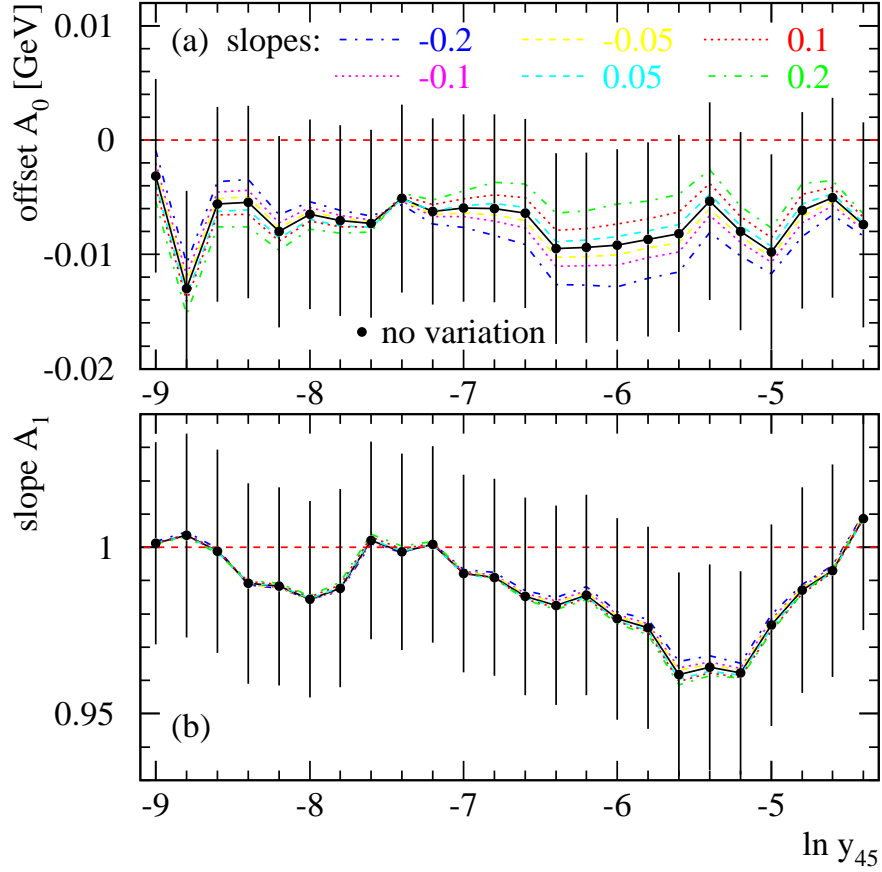
Figure 5.4: Influence of the variation of the $q\bar{q}$ background for different values of the cut on the jet resolution parameter $\ln y_{45}$ as described in 5.2. The upper diagram shows the offset A_0, the lower shows the slope A_2 of bias tests (see section 4.5.3) performed for different $\ln y_{45}$ distributions of the $q\bar{q}$ background and various values of the cut on $\ln y_{45}$.

the resulting systematic errors come from OPAL studies of the W mass in the 4-quark channel with the same data at the centre-of-mass energy of $\sqrt{s} = 189$ GeV [10]. That analysis, also using a reweighting technique, mainly differs in the method to determine the correct jet pairing for 5-jet events and the event classification as well as in the cut between 4- and 5-jet like events from the analysis performed in this thesis, but these differences are believed to only slightly affect the systematic uncertainties. The results for uncertainties exceeding 5 MeV can be seen in table 5.1.

The average LEP beam energy (see section 3.1.2) for the data taken in 1998 is currently known with a precision of 20 MeV [44, 14]. This leads to a systematic uncertainty on M_W of 16 MeV [10].

In order to describe the event shape variables and inclusive particle production rate of $W^{\pm} \rightarrow q\bar{q}'$ decays, the JETSET model is used, tuned to OPAL hadronic data at the Z^0 resonance [45]. A variation of the JETSET fragmentation parameters by $\pm 1\sigma$ about their tuned values yields a shift of 20 MeV on M_W in the hadronic channel [10] while an earlier OPAL tune of the JETSET model [46] biases the fitted mass by 30 MeV [10]. Furthermore, the JETSET string model was replaced by the HERWIG cluster model and the ARIADNE colour dipole model [47], applied to identical events differing only in the modelling of the hadronization. These tests give differences of $M_W^{\text{JETSET}} - M_W^{\text{HERWIG}} = -11 \pm 12$ MeV

Source of the error	$\sigma_{\text{syst.}}$ [MeV]
Colour reconnection	51
Bose-Einstein Correlations	67
Beam Energy	16
Fragmentation	30
Background	6
MC statistics	10
Total systematic error	92

Table 5.1: Summary of the systematic uncertainties for the fit results for contributions exceeding 5 MeV. The test of the affect of colour reconnection (SK I, $\rho = 0.9$) has been performed for this analysis, for the results of the other contributions to the systematic error the reader is referred to OPAL studies [10].

and $M_W^{\text{JETSET}} - M_W^{\text{ARIADNE}} = 6 \pm 12$ MeV [10]. Based on these tests, an error of 30 MeV is assigned to the simulation of the fragmentation process.

The reweighted mass distributions are fitted to the data, neglecting uncertainties of the reweighted spectra. The finite statistics of the Monte Carlo samples used in the reweighting procedure yield an error of 10 MeV on M_W in the hadronic channel [10].

Chapter 6

Summary and Conclusions

In this work, a reweighting fit to the W mass spectrum of hadronic events recorded with the OPAL detector was performed and optimised with respect to an appropriate inclusion of 5-jet like events into the analysis.

Compared to previous OPAL measurements of the mass of the W boson in hadronic decays of W bosons [10, 33], the expected error was reduced by 4%.

This improvement was possible by optimising the treatment of 5-jet events. First it was tried to perform a jet pairing selection that was equally powerful without using the 5-C fitted mass as an additional variable in the likelihood selection of the best jet combination. In order to get rid of the correlation between this likelihood selection and the W mass, the latter was not taken into account in the jet pairing but the second best jet combination was also taken into consideration. This leads to a flat non-WW background for events reconstructed as five jets. The fact that the errors evaluated by the fit perfectly describe the errors from ensemble tests proves that the best and the second best jet combination of 5-jet events are sufficiently independent.

Changing the cut on the logarithm of the jet resolution parameter $\ln y_{45}$, which determines whether to reconstruct an event as four or five jets, from -5.6 to -6.8 was shown to minimise the expected error of the fit and reduced the fraction of events treated as 4-jets from 68 to 34%. The event classification with respect to the jet pairing likelihood was optimised for this analysis.

Furthermore, it was shown that an inclusion of 5-jet events does not increase the systematic uncertainty from the effect of colour reconnection. Systematic effects from the treatment of $\gamma/Z^0 \to q\bar{q}$ background were studied.

The result of the one-parameter fit to the W mass in the hadronic channel from 183 pb^{-1} data recorded with the OPAL detector in 1998 at the centre-of-mass energy $\sqrt{s} = 189$ GeV is

$$M_W^{4q} = 80.360 \pm 0.105^{stat.} \pm 0.093^{syst.} \text{ GeV}. \tag{6.1}$$

The expected error is

$$\sigma_{exp}^{stat.} = 100 \pm 3 \text{ MeV}. \tag{6.2}$$

In addition, a two-dimensional reweighting fit using both the masses of the two W bosons was performed and shown to be successful, although surely more Monte Carlo events are needed for both signal and background to reduce the systematic uncertainty from limited Monte Carlo statistics to a value comparable to this error in the one-dimensional fit. It was discussed, that for further studies more Monte Carlo statistics would be needed to reduce the fluctuations in the bin of the two-dimensional reweighted histograms. The result of the two dimensional fit with both W masses from a 4-C kinematic

fit is $M_W^{4q} = 80.404 \pm 0.095^{stat.}$ GeV. The given error is related purely to statistics, an estimation of the error arising from systematic effects was not made in this analysis, but it is assumed to be approximately the same than in the one-dimensional analysis apart from the effect of limited Monte Carlo statistics. The expected uncertainty happens to be $\sigma_{exp}^{stat.} = 95 \pm 3$ MeV which is about 4% smaller than the expected error of the one-dimensional reweighting analysis.

Both results are consistent with previous OPAL measurements in the hadronic channel as well as the determination of the W mass from semi-leptonic events [10, 23, 25] and indirect measurements performed in precision electroweak tests at LEP1 [4].

Appendix A

How to improve the Jet Pairing Likelihood

As discussed in section 4.4.3, the sensitivity to the W mass is degraded if the mass is already used to determine the correct jet pairing for 5-jet events. This behaviour comes from the fact that the jet combinations with 5-C fitted masses in the vicinity of the mass of those Monte Carlo events, that are used to produce the probability density functions in the jet pairing likelihood (JPLH), are favoured. This effect is illustrated by the figure 4.15.

This appendix describes attempts to replace the 5-C fitted mass in the jet pairing likelihood by other variables that are powerful in order to determine the correct jet pairing but without being correlated to the mass itself. The following variables were investigated:

- the 5-C fit probability p_5^{5-C},

- the sum of the opening angles of the two W bosons $\alpha_{2j\text{-}W} + \alpha_{3j\text{-}W}$ where $\alpha_{3j\text{-}W}$ is the angle between the two most energetic jets of the 3-jet system,

- the opening angle of the 2-jet system $\alpha_{2j\text{-}W}$,

- the smallest "jet resolution" $\min(\ln y_{ij})$ (see equation 4.1) between the jets from the 3-jet system,

- the difference of the 4-C fitted masses $|\Delta M_W^{4-C}|_{\text{(flip lightest jet)}}$ of the two W bosons for the jet pairing that corresponds to the smallest jet of the 3-jet W being associated to the 2-jet system,

- the smallest difference of the 4-C fitted masses $\min\limits_{\text{all other comb.}} \{|\Delta M_W^{4-C}|\}$ of all other combinations than the one considered,

- the difference of the difference of the 4-C fitted masses $|\Delta M_W^{4-C}|_{\text{(flip lightest jet)}} - |\Delta M_W^{4-C}|$,

- $\min\limits_{\text{all other comb.}} \{|\Delta M_W^{4-C}|\} - |\Delta M_W^{4-C}|$ and

- the discrete variable I_{4to5} which expresses where those two jets that would be merged together in case of a 4-jet reconstruction end up: I_{4to5} has a value of

    - $I_{4to5} = 0$ if these two jets build together the 2-jet W of the considered combination,

75

- $I_{4to5} = 1$ if both fragments end up together in the 3-jet W,

- $I_{4to5} = 2$ if only the less energetic jet ends up in the 3-jet system and

- $I_{4to5} = 3$ otherwise.

The distributions for these variables can be seen in the figures A.1-A.9 for both the correct and the incorrect jet combinations. Only combinations with a 5-C fit probability exceeding 1% and a 5-C fitted mass larger than 65 GeV are considered. In case of the combinatorial background, all wrong combinations that fulfil these requirements enter the shown distributions.
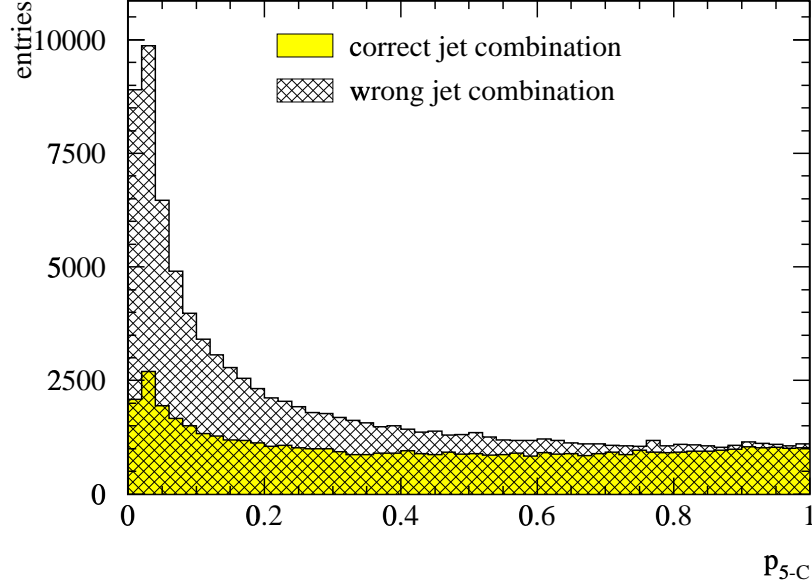
Figure A.1: 5-C fit probability p_5^{5-C}.

Comparing to figure 4.13, one can clearly see that none of theses variables are as powerful as the 5-C fitted mass itself. Even in an inclusion of multiple variables to the jet pairing likelihood (JPLH), part of their power to discriminate between correct and incorrect jet combinations might already be covered by the difference of the 4-C fitted mass and the minimum opening angle of the 3-jet system, variables that are already used in the JPLH. Furthermore, the aim is to find variables that are insensitive to the mass itself. Especially the variables derived from the opening angles ($\alpha_{2j\text{-}W}$ and $\alpha_{2j\text{-}W} + \alpha_{3j\text{-}W}$) are sensitive to the boost of each W boson, which is due to energy conservation determined by its mass: In the rest frame of the W boson, it decays into two particles with an angle of 180°. The larger the boost of the decaying particle, the smaller the angle between the two particles is allowed to be.

Table A.1 shows the correlations

$$\rho_{ij} = \frac{\langle (x_i - \bar{x}_i)(x_j - \bar{x}_j) \rangle}{\sqrt{\langle (x_i - \bar{x}_i)^2 \rangle \cdot \langle (x_j - \bar{x}_j)^2 \rangle}} \tag{A.1}$$

between the variables (i, j) used in the JPLH as well as those introduced in this appendix. This table shows that the opening angle of the 2-jet system $\alpha_{2j\text{-}W}$ is very much correlated with the W mass itself ($\rho = 55\%$). Replacing the mass in the JPLH by this angle would therefore still imply a sensitivity

Correlation [%]	1)	2)	3)	4)	5)	6)	7)	8)	9)	10)	11)	12)	13)
1) $\|\Delta M_W^{4-C}\|$	100	7.08	0.16	17.80	-57.21	16.46	24.16	9.23	-11.27	0.08	-43.86	-21.80	13.46
2) $\min_{3j-W}(\alpha_{ij})$		100	1.86	12.10	2.74	18.7	5.11	85.47	-3.64	-2.42	-5.68	-3.91	41.47
3) $\cos\theta_{3j-W}$			100	-0.66	2.15	-5.09	-8.27	-0.03	-1.61	-0.35	1.40	-0.38	0.76
4) M_W^{5-C}				100	-4.13	18.02	54.71	-0.97	1.97	-3.01	-4.21	6.83	3.60
5) p_5^{5-C}					100	2.36	-1.31	1.21	2.63	6.59	21.64	18.95	-1.27
6) $\alpha_{2j-W} + \alpha_{3j-W}$						100	30.40	18.71	16.75	-0.11	9.61	-3.71	18.77
7) α_{2j-W}							100	-2.05	9.50	12.58	-7.28	6.99	13.51
8) $\min_{3j-W}(\ln y_{ij})$								100	13.66	4.60	-15.46	-1.57	42.92
9) $\|\Delta M_W^{4-C}\|_{(\text{flip lightest jet})}$									100	4.42	94.23	2.90	-13.83
10) $\min_{\text{all other comb.}}\{\|\Delta M_W^{4-C}\|\}$										100	3.72	97.58	2.70
11) $\|\Delta M_W^{4-C}\|_{(\text{flip lightest jet})} - \|\Delta M_W^{4-C}\|$											100	9.96	-16.97
12) $\min_{\text{other comb.}}\{\|\Delta M_W^{4-C}\|\} - \|\Delta M_W^{4-C}\|$												100	0.32
13) I_{4jo5}													100

Table A.1: Correlation matrix of the jet pairing variables for W events. The variables 1), 2) and 3) are used to determine the jet pairing. In previous OPAL analyses [10, 25], the 5-C fitted mass, variable 4), was added to improve the jet pairing.
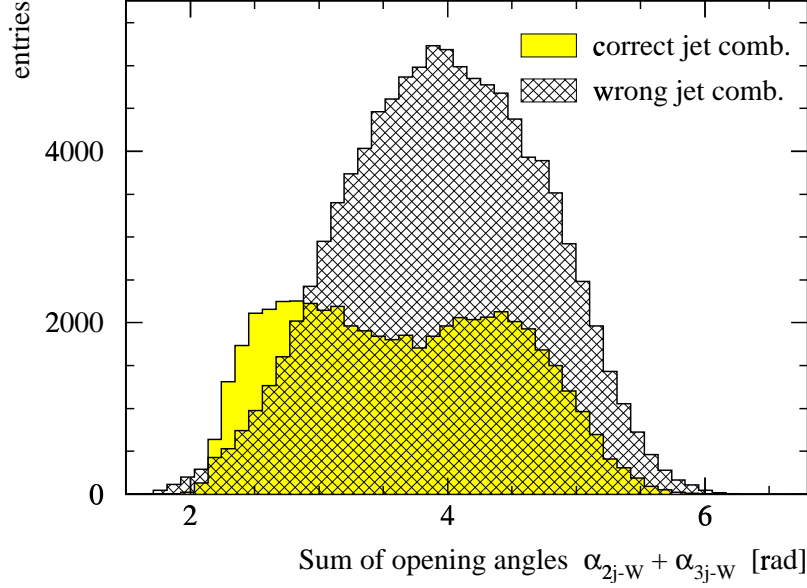
Figure A.2: The sum of the opening angles of the two W bosons $\alpha_{2j\text{-}W} + \alpha_{3j\text{-}W}$ where $\alpha_{3j\text{-}W}$ is the angle between the two most energetic jets of the 3-jet system.
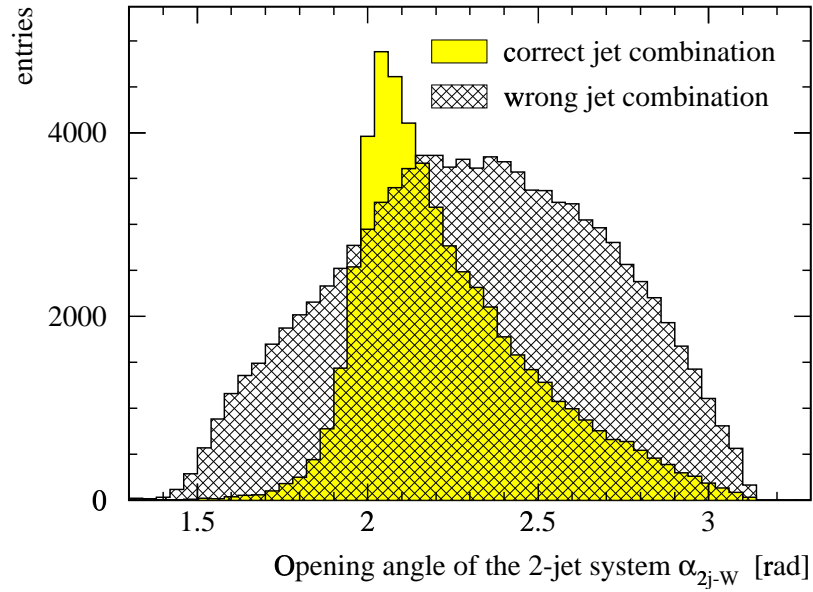
of the jet pairing to the W mass. The smallest y_{ij} of the 3-jet system is, since y_{ij} is proportional to the product of the angle and the smallest of the two jet energies, strongly correlated with the minimum opening angle of the 3-jet W ($\rho = 85\%$), a variable that is already included in the JPLH. The high correlation between the 5-C fit probability p_5^{5-C} and the 4-C fitted mass difference $|\Delta M_W^{4-C}|$ ($\rho = -57\%$) comes from the fact, that a jet combination with a large difference of the two W masses is likely to obtain a high χ^2 from a 5-C fit and therefore a small fit probability p_5^{5-C}, because of the equal-mass constraint that is incorporated in the 5-C fit.

A jet pairing likelihood selection using the additional variables

- p_5^{5-C},

- $\alpha_{2j\text{-}W} + \alpha_{3j\text{-}W}$,

- $\min\limits_{\text{all other comb.}} \{|\Delta M_W^{4-C}|\}$,

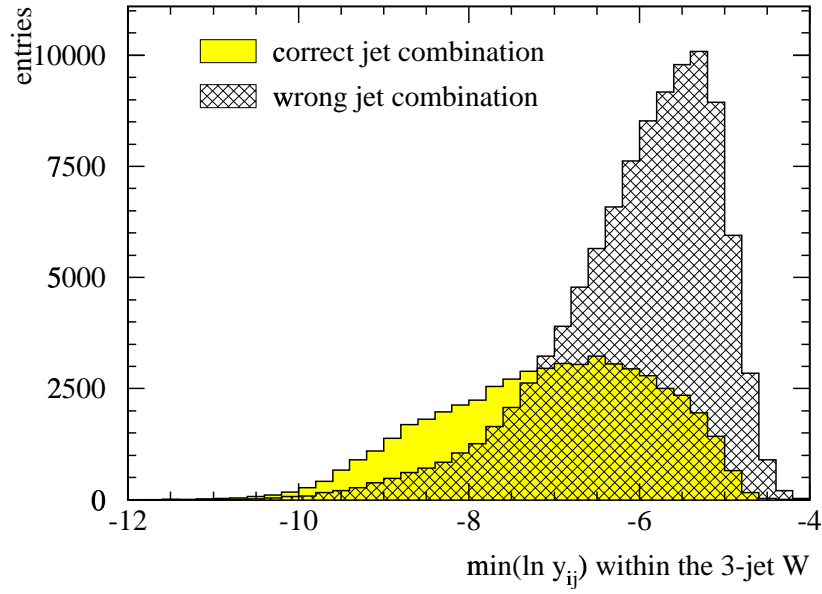- $|\Delta M_W^{4-C}|_{\text{(flip lightest jet)}} - |\Delta M_W^{4-C}|$ and

- I_{4to5}

enhances the jet pairing efficiency from about 59% to 61% with respect to the jet pairing likelihood as used in this analysis, i.e. without the 5-C fitted W mass as additional variable (see section 4.4.3). This efficiency is the fraction of correctly associated jets to all events that have at least one jet combination with a JPLH exceeding -4.2 and a 5-C fit probability greater than 1%.

The variables examined within the framework of this thesis were not sensitive enough and independent from the 5-C fitted mass at the same time. Therefore, it was decided to use a jet pairing without the 5-C fitted mass or any replacement. The low jet pairing efficiency was then improved by taking also the second best jet-W association into consideration. A proposal for further studies is to
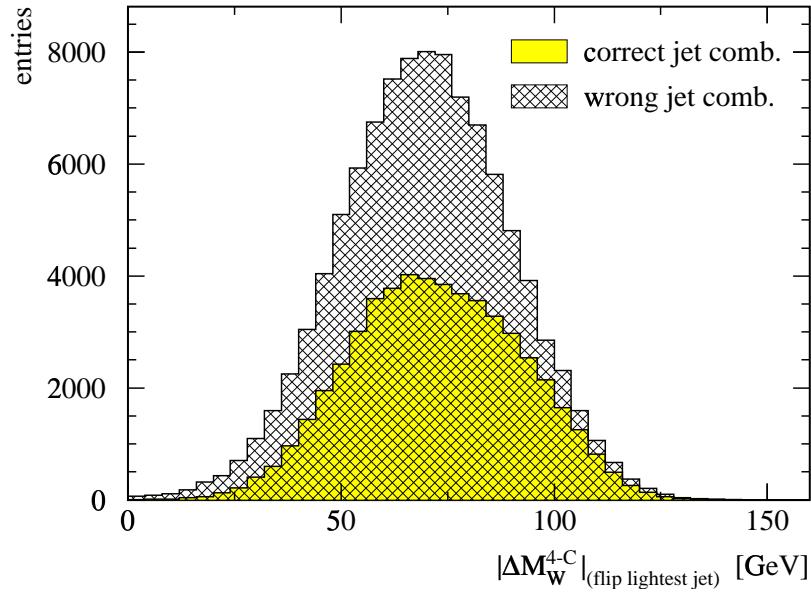
**Figure A.3:** The opening angle of the 2-jet system $\alpha_{2j\text{-}W}$.

examine whether the matrix elements for $WW \rightarrow q\bar{q}q\bar{q}$ events could possibly be a proper substitute for the W mass in the jet pairing likelihood.

**Figure A.4:** The smallest "jet resolution" $\min\left(\ln y_{ij}\right)$ between the jets from the 3-jet system.

Figure A.5: The difference of the 4-C fitted masses $\left|\Delta M_W^{4-C}\right|_{\text{(flip lightest jet)}}$ of the two W bosons for the jet pairing that corresponds to the smallest jet of the 3-jet W being associated to the 2-jet system.
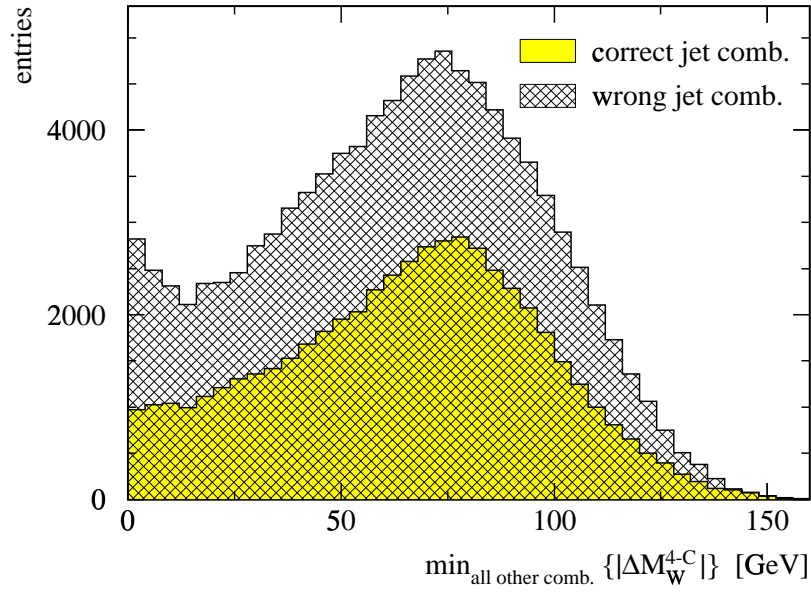
Figure A.6: The smallest difference of the 4-C fitted masses $\underset{\text{all other comb.}}{min}\left\{|\Delta M_W^{4-C}|\right\}$ of all other combinations than the one considered.
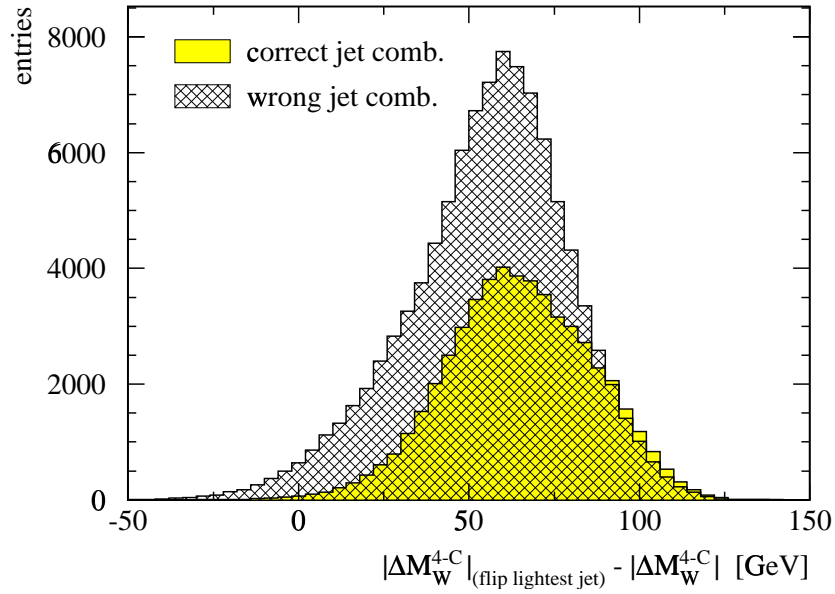
Figure A.7: The difference of the difference of the 4-C fitted masses $(|\Delta M_W^{4-C}|_{\text{(flip lightest jet)}} - |\Delta M_W^{4-C}|)$. $|\Delta M_W^{4-C}|$ is the mass difference for the considered jet pairing while $|\Delta M_W^{4-C}|_{\text{(flip lightest jet)}}$ belongs to the combination that corresponds to the smallest jet from the 3-jet system being flipped to the 2-jet W.
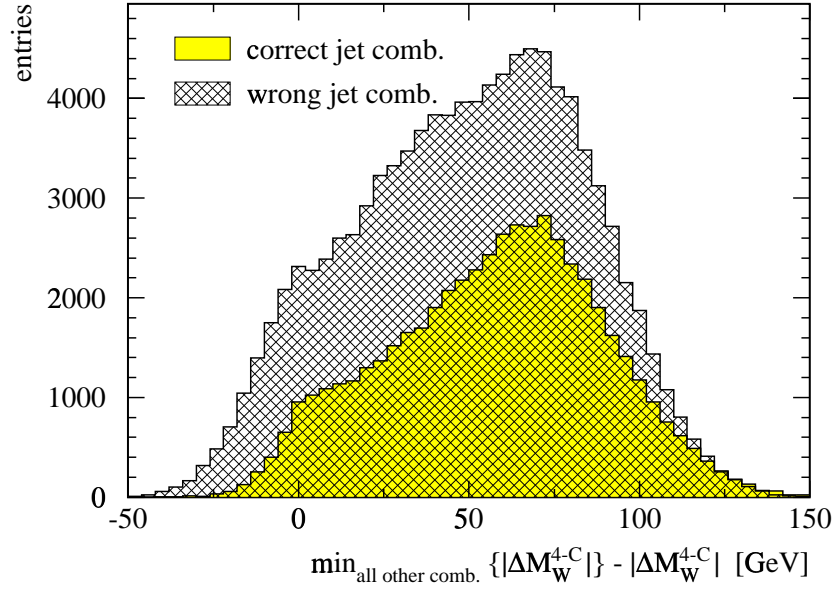
Figure A.8: The difference of the difference of the 4-C fitted masses ($\min\limits_{\text{all other comb.}} \left\{ |\Delta M_W^{4-C}| \right\} - |\Delta M_W^{4-C}|$) where the minimum is taken from all other jet pairings.
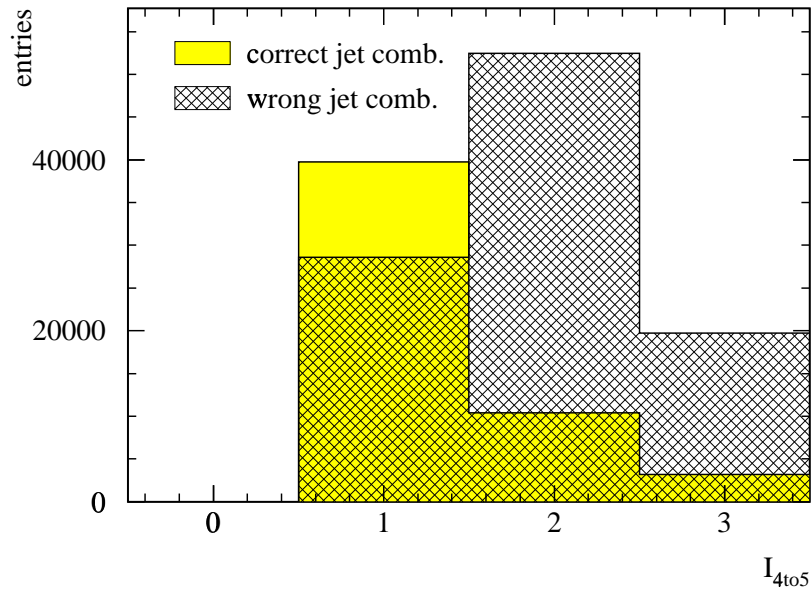
Figure A.9: The discrete variable I_{4to5} expresses in which W boson those two jets, that would have been merged in a 4-jet treatment, end up, as defined by the considered jet combination: $I_{4to5} = 0$: These two jets build together the 2-jet W. $I_{4to5} = 1$: Both fragments end up together in the 3-jet W. $I_{4to5} = 2$: Only the less energetic jet ends up in the 3-jet system and $I_{4to5} = 3$ otherwise.

Appendix B

Monte Carlo Samples

This appendix summarises the different Monte Carlo samples used to obtain the reweighted spectra, the expected errors and the systematic checks performed in this thesis, all corresponding to a centre-of-mass energy of $\sqrt{s} = 189$ GeV.

Run no.	Generator info	M_W/GeV	Γ_W/GeV	$\sqrt{s}$/GeV	Events
9298	KORALW/JETSET, grc4f	79.83	2.0544	188.634	50000
9299	KORALW/JETSET, grc4f	80.08	2.0738	188.634	100000
9300	KORALW/JETSET, grc4f	80.33	2.0933	188.634	200000
9301	KORALW/JETSET, grc4f	80.58	2.1129	188.634	100000
9302	KORALW/JETSET, grc4f	80.83	2.1326	188.634	50000

Table B.1: Monte Carlo signal samples used to create the reweighted histograms at a centre-of-mass energy of $\sqrt{s} = 189$ GeV.

Background	Run no.	Generator info	$\sqrt{s}$/GeV	Events
Z^0/γ ($q\bar{q}$ backgr.)	5111	PYTHIA	189.000	500000
4-f (non-WW)	9323	KORALW/JETSET,grc4f	188.634	151563

Table B.2: Monte Carlo non-WW background samples at a centre-of-mass energy of $\sqrt{s} = 189$ GeV.

ρ	Run no.	Generator info	M_W/GeV	$\sqrt{s}$/GeV	events
0	9232	KORALW/JETSET, grc4f	80.33	188.634	100000
∞	9233	KORALW/JETSET, grc4f	80.33	188.634	100000

Table B.3: Monte Carlo signal samples used for colour reconnection studies (Sjöstrand-Khoze model I) at a centre-of-mass energy of $\sqrt{s} = 189$ GeV. These two samples contain the same events which are identical up to the end of the parton shower. Out of these two samples, MC samples can be mixed for any given value of ρ.

Bibliography

[1] G. Kane. *Modern Elementary Particle Physics*. Addison-Wesley, 1993.

[2] D.J. Griffiths. *Introduction to Elementary Particles*. New York Wiley, 1987.

[3] P. Schmüser. *Feynman-Graphen und Eichtheorien für Experimentalphysiker*. Berlin Springer, 1988.

[4] LEP Electroweak Working Group. A combination of preliminary electroweak measurements and constraints on the standard model. Technical Report 2000-016, CERN, 2000.

[5] UA1 Collaboration. *Zeit. Phys.*, C(44):15, 1989.

[6] UA2 Collaboration. *Phys. Lett.*, B(276):354, 1992.

[7] G. Altarelli, T. Sjöstrand, and F. Zwirner Eds. Physics at LEP2. Technical Report CERN 96-01, CERN, 1996. Volume 1.

[8] The OPAL collaboration. W^+W^- Production Cross Section and W Branching Fractions in e^+e^- Collisions at 189 GeV . *Submitted to Phys. Lett. B*, 2000.

[9] A. Gurtu. Precision Tests of the Electroweak Gauge Theory. In *Proceedings of XXXth International Conference on High Energy Physics*, Osaka, Japan. To be published.

[10] The OPAL Collaboration. Measurement of the W mass and Width in e^+e^- Collisions at 189 GeV. *to be sent to Phys. Lett. B*, 2000.

[11] The Particle Data Group. *The European Physical Journal C: Review of Particle Physics*, volume C. Società Italiana di Fisica and Springer-Verlag, 2000.

[12] The LEP2 Team. LEP Design Report. Technical Report CERN-AC/96-01, CERN, 1996.

[13] A. Lasseur B. Desforges. 1999 SPS and LEP Machine Statistics. Technical Report SL-Note-99-051 OP, CERN, 1999.

[14] LEP Energy Working Group. Evaluation of the LEP Centre-of-Mass Energy for Data taken in 1998. Technical Report CERN 99-01, CERN, 1999.

[15] LEP Energy Working Group. Evaluation of the LEP Centre-of-Mass Energy above the W-Pair Production Threshold. *Eur. Phys. J.*, C(11):573–585, 1999.

[16] K. Ahmet *et al.* The OPAL Detector at LEP. *Nucl. Instr. Meth.*, A(305):275, 1991.

[17] B.E. Anderson *et al* The OPAL Collaboration. The OPAL Silicon-Tungsten Calorimeter and Front End Electronics. *IEEE Trans. Nucl. Sci.*, (41):845, 1994.

[18] S. Anderson *et al*. The extended OPAL Silicon Strip Microvertex Detector. *Nucl. Instr. Meth.*, A(403):326, 1998.

[19] J. Allison et al. *Nucl. Instr. Meth.*, A(317):47, 1992.

[20] R. Brun. GEANT 3 Users Guide. Technical Report CERN/DD/EE/84-1, CERN, 1984.

[21] P. Mendéz-Lorenzo. PhD thesis, Ludwigs-Maximilians-Universität München, 2000. In preparation.

[22] The OPAL Collaboration. W^+W^- production in e^+e^- collisions at 189 GeV. OPAL Physics Note PN378, CERN, 1999.

[23] J. Dubbert. *Measurement of the W Boson Mass in the $WW \rightarrow qql\nu$ Channel with the OPAL Detector at LEP*. PhD thesis, Ludwig-Maximilians-Universität München, 2000. In preparation.

[24] M.A. Thomson. The OPAL $W^+W^- \rightarrow q\overline{q}\ell\overline{\nu}$ Event Selection. Opal Technical Note TN635, CERN, 2000.

[25] The OPAL Collaboration. Measurement of the W Mass and Width in e^+e^- Collisions at 183 GeV. *Phys. Lett.*, B(453):138, 1999.

[26] The OPAL Collaboration. Measurement of the Mass of the W Boson in e^+e^- Annihilations at 192-202 GeV. OPAL Physics Note PN422, CERN, 2000.

[27] N. Brown and X.J. Stirling. Jet Cross-Sections at leading double Logarithm in e^+e^- Annihilation. *Phys. Lett.*, B(252):657, 1990.

[28] S. Mihara and S. Yamashita. MT 3.00 a new Algorithm to calculate Energy Flow based on MT Package. OPAL Technical Note TN575, CERN, 1998.

[29] http://www.cern.ch/opal/group/ww/wmassworkpages/drw/wwfix.html. internal web page.

[30] E. Torrence. $W^+W^- \rightarrow qqqq$ Event Selection at 189 GeV. OPAL Technical Note TN650, CERN, 2000.

[31] S. Catani and M.H. Seymour. The Dipole Formalism for the Calculation of QCD Jet Cross-sections at next-to-leading Order. *Phys. Lett.*, B(378), 1996.

[32] F.A. Berends, R. Pittau, and R. Kleiss. EXCALIBUR - a Monte Carlo Program to evaluate all four-Fermion Processes at LEP 200 and beyond. *Comp. Phys. Comm.*, (85):437–452, 1995.

[33] R.L. Coxe. *Measurement of the Mass and the Width of the W Boson with the OPAL detector at LEP*. PhD thesis, University of Chicago, 2000.

[34] R. J. Barlow. *A guide to the Use of Statistical Methods in Physical Science*. John Whiley & Sons, 1989.

[35] K. Ishii, T. Saeki, and S. Yamashita. Jet Error Parameterization. OPAL Technical Note TN449, CERN, 1996.

[36] K. Ishii and S. Yamashita. Jet Error Parameterization for MT 3.00. OPAL Technical Note TN577, CERN, 1998.

[37] C.P. Ward C.G. Littlewood and D.R. Ward. Measurement of the Mass of the W Boson at 189 GeV using an analytic Breit-Wigner fit. OPAL Technical Note TN658, CERN, 2000.

[38] C. Burgard and C. Hartmann. Measurement of the Mass and the Width of the W Boson Using a Reweighting Method. OPAL Technical Note TN468, CERN, 1997.

[39] R. Barlow. Application of the Bootstrap Resampling Technique to Particle Physics Experiments. *MAN/HEP/99/4*, 2000.

[40] The OPAL Collaboration. Bose-Einstein Correlations in $e^+e^- \rightarrow W^+W^-$ at 172 and 183 GeV. *Eur. Phys. J.*, C(8):559–571, 1999.

[41] J. Schiek. *Bose-Einstein Correlations in* $e^+e^- \rightarrow W^+W^-$ *events at 172, 183 and 189 GeV*. PhD thesis, Ruprecht-Karls-University Heidelberg, 1999.

[42] U. Pettersson G. Gustafson and P.M. Zerwas. *Phys.Lett.*, B(209):90, 1988.

[43] The OPAL Collaboration. Colour Reconnection Studies in $e^+e^- \rightarrow W^+W^-$ at $\sqrt{s} = 183$ GeV. *Phys. Lett.*, B(453):153, 1999.

[44] A.B̃londel et al. Evaluation of the LEP Centre-of-Mass Energy above the W-Pair Production Threshold. *Eur. Phys. J.*, C(11):573, 1998.

[45] G. Alexander *et al.* OPAL Collaboration. A Comparison of *b* and *uds* Quark Jets to Gluon Jets. *Z. Phys.*, C(69):543, 1996.

[46] P.D. Acton *et al.* OPAL Collaboration. A Study of Differences between Quark and Gluon Jets using Vertex Tagging of Quark Jets. *Z. Phys.*, C(58):387, 1993.

[47] L. Loennblad. Reconnecting coloured Dipoles. *Z. Phys.*, C(70):107, 1996.

Acknowledgement